COMPUTATIONAL INVERSE SOLUTION STRATEGIES FOR VISCOELASTIC MATERIAL CHARACTERIZATION USING VIBROACOUSTIC METHODS

A Dissertation

Presented to the Faculty of the Graduate School

of Cornell University

In Partial Fulfillment of the Requirements for the Degree of

Doctor of Philosophy

by

John Charles Brigham

August 2008

COMPUTATIONAL INVERSE SOLUTION STRATEGIES FOR VISCOELASTIC MATERIAL CHARACTERIZATION USING VIBROACOUSTIC METHODS

John Charles Brigham, Ph. D.

Cornell University 2008

Vibroacoustic testing methods are those in which a fluid immersed solid is excited by a remote force, while the resulting acoustic emission in the surrounding fluid is measured. The particular method studied herein consists of measuring the acoustic pressure amplitudes in the fluid surrounding a solid being vibrated to a steady-state with a harmonic pressure. These techniques are currently under development for use in nondestructive and noninvasive imaging of biological soft tissues. However, there is significant potential to extend these methods for quantitative characterization of tissue properties. Furthermore, viscoelastic material properties carry information about stiffness and damping of materials, both of which are significantly affected by the presence of disease. Therefore, approaches to extract these rate dependent properties will have considerable implications in the diagnosis and treatment of disease.

Computational techniques were developed and analyzed to characterize the viscoelastic properties of solids using vibroacoustic tests. The techniques presented involve casting the inverse problem as a minimization problem which is then solved using a global nonlinear optimization algorithm. Through numerical and laboratory experiments, acoustic emissions are shown to hold sufficient information for quantifying both elastic and viscoelastic material behavior. In addition, a unique optimization algorithm is presented to account for the computational expense of

numerical representations of biological systems along with the simulation demands of global optimization. The methodology, referred to as the Surrogate-Model Accelerated Random Search (SMARS) algorithm, is a non-gradient based iterative application of a random search algorithm and the surrogate-model method for optimization. Through simulated examples, the SMARS algorithm is shown to be both robust and efficient. In the cases examined, the SMARS algorithm is shown to outperform two traditional global optimization algorithms by attaining more accurate solutions with fewer function evaluations. Lastly, an approach is shown for incorporating the proper orthogonal decomposition (POD) technique for model reduction into the inverse solution strategy to further reduce the computational cost. The POD reduced-order modeling methodology is shown to be capable of generalizing over the viscoelastic material search domains for the inverse problems and identifying accurate estimates to the viscoelastic behavior of solids with minimal computational expense.

BIOGRAPHICAL SKETCH

John Brigham was raised in South Burlington, Vermont by his loving parents Mark and Kathleen, and alongside his older brother Jason. In 1999 John graduated among the top members of his class from South Burlington High School and began his studies in civil engineering and mathematics at Vanderbilt University in Nashville, Tennessee. In 2003 John graduated from Vanderbilt *magna cum laude* with a B.E. in civil engineering and mathematics. John then decided to continue his education with graduate studies in civil engineering. In the fall of 2003 John and his future wife Katharine came to Cornell University in Ithaca, New York, and John began his tenure at Cornell University in the structures group of the Department of Civil and Environmental Engineering. During his Ph.D. studies at Cornell, John studied under the supervision of Professor Wilkins Aquino in the broad fields of computational mechanics and inverse problems, with particular emphasis on inverse characterization in biomechanics. Along the way he achieved one of his greatest accomplishments when he married Katharine Gau, now Katharine Brigham. In September 2008 John will join the faculty in the Department of Civil and Environmental Engineering at the University of Pittsburgh as an Assistant Professor.

For K. Brigham

ACKNOWLEDGMENTS

I would like to first express my deepest gratitude to my advisor and chair of my graduate committee Professor Wilkins Aquino. Without his unending faith in my potential and his wonderful and tireless guidance none of my success could have been possible.

My thanks to Professor Subrata Mukherjee, not only for serving on my graduate committee, but also for his significant contribution to my education and his generous support during times of need.

I would also like to thank Professor Anthony Ingraffea and Professor James Greenleaf for serving on my graduate committee and for their support throughout my studies.

I am deeply indebted to Professor Chris Earls. In a very short amount of time Professor Earls has become one the greatest mentors I have ever had.

I must also thank Professor Peter Diamessis. I owe much of my sanity and successes, particularly towards the end of my studies, to our lunchtime philosophical discussions.

Last, but certainly not least, I would like to thank my family for their love and support, without which I could not have accomplished anything. In particular, I am eternally grateful for my father's humble brilliance, my mother's never ending strength, my brother's quiet caring nature, and my wife's unlimited kindness, all of which will always be a source of inspiration.

TABLE OF CONTENTS

LIST OF FIGURES

LIST OF TABLES

CHAPTER 1

Inverse Estimation of Viscoelastic Material Properties for Solids Immersed in Fluids using Vibroacoustic Techniques[1]

1.1 Abstract

This work presents an approach to inversely determine material properties for solids immersed in fluids through the use of steady-state dynamic response. The methodology uses measured acoustic pressure amplitudes in the fluid surrounding a structure being vibrated with a harmonic force to determine the parameters for elastic and viscoelastic material models. Steady-state dynamic finite element analysis is used to compute the frequency response function of homogeneous and heterogeneous solids. The frequency response is then used to inversely estimate material parameters. In order to solve the inverse problem, an optimization method is presented which combines the global search capabilities of the random search method with the reduced computational time of a surrogate-model approach. Through numerical and laboratory experiments, this work shows that acoustic emissions hold sufficient information for quantifying both elastic and viscoelastic material behavior. Furthermore, the examples show that the surrogate model accelerated random search algorithm is an efficient and accurate method for solving these types of inverse problems. This research has direct and important implications in non-destructive evaluation of material properties in general. However, the examples shown in this paper are based on applications related to non-invasive characterization of biological materials through methodologies currently applied to medical imaging.

1.2 Introduction

Methods for non-destructive evaluation of material properties are of strong interest in many fields of engineering and science. Several examples include the work by Albanese, Banks, and Raye [1], Audoin [5], Ogi, Sato, Asada, and Hirao [30], Aristegui and Baste [3], and Aquino and Brigham [2]. Non-destructive and non-invasive methods to characterize material behavior are of particular interest in the medical field. Determining the properties of biological structures provides valuable insight into the onset and progression of various diseases, as well as the development of tools to diagnose and treat illness. Examples include the work by Baldewsing, De Korte, Schaar, Mastik, and Van Der Steen [7], and the work by Haemmerich, Tungjitkusolmun, Staelin, Lee, Mahvi, and Webster [22], which use finite element analyses to model the behavior of biological structures. In both examples it is crucial that accurate material properties be determined to develop modeling tools for diagnosis and treatment of diseases.

Biological soft tissues pose particular difficulty for material identification due to their rate-dependent mechanical behavior [19, 20]. Thus, in order to characterize the mechanical behavior of soft tissues, it is necessary to perform tests that reveal this rate dependent behavior. This requires the use of dynamic testing procedures to measure features such as waveforms, wave speeds, impedances, steady-state dynamic responses, and other time or frequency dependent behavior. Examples of these methods include the work by Catheline, Gennisson, Delon, Fink, Sinkus, Abouelkaram, and Culioli [10], Levinson, Shinagawa, and Sato [24], Leymarie, Aristegui, Audoin, and Baste [25], and Chen, Fatemi, and Greenleaf [11]. However, in general current methods require the application of mechanical forces and contact response measurements in controlled laboratory settings, or are applicable only for simple geometries and material behavior.

A methodology, known as vibro-acoustography (VA), was developed in the realm of medical imaging that offers the potential for the noninvasive characterization of the mechanical properties of tissues [15, 16]. VA uses ultrasound radiation force (a nonlinear, second-order phenomenon in wave theory) to exert a localized oscillating stress field at a desired low frequency (normally in the kHz range) within or on the surface of the object. In this method, the dynamic radiation force is produced by focused continuous-wave ultrasound beams driven at slightly different frequencies. The two beams are focused at the same point in the object. Interference between the two beams produces a radiation force oscillating at the difference frequency. In response to this oscillating force, the object vibrates, resulting in an acoustic radiation field. This acoustic field is detected by a sensitive hydrophone and used to form an image of the object as the focal point of the ultrasound beam is scanned within the object.

Alternatively, the acoustic emissions obtained through VA can be used to estimate the mechanical properties of the imaged object [28]. This problem is of crucial importance, especially in the medical field, because of the ubiquitous presence of stiff tissue often represents an early warning sign for disease, as in the cases of breast or prostate cancer [17, 21]. Very often tumors are found at surgery that were occult even with modern imaging instruments.

The inverse identification of material properties through acoustic emissions, like the majority of inverse problems, can easily become intractable as material behavior, geometry, and/or boundary conditions gain any degree of complexity. It is often not possible to find analytical solutions to such inverse problems, thus requiring numerical modeling for the forward or direct problem, and the use of nonlinear optimization methods to search for the inverse solution. This model updating approach to inverse problems has gained much popularity in recent years due to a relentless increase in

computational speed [2, 4, 6].

Common optimization methods used for the solution of inverse problems are divided into two main families: gradient-based (e.g. conjugate gradient, Newton, etc.) and non gradient-based approaches (e.g. neural networks, genetic algorithms, simulated annealing, random search, etc.). In gradient based methods, the derivatives of an error measure need to be determined. These methods offer the advantage of being computationally faster than non-gradient based methods. However, they suffer from two main drawbacks: the derivative of the error measure may not be defined in some portions of the search domain and convergence is only guaranteed to local extrema (i.e. local minimum/maximum). On the other hand, non gradient-based methods do not require the computation of the derivatives of an error measure and offer global convergence capabilities.

The inverse identification of material properties, in general, requires convergence to global extrema. Therefore, the optimization approach used in this work emphasizes the use of non-gradient based methods. In the approach proposed in this paper, a surrogate model optimization strategy is combined with a classical random search (RS) technique to form the Surrogate-Model Accelerated Random Search (SMARS) algorithm. The SMARS method takes advantage of the global search capabilities of RS while increasing the rate of convergence through a surrogate model approach.

The methodology proposed herein integrates vibroacoustic techniques with the SMARS algorithm to inversely characterize viscoelastic properties of solids immersed in fluids. This work presents an approach that can find wide applications in non-destructive material evaluation, particularly in medical applications such as non-invasively quantifying material properties in living tissue. First, the finite element (FE) formulation for coupled fluid-structure interaction is presented. Next, the SMARS algorithm is described. Lastly, four examples are presented, in which material

properties are inversely determined for elastic and viscoelastic solids vibrating in an acoustic medium. Three of the examples involve simulated tests, while the fourth example includes physical experimental results as reported by Mitri [28].

1.3 Finite Element Formulation of the Vibroacoustics Problem

1.3.1 Solid Mechanics Formulation

Fluid-structure interaction, in the present context, can be described mathematically by a coupled system of partial differential equations (PDEs) derived from the conservation of linear momentum. For the purposes of this work, body forces are assumed to be negligible. Thus, the governing differential equation for structural behavior is given by

$$\nabla \cdot \boldsymbol{\sigma}(\vec{x},t) = \rho \ddot{\vec{u}}(\vec{x},t) \quad \text{on } \Omega . \tag{1}$$

A constitutive model describing the stress-strain relationship in a general rate dependent form can be represented as

$$\boldsymbol{\sigma}(\vec{x},t) = f\left(\boldsymbol{\varepsilon}(\vec{x},t), \frac{\partial \boldsymbol{\varepsilon}(\vec{x},t)}{\partial t}, \frac{\partial^2 \boldsymbol{\varepsilon}(\vec{x},t)}{\partial t^2}, ..., \frac{\partial^n \boldsymbol{\varepsilon}(\vec{x},t)}{\partial t^n}\right). \tag{2}$$

Assuming small strains and deformations, the strains are defined as

$$\boldsymbol{\varepsilon}(\vec{x},t) = \frac{1}{2}\left[\nabla \vec{u}(\vec{x},t) + \left(\nabla \vec{u}(\vec{x},t)\right)^T\right]. \tag{3}$$

The above assumption is justified since the displacements and strains resulting from vibroacoustic excitations are, in general, small.

The natural boundary conditions are given by the Cauchy formula as

$$\boldsymbol{\sigma}(\vec{x},t)\vec{n}(\vec{x}) = \vec{T}(\vec{x},t) \quad \text{on } \Gamma_T , \tag{4}$$

and the essential boundary conditions are given as

$$\vec{u}(\vec{x},t) = \vec{u}^o(\vec{x},t) \quad \text{on } \Gamma_u . \tag{5}$$

The initial displacements and velocities in the body are assumed to be zero. In the above equations, $\vec{x}$ is the spatial position vector, t is time, $\boldsymbol{\sigma}(\vec{x},t)$ is the stress tensor,

ρ is the mass density (assumed constant in this work), $\vec{u}(\vec{x},t)$ is the displacement vector, $\boldsymbol{\varepsilon}(\vec{x},t)$ is the strain tensor, $\vec{n}(\vec{x})$ is the unit vector normal to the surface, $\vec{T}(\vec{x},t)$ is the traction vector, Ω is the given domain of interest, Γ is the boundary of the domain, Γ_T is the portion of the boundary where external traction is specified, and Γ_u is the portion of the boundary where the displacement is specified. In this work, vectors are shown with arrows (or curved brackets for discretization), second order tensors are shown in bold, fourth order tensors are shown with IV as a superscript, and matrices are shown with square brackets. Each dot over a variable represents a derivative with respect to time.

1.3.2 Viscoelastic Constitutive Model

In this work, the stress-strain relationship in the solid was considered to be defined by a linear viscoelastic model obeying an exponential series relaxation law (i.e. Prony series) in the time domain given by

$$\boldsymbol{\sigma}(\vec{x},t) = \mathbf{C}^{IV}\boldsymbol{\varepsilon}(\vec{x},t) + \sum_{m=1}^{n}\left[\int_0^t \tilde{\mathbf{C}}_m^{IV} e^{-(t-\xi)/\tau_m}\frac{\partial\boldsymbol{\varepsilon}(\vec{x},\xi)}{\partial\xi}d\xi\right], \tag{6}$$

where $\mathbf{C}^{IV}$ is the 4th order tensor representing the long-term purely elastic moduli of the material, $\tilde{\mathbf{C}}_m^{IV}$ are the 4th order tensors representing the viscous moduli, t is total time, and τ_m are known as the relaxation times. This viscoelastic relationship is an expansion to three-dimensions of the traditional one-dimensional relationship derived from a rheological model of n parallel sets of springs and dashpots in series (Maxwell elements), with an additional spring in parallel, and is referred to as the generalized Maxwell model, see Figure 1.1. (See Findley, Lai, and Onaran [18] for a complete discussion of viscoelasticity) .

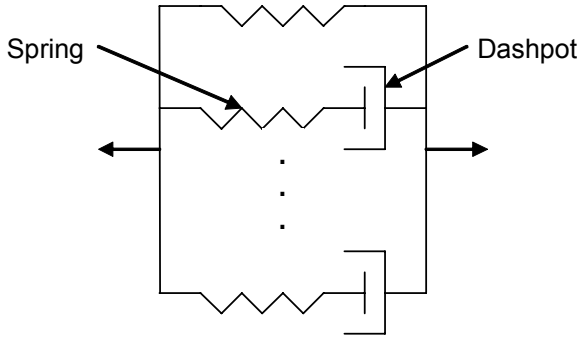

Figure 1.1. One dimensional generalized Maxwell model for viscoelasticity.

In general, for the extension of the one-dimensional generalized Maxwell model to three-dimensions, each component of the constitutive 4th order tensor can be assumed to be governed by a Prony series relationship. To simplify the three dimensional formulation without sacrificing generality, the relaxation time was considered to be a single value for each Maxwell element, as shown in Equation (6). This simplification is used to limit the number of parameters required to define the material model, while still maintaining the same overall behavior of the generalized Maxwell model representation. It is important to bear in mind that if no Maxwell units are used (i.e. $n = 0$), the representation shown in Equation (6) simplifies to a purely linear elastic material model.

The time-domain relaxation model can be converted to the frequency domain by assuming harmonically varying strains and stresses given by

$$\boldsymbol{\varepsilon}(\vec{x},t) = \boldsymbol{\varepsilon}_o(\vec{x},\omega)e^{i\omega t} \tag{7}$$

and

$$\boldsymbol{\sigma}(\vec{x},t) = \boldsymbol{\sigma}_o(\vec{x},\omega)e^{i(\omega t+\delta)} = \boldsymbol{\sigma}^*(\vec{x},\omega)e^{i(\omega t)}, \tag{8}$$

where

$$\boldsymbol{\sigma}^*(\vec{x},\omega) = \boldsymbol{\sigma}_o(\vec{x},\omega)e^{i\delta}. \tag{9}$$

In the above equations, ω is the circular frequency, $\boldsymbol{\varepsilon}_o$ and $\boldsymbol{\sigma}_o$ are the strain amplitude and the stress amplitude respectively, and δ is the phase lag between the

stress and strain responses. Typically, δ is used as a measure of viscous damping in the material. By substituting Equations (7)-(9) into Equation (6), the stress-strain relationship can be expressed in the frequency domain as

$$\boldsymbol{\sigma}^{*}(\vec{x},\omega) = \mathbf{C}^{*IV}(\omega)\boldsymbol{\varepsilon}_{o}(\vec{x},\omega), \tag{10}$$

where

$$\mathbf{C}^{*IV}(\omega) = \mathbf{C}^{IV} + \sum_{m=1}^{n} \tilde{\mathbf{C}}_{m}^{IV}\left(\frac{\omega^2\tau_m^2 + i\omega\tau_m}{1+\omega^2\tau_m^2}\right). \tag{11}$$

$\mathbf{C}^{*IV}(\omega)$ is referred to as the complex relaxation tensor of the material.

1.3.3 Structural Discretization

In the following derivations, the stress, strain, and elasticity tensors are converted to vectors and matrices through the conventions of Voight notation [12]. Let a continuous virtual displacement field, $\delta\vec{u}(\vec{x})$, be defined on Ω and Γ. The virtual displacement field is defined such that it vanishes where essential boundary conditions are specified. The principle of virtual work is expressed as [12]

$$\int_{\Omega}\rho\delta\vec{u}(\vec{x},t)\cdot\ddot{\vec{u}}(\vec{x},t)\,dV + \int_{\Omega}\delta\vec{\varepsilon}(\vec{x},t)\cdot\vec{\sigma}(\vec{x},t)\,dV - \int_{\Gamma_T}\delta\vec{u}(\vec{x},t)\cdot\vec{T}(\vec{x},t)\,d\Gamma_T = 0, \tag{12}$$

where $\delta\vec{\boldsymbol{\varepsilon}}(\vec{x},t)$ is the virtual strain field corresponding to the virtual displacement field.

To obtain a system of ordinary differential equations in time the domain is divided into finite elements and the displacement and virtual displacement fields are approximated within each element as

$$\vec{u}(\vec{x},t) = \left[N(\vec{x})\right]\left\{u^{e}(t)\right\} \tag{13}$$

and

$$\delta\vec{u}(\vec{x}) = \left[N(\vec{x})\right]\left\{\delta u^{e}\right\}, \tag{14}$$

where $\left[N(\vec{x})\right]$ is the matrix containing the interpolation functions for an element. Substituting the field approximations into Equation (12), eliminating the arbitrary

virtual displacement field vector, and adding individual element contributions, the semi-discretized form of the equation of motion becomes

$$\left[M\right]\left\{\ddot{u}(t)\right\}+\left\{I(t)\right\}=\left\{R(t)\right\}, \tag{15}$$

where $\left[M(\vec{x})\right]$ is the global mass matrix, $\left\{\ddot{u}(t)\right\}$ is the global vector of nodal accelerations, $\left\{I(t)\right\}$ is the internal force vector, and $\left\{R(t)\right\}$ is the external force vector. These global quantities are defined as

$$\left[M\right]=\sum_{elements}\int_{\Omega^e}\rho\left[N(\vec{x})\right]^T\left[N(\vec{x})\right]dV, \tag{16}$$

$$\left\{I(t)\right\}=\sum_{elements}\int_{\Omega^e}\left[B(\vec{x})\right]^T\vec{\sigma}(\vec{x},t)dV, \tag{17}$$

and

$$\left\{R(t)\right\}=\sum_{elements}\int_{\Gamma_T^e}\left[N(\vec{x})\right]^T\vec{T}(\vec{x},t)dS, \tag{18}$$

where $\left[B(\vec{x})\right]$ is the matrix of spatial derivatives of the interpolation functions, and the summation over elements refers to the assembly of the element matrices.

1.3.4 Fluid Behavior

For a compressible fluid with no net flow and small pressure amplitudes, the governing PDE for conservation of linear momentum is given by [23]

$$\nabla p(\vec{x},t)+\rho_f\ddot{\vec{u}}^f(\vec{x},t)=0 \quad \text{on } \Phi. \tag{19}$$

The pressure is related to the gradient of displacements through the fluid constitutive relationship as [23]

$$p(\vec{x},t)=-B_f\nabla\cdot\vec{u}^f(\vec{x},t). \tag{20}$$

The essential and natural boundary conditions are given, respectively, as

$$p(\vec{x},t)=p_o(\vec{x},t) \quad \text{on } \Psi_p, \tag{21}$$

and

$$\frac{\partial p(\vec{x},t)}{\partial\vec{n}_f(\vec{x})}=-\rho_f\ddot{u}_n^f(\vec{x},t) \quad \text{on } \Psi_u, \tag{22}$$

where $p(\vec{x},t)$ is the scalar fluid pressure in excess of hydrostatic pressure, ρ_f is the

mass density of the fluid, $\vec{u}^{\,f}(\vec{x},t)$ is the fluid particle displacement, B_f is the bulk modulus of the fluid, $\vec{n}_f(\vec{x})$ is the unit normal to the fluid surface, $\ddot{u}_n^f(\vec{x},t)$ is the acceleration of the fluid boundary in the direction of the normal, Φ is the fluid domain, Ψ is the boundary of the fluid domain, Ψ_p is the portion of the boundary where pressure is specified, and Ψ_u is the portion of the boundary where acceleration is specified. Viscosity of the fluid is neglected in this work.

1.3.5 Fluid Discretization

Using a variational approach [12], an arbitrary, continuous, virtual pressure field, $\delta p(\vec{x},t)$, is defined on Φ and Ψ. Taking the divergence of Equation (19) and substituting Equation (20), the acoustic wave equation becomes

$$\nabla^2 p(\vec{x},t) - \frac{\rho_f}{B_f}\ddot{p}(\vec{x},t) = 0\,. \tag{23}$$

Then, taking the product of the virtual pressure field with Equation (23), integrating over the domain, applying divergence theorem, and substituting natural boundary conditions, the weak form of the acoustic field problem is given by

$$\begin{aligned}&\int_\Phi \delta p(\vec{x},t)\frac{\rho_f}{B_f}\ddot{p}(\vec{x},t)dV + \int_\Phi \nabla\delta p(\vec{x},t)\cdot\nabla p(\vec{x},t)dV + \cdots \\ &\cdots + \int_\Psi \delta p(\vec{x},t)\rho_f \ddot{u}_n^f(\vec{x},t)dS = 0\end{aligned}\,. \tag{24}$$

Similarly to the structural discretization, the domain is divided into finite elements and the pressure field is approximated within each element. Substituting the field approximations into Equation (24) and eliminating the virtual pressure field vector, the semi-discretized acoustic wave equation becomes

$$\left[M_f\right]\left\{\ddot{p}(t)\right\} + \left[K_f\right]\left\{p(t)\right\} = -\left\{R_f(t)\right\}, \tag{25}$$

where $\left\{p(t)\right\}$ is the vector of nodal pressures, and the global matrices are given by

$$\left[M_f\right] = \sum_{elements}\frac{\rho_f}{B_f}\int_\Phi \left[H(\vec{x})\right]^T\left[H(\vec{x})\right]dV\,, \tag{26}$$

$$\left[K_f\right] = \sum_{elements} \int_{\Phi} \left[F(\vec{x})\right]^T \left[F(\vec{x})\right] dV \,, \tag{27}$$

and

$$\left\{R_f(t)\right\} = \sum_{elements} \int_{\Psi_u} \rho_f \left[H(\vec{x})\right]^T \ddot{u}_n(\vec{x},t) dS \,, \tag{28}$$

where $\left[H(\vec{x})\right]$ is a row vector of interpolation functions, $\left[F(\vec{x})\right]$ is the matrix of spatial derivatives of the interpolation functions for the fluid, $\left[M_f\right]$ is referred to as the fluid mass matrix, $\left[K_f\right]$ is the fluid stiffness matrix, and $\left\{R_f(t)\right\}$ is the fluid external force vector.

1.3.6 Coupled System of Equations

The structural and fluid equations are coupled through their respective external force vectors. The fluid pressure at the fluid-structure interface translates to an external traction on the structure in the direction of the fluid normal, and the structural acceleration at the interface translates to the normal derivative of pressure on the fluid, which can be shown as

$$\boldsymbol{\sigma}(\vec{x},t)\vec{n}(\vec{x}) = -p(\vec{x},t)\vec{n}(\vec{x}) \quad \text{on } \Gamma_{fs} \tag{29}$$

and

$$\frac{\partial p(\vec{x},t)}{\partial \vec{n}_f(\vec{x})} = -\rho_f \ddot{\vec{u}}(\vec{x},t) \cdot \vec{n}_f(\vec{x}) \quad \text{on } \Gamma_{fs} \,, \tag{30}$$

where Γ_{fs} is the structural and fluid surface at the interface. The semi-discretized finite element equations for the coupled fluid-structure system can then be expressed as

$$\left[M\right]\left\{\ddot{u}(t)\right\} + \left\{I(t)\right\} = \left\{R(t)\right\} + \left[S\right]\left\{p(t)\right\} \tag{31}$$

and

$$\left[M_f\right]\left\{\ddot{p}(t)\right\} + \left[K_f\right]\left\{p(t)\right\} = -\left\{R_f(t)\right\} - \rho_f \left[S\right]^T \left\{\ddot{u}(t)\right\} \,, \tag{32}$$

where $\left[S\right]$ is the global interaction matrix defined by

$$\left[S\right] = \sum_{elements} \int_{\Gamma_{fs}} \left[N(\vec{x})\right]^T \vec{n}_f(\vec{x}) \left[H(\vec{x})\right] dS \,. \tag{33}$$

In this work, steady-state dynamic analysis is considered. For steady-state dynamic analysis, structural displacement, fluid pressure, and external forces are assumed to vary harmonically as

$$\left\{u(t)\right\} = \left[\left(\Re\left(\left\{\bar{u}(\omega)\right\}\right) + i\Im\left(\left\{\bar{u}(\omega)\right\}\right)\right)\right] e^{i\omega t}, \tag{34}$$

$$\left\{p(t)\right\} = \left[\Re\left(\left\{\bar{p}(\omega)\right\}\right) + i\Im\left(\left\{\bar{p}(\omega)\right\}\right)\right] e^{i\omega t}, \tag{35}$$

$$\left\{R(t)\right\} = \left[\Re\left(\left\{\bar{R}(\omega)\right\}\right) + i\Im\left(\left\{\bar{R}(\omega)\right\}\right)\right] e^{i\omega t}, \tag{36}$$

and

$$\left\{R_f(t)\right\} = \left[\Re\left(\left\{\bar{R}_f(\omega)\right\}\right) + i\Im\left(\left\{\bar{R}_f(\omega)\right\}\right)\right] e^{i\omega t}, \tag{37}$$

where $\left\{\bar{u}(\omega)\right\}$, $\left\{\bar{p}(\omega)\right\}$, $\left\{\bar{R}(\omega)\right\}$, and $\left\{\bar{R}_f(\omega)\right\}$ are the complex amplitudes of the steady-state response of the displacement, pressure, and external force vectors, respectively, and $\Re$ and $\Im$ denote real and imaginary components, respectively.

Defining the elastic and viscous stiffness matrices to be

$$\left[K^E\right] = \sum_{elements} \int_V [B]^T [C][B] dV \tag{38}$$

and

$$\left[K_m^V\right] = \sum_{elements} \int_V [B]^T \left[\tilde{C}_m\right][B] dV, \tag{39}$$

where $[C]$ and $\left[\tilde{C}_m\right]$ are the matrix conversions of the fourth-order tensors $\mathbf{C}^{IV}$ and $\tilde{\mathbf{C}}_m^{IV}$, respectively, to Voigt notation. Then substituting the harmonic variables, and equating real terms and imaginary terms, the coupled system of equations becomes

$$\begin{bmatrix} [A] & -[D] & -[S] & 0 \\ [D] & [A] & 0 & -[S] \\ -\omega^2\rho_f[S]^T & 0 & [L] & 0 \\ 0 & -\omega^2\rho_f[S]^T & 0 & [L] \end{bmatrix} \begin{Bmatrix} \Re\left(\left\{\bar{u}(\omega)\right\}\right) \\ \Im\left(\left\{\bar{u}(\omega)\right\}\right) \\ \Re\left(\left\{\bar{p}(\omega)\right\}\right) \\ \Im\left(\left\{\bar{p}(\omega)\right\}\right) \end{Bmatrix} = \begin{Bmatrix} \Re\left(\left\{\bar{R}(\omega)\right\}\right) \\ \Im\left(\left\{\bar{R}(\omega)\right\}\right) \\ -\Re\left(\left\{\bar{R}_f(\omega)\right\}\right) \\ -\Im\left(\left\{\bar{R}_f(\omega)\right\}\right) \end{Bmatrix}, \tag{40}$$

where

$$[A] = -\omega^2[M] + \left[K^E\right] + \sum_{m=1}^{n} \frac{\omega^2\tau_m^2}{1+\omega^2\tau_m^2}\left[K_m^V\right], \tag{41}$$

$$[D] = \sum_{m=1}^{n} \frac{\omega\tau_m}{1+\omega^2\tau_m^2}\left[K_m^V\right], \tag{42}$$

and

$$[L] = -\omega^2 [M_f] + [K_f]. \tag{43}$$

1.4 Inverse Problem

The inverse problem considered in this work was to determine elastic and viscoelastic parameters defining the constitutive relationship of a solid immersed in fluid using acoustic emissions. These material parameters were to be determined through the measured steady-state acoustic pressure response in the surrounding fluid, $\overline{p}(x,\omega)$, given the geometry and boundary conditions of the system.

The inverse problem was cast as an optimization problem, in which the goal was to determine a set of parameters that minimizes the difference between a physical and a calculated response. Typically this can be outlined as the minimization of an error measure, which was defined in this work to be the l^2-norm of the discrete response error, given by

$$E(\underset{\sim}{a}) = \sqrt{\sum_{i=1}^{n} \left[p_i^{\exp} - p_i^s(\underset{\sim}{a}) \right]^2}, \tag{44}$$

where $\underset{\sim}{a}$ is the vector of parameters to be estimated, n is the number of discrete frequencies sampled from the measured response, $p_i^{\exp}$ is the pressure at a given fluid point corresponding to the i^{th} frequency of the test response, and $p_i^s(\underset{\sim}{a})$ is the pressure corresponding to the i^{th} frequency computed using finite element analysis.

1.4.1 Optimization Algorithm

The optimization algorithm used in this work is a combination of a classical random search algorithm with a more recently developed surrogate-model (or meta-model) approach. This algorithm is referred to as the Surrogate-Model Accelerated Random Search (SMARS). SMARS takes advantage of the global convergence capabilities of the random search (RS) algorithm, while accelerating the search by

applying the more cost effective surrogate-model approach.

The RS method, originally outlined by Brooks [9], was used as one of the major foundations of this work. The most general form of the RS method consists of probing the solution space by generating sets of parameters randomly and computing the corresponding response error for each set. Next, sets of parameters are randomly generated in a neighborhood of the current best parameter set. The process is repeated until the minimum response error decreases below a predefined tolerance or a maximum number of trials is reached. The trial parameter sets are selected based on some probability distribution (e.g. normal distribution) centered about the current best parameter set. Validity was given to the random method in Masri, Smyth, Chassiakos, Nakamura, and Caughey [27] as the RS algorithm was shown to exhibit global convergence in a probabilistic sense.

In addition to the global convergence capabilities, the RS method is not strongly affected by the size of the search space and the initial parameter estimates. The downfall of the RS method is that many function evaluations are often required to locate a reasonable solution. In cases where computationally expensive numerical models are used such as finite element analysis, the RS method may become unfeasible. In recent applications of the RS method, heuristic techniques have been developed in an attempt to increase the speed of convergence while maintaining the global search capabilities [27, 37].

Surrogate-model methods have been developed to limit the number of numerical model evaluations required to find an optimal solution [26, 31, 34, 35, 39]. Typically, in a surrogate model approach, nonlinear mapping tools, such as radial basis functions, artificial neural networks, and support vector machines, are used to approximate the response of a computationally expensive numerical model (e.g. a finite element model). An approximation to the inverse problem solution is then obtained with the

surrogate-model used in place of the expensive numerical model.

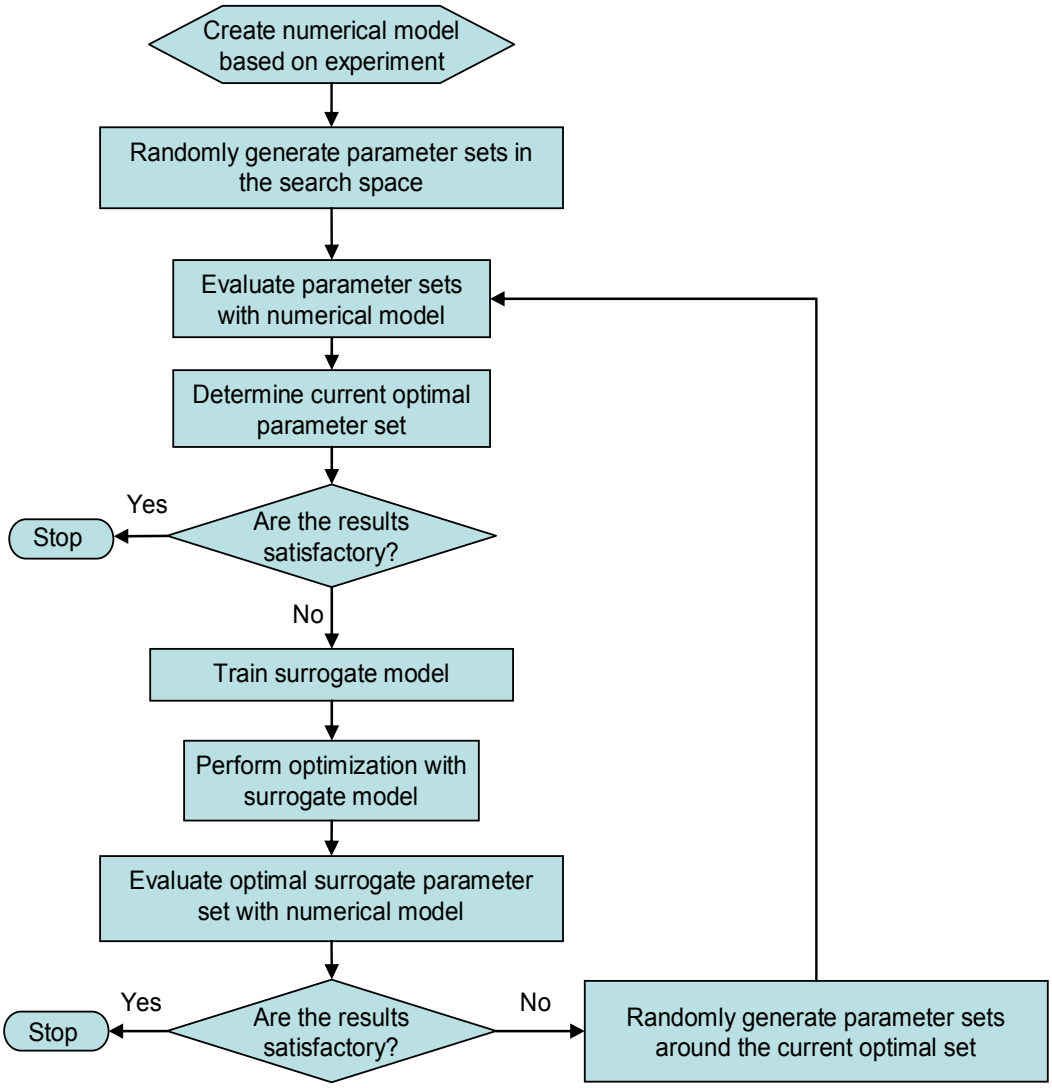

Figure 1.2. Flow chart for the Surrogate Model Accelerated Random Search algorithm

The SMARS algorithm is an iterative application of the random search and surrogate-model methods described above. Figure 1.2 shows a flowchart that describes the SMARS algorithm. In the initial step of the algorithm, parameter sets are randomly generated and the corresponding responses are evaluated using the

numerical model. This initial set of parameters and responses is used to both determine a starting point for the random search and to act as an initial training set for the surrogate model. For this work, an artificial neural network (ANN) was used as the surrogate-model to approximate the numerical model (for a complete description of ANNs and training approaches the reader is referred to Reed and Marks [33]). The surrogate model is then trained to become an approximate mapping to the response of the numerical model, relating parameter sets to the model output response. Once trained, the surrogate model is used to estimate an optimal parameter set using a global optimization method. In this work, a hybrid direct search-genetic algorithm strategy was used for this purpose. The surrogate model estimate is then evaluated through the numerical model to obtain the actual response of the parameter set. If the optimal parameter set yields an error below a predefined tolerance, the algorithm ends, otherwise the random search continues by generating additional random parameter sets in the neighborhood of the current optimal set, and the process is repeated.

1.5 Examples and Discussion

Several examples were considered to demonstrate the feasibility of the proposed approach to non-invasively estimate the viscoelastic material properties of a solid from acoustic emissions. In all cases, the frequency response of a solid immersed in a fluid was obtained by applying a harmonic pressure to the body over a range of frequencies and measuring the steady-state acoustic field (i.e. fluid pressure) at a point in the surrounding fluid. Discrete points were then sampled from the frequency response functions and used with the SMARS algorithm to inversely estimate the elastic and viscoelastic properties of the vibrating body. The numerical simulations of the experiments were performed using steady-state dynamic finite element analysis as described in Section 1.3. In all cases, the finite element models were thoroughly

checked for mesh convergence over the admissible ranges of material parameters considered.

First, three numerical examples were considered in which an experiment was simulated through finite element analysis to create the test data. To explore the robustness of the SMARS algorithm, five independent optimization runs of each simulated example were carried out, and the mean and standard deviation of the results were calculated. The three simulated experiments consisted of a viscoelastic cylinder, a soft viscoelastic rectangular prism with a hard elastic cylindrical inclusion, and a soft tissue sphere with a spherical ice inclusion. Water was used as the acoustic medium surrounding the solids in all three cases.

Each simulated experiment had artificial random Gaussian noise added to the response data in order to explore the tolerance of the SMARS algorithm to imperfect data. The random Gaussian noise was introduced in the simulated data as

$$p_i^{error} = p_i^{exact}\left(1+0.1\eta\right), \tag{45}$$

where p_i^{error} is the i^{th} response point containing the random noise, p_i^{exact} is the i^{th} response point of the simulated test without noise, and η is a normally distributed random variable with unit variance and zero mean. It was found that this equation produced realistic values of acoustic pressure deviations. Furthermore, the noise was added to relieve the inverse crime of using the same numerical model to simulate the experiment as to perform the optimization simulations. Although limitations inevitably exist when using simulated experiments, in order to represent realistic scenarios, a well developed numerical model with artificial noise is considered sufficient for the purposes of this work.

In addition, a physical experiment was used to further validate the methodology, and test the SMARS optimization technique without the inverse crime of a simulated experiment. The experiment consisted of a chalk sphere immersed in a tank of water.

The sphere was vibrated by a pressure force created remotely using ultrasound, and the acoustic pressure was measured using a hydrophone at a point within the surrounding fluid.

In all cases the surrounding fluid was modeled as an infinite domain. Furthermore, for each optimization case, the unknown parameters were constrained to a specific search range. Although the SMARS algorithm is a method for unconstrained optimization, it is reasonable to assume that material parameters can be bound within a certain range.

For the examples, only isotropic viscoelastic materials are considered for the sake of simplicity. Oftentimes, isotropic viscoelastic response is defined with two independent functions of frequency such as complex viscoelastic bulk and shear moduli. In the work presented by Urban, Kinnick, and Greenleaf [38], the material behavior was represented by a complex shear modulus and a purely elastic bulk modulus. In a similar manner, for this work, the material was defined by a constant Poisson's ratio and a complex Young's modulus given by

$$E^*(\omega) = E + \sum_{m=1}^{n} \tilde{E}_m \left(\frac{\omega^2 \tau_m^2 + i\omega\tau_m}{1 + \omega^2 \tau_m^2} \right). \tag{46}$$

Thus, the isotropic viscoelastic constitutive model can be described through the long-term elastic Young's modulus E, the viscous Young's moduli $\tilde{E}_m$, the Poisson's ratio υ, and the relaxation times τ_m. In the results presented, the viscous Young's moduli are expressed through a dimensionless viscous Young's moduli, g_m, given by

$$g_m = \frac{\tilde{E}_m}{E + \sum_{i=1}^{n} \tilde{E}_i}. \tag{47}$$

It is important to realize that different combinations of viscoelastic parameters (i.e. $E, \tilde{E}_m, \tau_m$), or even different viscoelastic rheological representations can result in

the same material behavior over a given time period or frequency range. This non-uniqueness not only causes difficulty in deriving physical meaning from the viscoelastic parameters, but also causes problems for any inverse characterization strategy. Alternatively, a viscoelastic material may be uniquely characterized by more physically relevant quantities, such as energy storage and dissipation over time or frequency. In the frequency domain, which is considered for this work, energy dissipation and storage can be expressed through the mechanical loss, $\tan\left[\delta(\omega)\right]$, which is associated with viscous damping, and the equivalent elastic modulus, $E^{eq}(\omega)$, respectively. The mechanical loss and equivalent elastic modulus are defined as the ratio of the imaginary to the real portion of the complex relaxation modulus, and the magnitude of the complex modulus, respectively. For the complex Young's modulus considered here these quantities are given by

$$\tan(\delta) = \left[\sum_{m=1}^{n} \tilde{E}_m \left(\frac{\omega\tau_m}{1+\omega^2\tau_m^2}\right)\right] \Bigg/ \left[E + \sum_{m=1}^{n} \tilde{E}_m \left(\frac{\omega^2\tau_m^2}{1+\omega^2\tau_m^2}\right)\right], \tag{48}$$

and

$$E^{eq}(\omega) = \left\{\left[\sum_{m=1}^{n} \tilde{E}_m \left(\frac{\omega\tau_m}{1+\omega^2\tau_m^2}\right)\right]^2 + \left[E + \sum_{m=1}^{n} \tilde{E}_m \left(\frac{\omega^2\tau_m^2}{1+\omega^2\tau_m^2}\right)\right]^2\right\}^{1/2}. \tag{49}$$

Although the generalized Maxwell model parameters defining these characteristics may be non-unique, the characteristic functions themselves uniquely define the material behavior. Therefore, in the following examples the results are expressed in terms of these viscoelastic characteristic functions, $\tan\left[\delta(\omega)\right]$ and $E^{eq}(\omega)$, resulting from the inversely determined viscoelastic moduli.

1.5.1 Example 1: Simulated Viscoelastic Cylinder in Water

The first example consisted of a cylinder with a 7.5 mm radius, immersed in water, and with a pressure line applied to a portion of the perimeter, as shown in Figure 1.3

(a). The experiment was simulated with a plane strain finite element model as shown in Figure 1.3 (b). The material was represented with a generalized Maxwell model with one Maxwell unit. The density of the solid was assumed to be known and was taken as $1050\,kg/m^3$, while the density of the surrounding water was $1000\,kg/m^3$. Plane strain was selected for this example to decrease computation time.

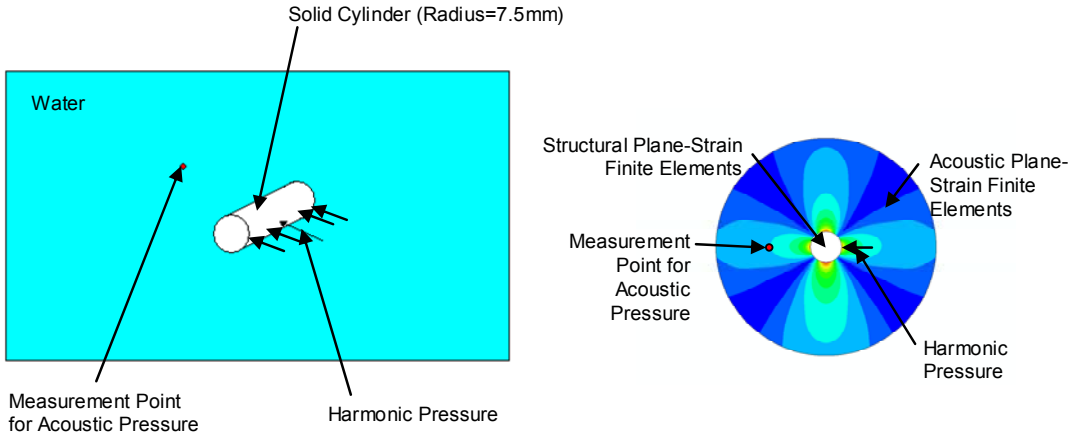

Figure 1.3. (a) Schematic and (b) finite element model of the simulated experiment for Example 1: simulated viscoelastic cylinder in water.

Table 1.1. Experimental material properties and optimization search ranges for Example 1: simulated viscoelastic cylinder in water.

Optimization Parameter	Target Value	Optimization Minimum	Optimization Maximum
E	$3.19\text{x}10^{9}$	$1.0\text{x}10^{8}$	$1.0\text{x}10^{10}$
ν	0.26	0.20	0.48
g	0.1	0.01	0.99
τ	$1.0\text{x}10^{-6}$	$1.0\text{x}10^{-7}$	$1.0\text{x}10^{-5}$

Table 1.1 shows the material properties used for the simulated experiment and the search ranges used for the optimization process. The parameters to be identified for this example were the long-term elastic Young's modulus, E, the dimensionless viscous Young's modulus, g, Poisson's ratio, ν, and the relaxation time, τ. Figure 1.4 shows the frequency response for the magnitude of the complex acoustic pressure at a given point in the surrounding fluid and the sampled points that were used to obtain the inverse solution.

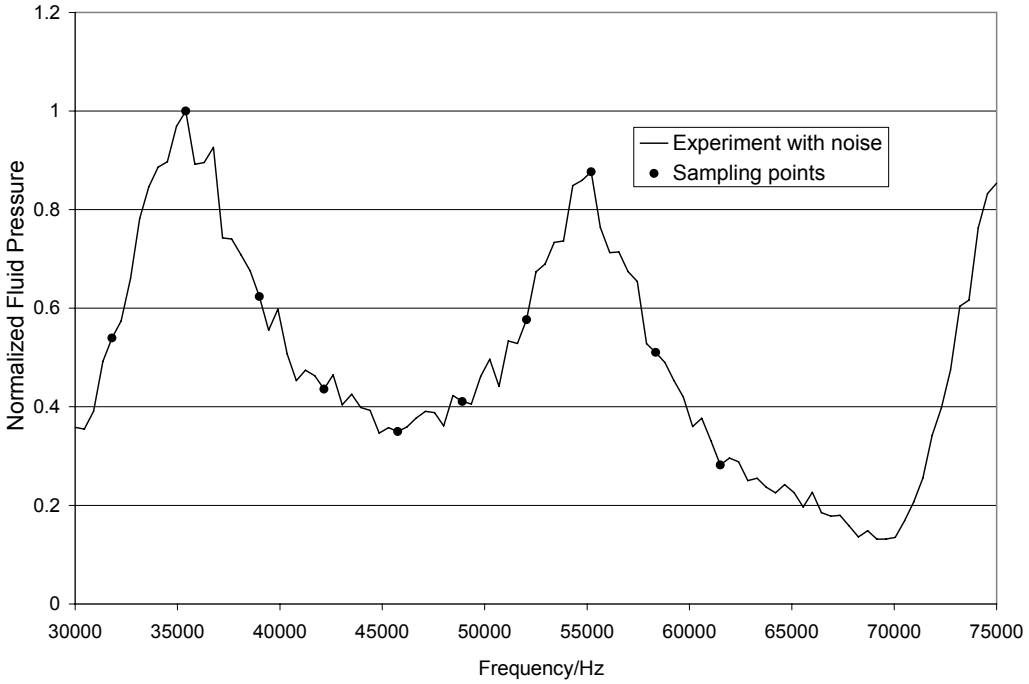

Figure 1.4. Frequency response of normalized acoustic pressure and discrete sampling points used for optimization for Example 1: simulated viscoelastic cylinder in water.

Figure 1.5 shows the mean and standard deviation of the acoustic pressure frequency responses computed from five optimization trials. These results are compared to the simulated experiment with artificial noise. Table 1.2 shows the material parameters found in the five optimization trials. It is clear from Figure 1.5 that the estimated parameters produced responses in agreement with the experimental response.

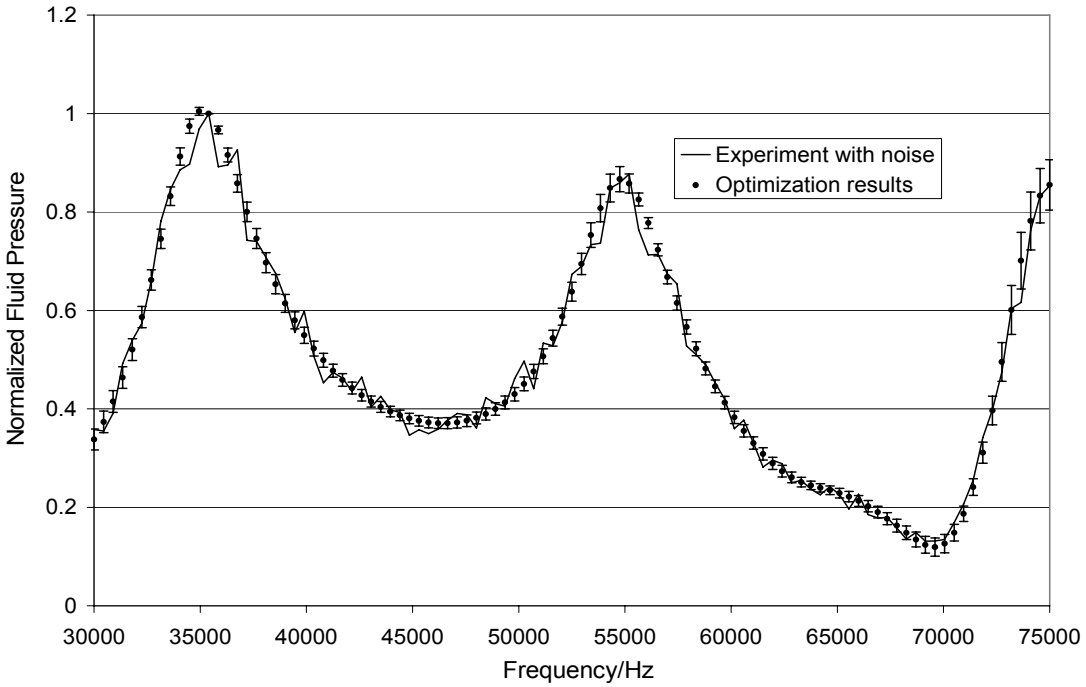

Figure 1.5. Frequency response of normalized acoustic pressure for optimization results compared to the simulated experiment for Example 1: simulated viscoelastic cylinder in water. The optimization results show the mean and standard deviation (error bars) of the five trials.

Table 1.2. Optimization results for the five optimization trials for Example 1: simulated viscoelastic cylinder in water.

	E	ν	g	τ
Actual	$3.19\text{x}10^{9}$	0.26	0.10	$1\text{x}10^{-6}$
Trial 1	$3.21\text{x}10^{9}$	0.28	0.14	$5.39\text{x}10^{-7}$
Trial 2	$3.15\text{x}10^{9}$	0.23	0.065	$2.68\text{x}10^{-6}$
Trial 3	$3.22\text{x}10^{9}$	0.30	0.12	$5.85\text{x}10^{-7}$
Trial 4	$3.23\text{x}10^{9}$	0.27	0.13	$3.44\text{x}10^{-7}$
Trial 5	$3.24\text{x}10^{9}$	0.26	0.17	$4.87\text{x}10^{-7}$
Mean	$3.21\text{x}10^{9}$	0.27	0.13	$9.26\text{x}10^{-7}$
Std. Dev.	$3.33\text{x}10^{7}$	0.025	0.039	$9.82\text{x}10^{-7}$

The results show, as expected, that the Generalized Maxwell model parameters such as dimensionless viscous Young's modulus and relaxation time are non-unique. This can be inferred from the large fluctuation of these values in the five trials (Table 1.2).

Therefore, to better understand the optimization results, the viscoelastic characteristics described in Equations (48) and (49) were analyzed. Figure 1.6 and Figure 1.7 show the mean and standard deviation of the mechanical loss and equivalent elastic modulus versus frequency, respectively, for the results of the five optimization trials. These results are compared to the characteristics resulting from the given material parameters. The identification of the equivalent elastic modulus was excellent over the frequency range examined, and the low deviation amongst trials is an indication that this parameter has a strong effect on the frequency response of the material. The identification of Poisson's ratio was slightly less accurate, yet still acceptable. The identification of the mechanical loss showed the lowest accuracy of the parameters investigated. The low accuracy and strong deviation between trials is likely due to the small amount of damping included in the system through the viscoelastic model, resulting in a relatively low effect of the mechanical loss on the frequency response.

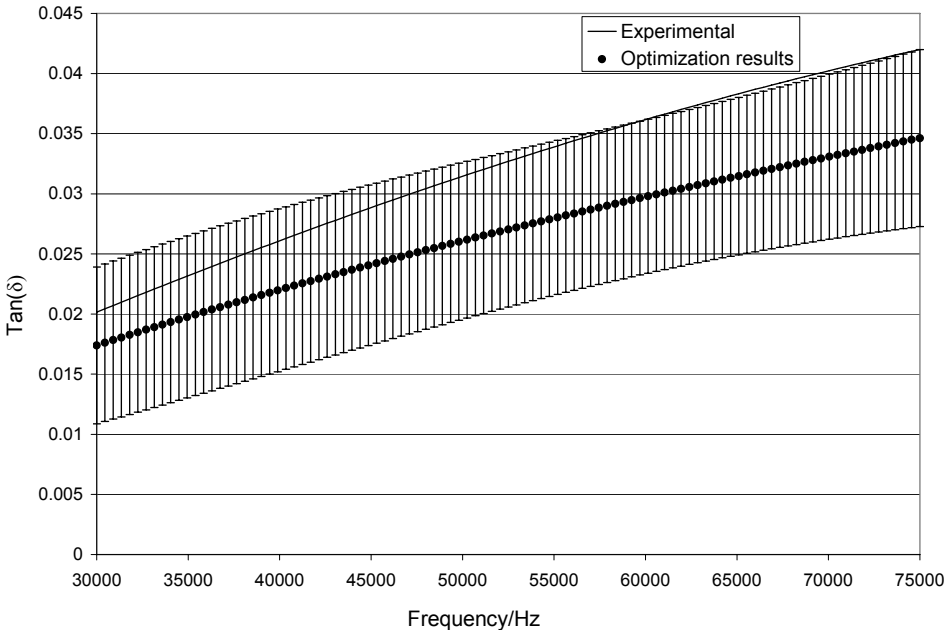

Figure 1.6. Frequency distribution of the mechanical loss ($\tan(\delta)$), for the optimization results for Example 1: simulated viscoelastic cylinder in water. The optimization results show the mean and standard deviation (error bars) of the five trials.

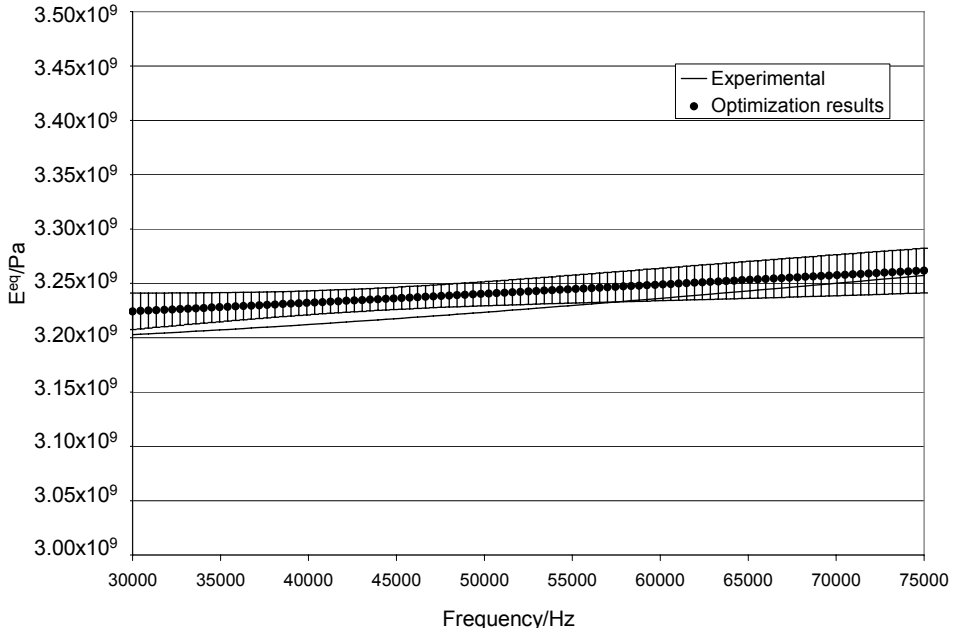

Figure 1.7. Frequency distribution of the equivalent elastic modulus (E^{eq}), for the optimization results for Example 1: simulated viscoelastic cylinder in water. The optimization results show the mean and standard deviation (error bars) of the five trials.

1.5.2 Example 2: Simulated Soft Prism with Hard Cylindrical Inclusion

The second example consisted of a rectangular prism with cross-sectional dimensions 6 cm x 4 cm, immersed in water, with a cylindrical inclusion of 7.5 mm radius, as shown in Figure 1.8 (a). A harmonic pressure line was applied to a portion of the perimeter of the cylindrical inclusion. Again, the experiment was simulated with a plane strain finite element model to alleviate computational time, as shown in Figure 1.8 (b). For this case the inclusion was assumed to be purely elastic. The rectangular prism was taken to be a softer material with a viscoelastic material model represented by a generalized Maxwell model with one Maxwell unit. Both materials were given a density of $1050\,kg/m^3$. Table 1.3 shows the material properties used for the simulated experiment and the search ranges used for the optimization process. The parameters to be identified for this example were the Young's modulus for the elastic inclusion, E_1, the long-term elastic Young's modulus for the surrounding material, E_2, the dimensionless viscous Young's modulus for the surrounding material, g_2, and the relaxation time for the surrounding material, τ_2. It is important to note that the search range for the elastic moduli was the same for both materials. By using the same search range, no assumption is made as to whether the inclusion was hard or soft, thus maintaining generality. For this example, both materials were considered to be nearly incompressible (i.e. $\nu \approx 0.5$). In addition, it was assumed that only the viscoelastic properties of the surrounding material were of interest, and the hard inclusion would depict purely elastic behavior. This material distribution could resemble, for instance, the presence of calcifications in breast tissue.

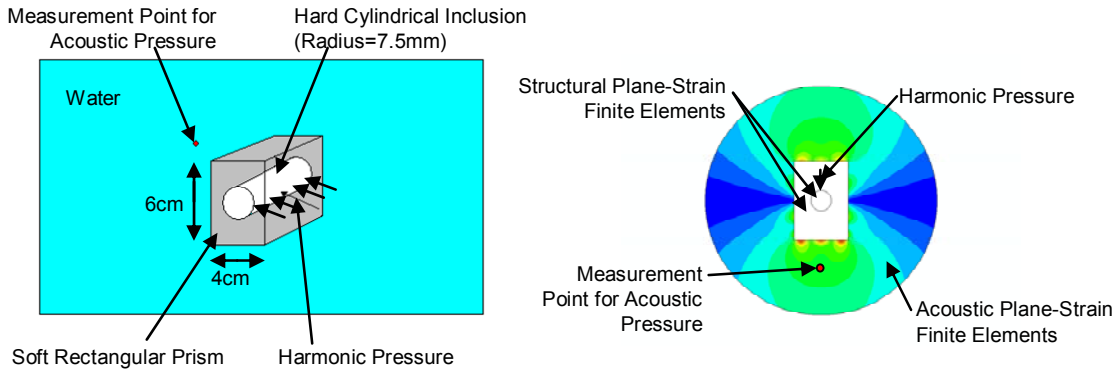

a) **b)**

Figure 1.8. (a) Schematic and (b) finite element model of the simulated experiment for Example 2: simulated soft prism with hard cylindrical inclusion.

Table 1.3. Experimental material properties and optimization search ranges for Example 2: simulated soft prism with hard cylindrical inclusion.

	Target Value	Optimization Minimum	Optimization Maximum
E_1	3.19×10^9	1.0×10^8	5.0×10^9
E_2	2.5×10^8	1.0×10^8	5.0×10^9
g_2	0.50	0.01	0.99
τ_2	1.0×10^{-6}	1.0×10^{-7}	1.0×10^{-4}

Figure 1.9 shows the frequency response for the magnitude of the acoustic pressure at a given point in the surrounding fluid, and the sampled discrete points used for the inverse solution. Figure 1.10 shows the mean and standard deviation of the acoustic pressure frequency response obtained from the five optimization trials. These results are also compared to the response from the simulated experiment with artificial noise. It can be observed in Figure 1.10 that the experimental frequency response was closely matched.

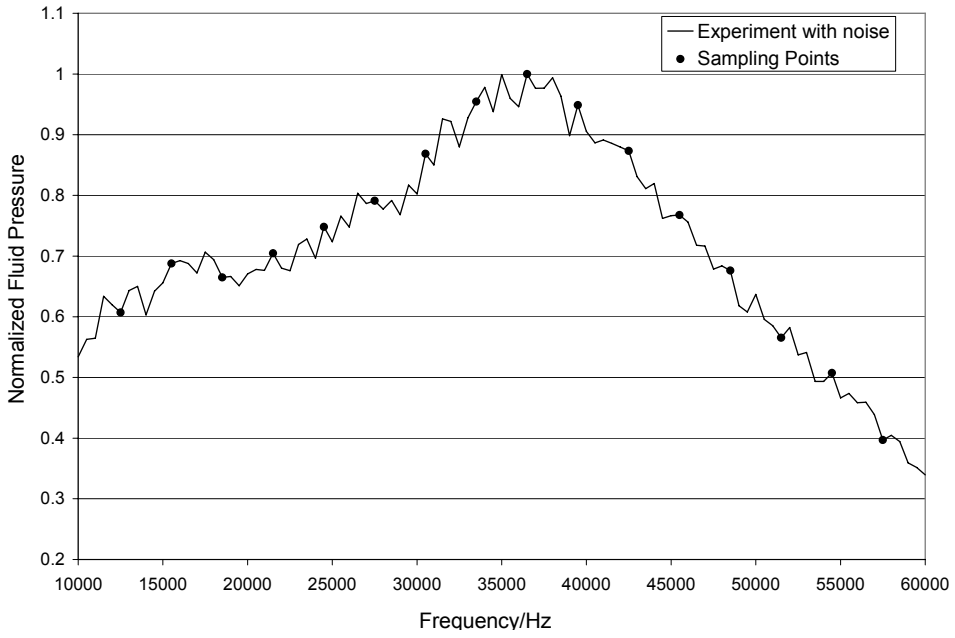

Figure 1.9. Frequency response of normalized acoustic pressure and discrete sampling points used for optimization for Example 2: simulated soft prism with hard cylindrical inclusion.

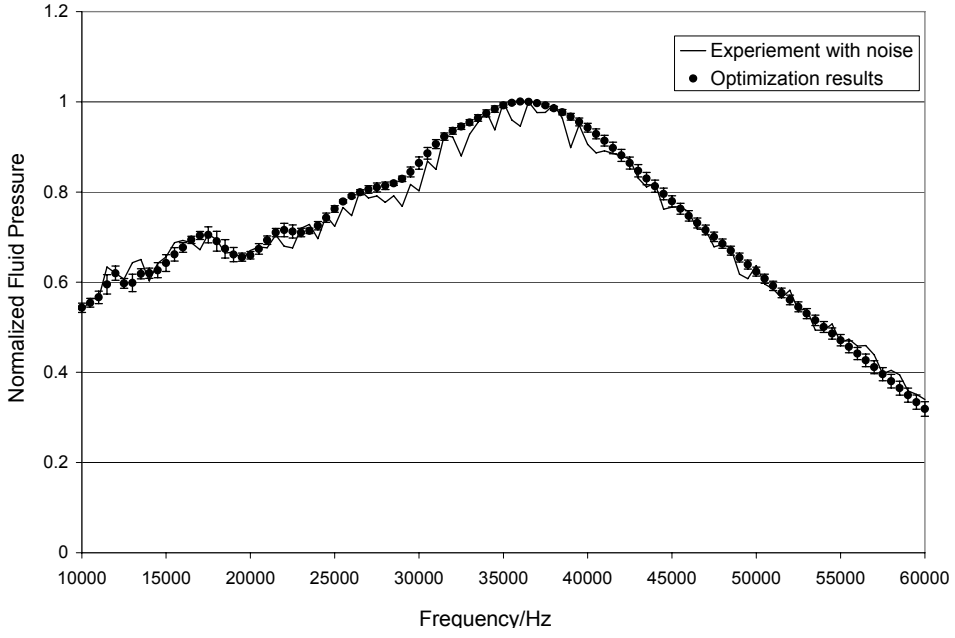

Figure 1.10. Frequency response of normalized acoustic pressure for optimization results compared to the simulated experiment for Example 2: simulated soft prism with hard cylindrical inclusion. The optimization results show the mean and standard deviation (error bars) of the five trials.

Table 1.4 shows the material parameters found in the five optimization trials. Figure 1.11 and Figure 1.12 show the mean and standard deviation of the soft matrix mechanical loss and equivalent elastic modulus, respectively. Both elastic moduli (equivalent elastic modulus of the matrix and Young's modulus of the inclusion) were accurately found. It is important to emphasize the significance that the algorithm was able to extract from the frequency response which material was harder, without *a priori* information. For this case, the viscoelastic characteristics, particularly the mechanical loss, were found with a higher level of accuracy and precision than in the previous example. This is likely due to the fact that the surrounding material had a larger amount of damping due to the viscoelastic model in this case than in the previous example, and as such, the mechanical loss had a stronger influence on the frequency response.

Table 1.4. Optimization results for the five optimization trials for Example 2: simulated soft prism with hard cylindrical inclusion.

	E_1	E_2	g_2	τ_2
Actual	$3.19\text{x}10^{9}$	$2.50\text{x}10^{8}$	0.50	$1.00\text{x}10^{-6}$
Trial 1	$3.01\text{x}10^{9}$	$2.73\text{x}10^{8}$	0.67	$3.96\text{x}10^{-7}$
Trial 2	$3.20\text{x}10^{9}$	$2.42\text{x}10^{8}$	0.80	$2.22\text{x}10^{-7}$
Trial 3	$3.14\text{x}10^{9}$	$2.61\text{x}10^{8}$	0.79	$2.32\text{x}10^{-7}$
Trial 4	$3.05\text{x}10^{9}$	$2.59\text{x}10^{8}$	0.80	$2.09\text{x}10^{-7}$
Trial 5	$3.27\text{x}10^{9}$	$2.68\text{x}10^{8}$	0.73	$3.26\ \text{x}10^{-7}$
Mean	$3.130\text{x}10^{9}$	$2.61\text{x}10^{8}$	0.76	$2.77\text{x}10^{-7}$
Std. Dev.	$0.106\text{x}10^{9}$	$1.19\text{x}10^{7}$	0.057	$8.09\text{x}10^{-8}$

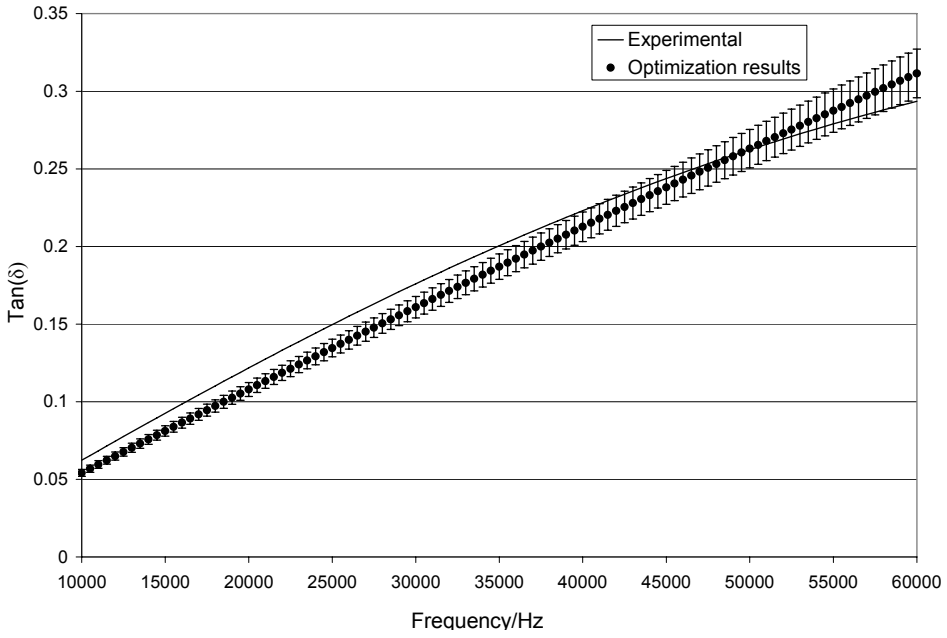

Figure 1.11. Frequency distribution of the mechanical loss ($\tan(\delta)$), for the optimization results for Example 2: simulated soft prism with hard cylindrical inclusion. The optimization results show the mean and standard deviation (error bars) of the five trials.

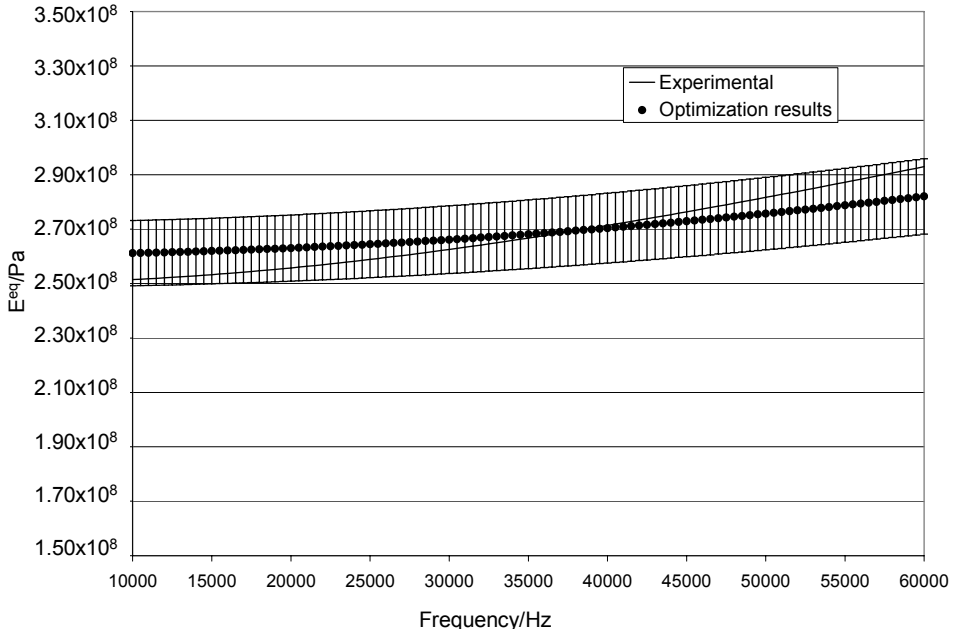

Figure 1.12. Frequency distribution of the equivalient elastic modulus (E^{eq}), for the optimization results for Example 2: simulated soft prism with hard cylindrical inclusion. The optimization results show the mean and standard deviation (error bars) of the five trials.

1.5.3 Example 3: Simulated Tissue with Ice Sphere Inclusion

The third example presents a simulated experiment for the identification of material changes during cryoablation. Cryoablation is a process in which localized regions of undesirable tissue are destroyed through freezing, see Rubinsky [36] and Baust, Gage, Ma, and Zhang [8]. Inverse estimation of the material properties of frozen and unfrozen tissue could be used for tracking the progress of cryoablation during clinical procedures. Axisymmetric finite elements were used to model an ice sphere with a 1.5 cm radius embedded in a soft tissue sphere with a 5 cm radius. A pressure was applied to a small region on the surface of the sphere, and the acoustic pressure amplitude was determined at a point within the surrounding acoustic medium as shown in Figure 1.13 (a). The axisymmetric finite element model developed to represent the experiment is shown in Figure 1.13 (b).

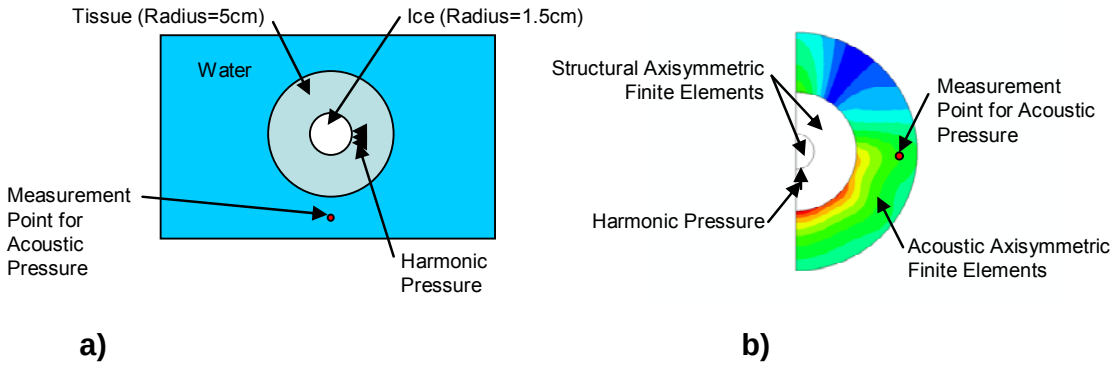

Figure 1.13. (a) Schematic and (b) finite element model of the simulated experiment for Example 3: simulated tissue with ice sphere inclusion.

The ice was considered to be a linear elastic material, which is reasonable for the frequencies considered [32], while the tissue was considered to be a highly viscous material represented by a generalized Maxwell model with one Maxwell unit. Table 1.5 shows the material properties used for the simulated experiment and the search

ranges used for the optimization process. The elastic parameters used for the ice were based on the values presented in Pounder [32]. The viscoelastic parameters used for the tissue were based on a combination of the elastic parameters reported in Duck[14] for soft tissue and the viscoelastic parameters reported in Urban, Kinnick, and Greenleaf[38] for mammalian tissue. The density of both materials was considered to be close to the density of water ($1000\,kg/m^3$), which is a reasonable approximation for both soft biological tissues and ice. The tissue was considered to be nearly incompressible, whereas, the Poisson's ratio for ice was taken to be 0.33, and considered unknown in this problem. Therefore, the parameters to be identified for this example were Young's modulus for the ice, E_1, Poisson's ratio for the ice, ν_1, the long-term elastic Young's modulus for the surrounding tissue, E_2, the dimensionless viscous Young's modulus for the surrounding tissue, g_2, and the relaxation time for the surrounding tissue, τ_2. For this case, it was considered reasonable to assume that the inclusion was harder than the surrounding material. Figure 1.14 shows the frequency response for the acoustic pressure amplitude of a point in the surrounding fluid, and the sampled discrete points used in the inverse solution.

Table 1.5. Experimental material properties and optimization search ranges for Example 3: simulated tissue with ice sphere inclusion.

Optimization Parameter	Target Value	Optimization Minimum	Optimization Maximum
E_1	$7.0\text{x}10^9$	$1.0\text{x}10^9$	$1.0\text{x}10^{10}$
ν_1	0.33	0.20	0.49
E_2	$5.0\text{x}10^5$	$1.0\text{x}10^5$	$1.0\text{x}10^6$
g_2	0.5	0.01	0.99
τ_2	$1.0\text{x}10^{-6}$	$1.0\text{x}10^{-7}$	$1.0\text{x}10^{-4}$

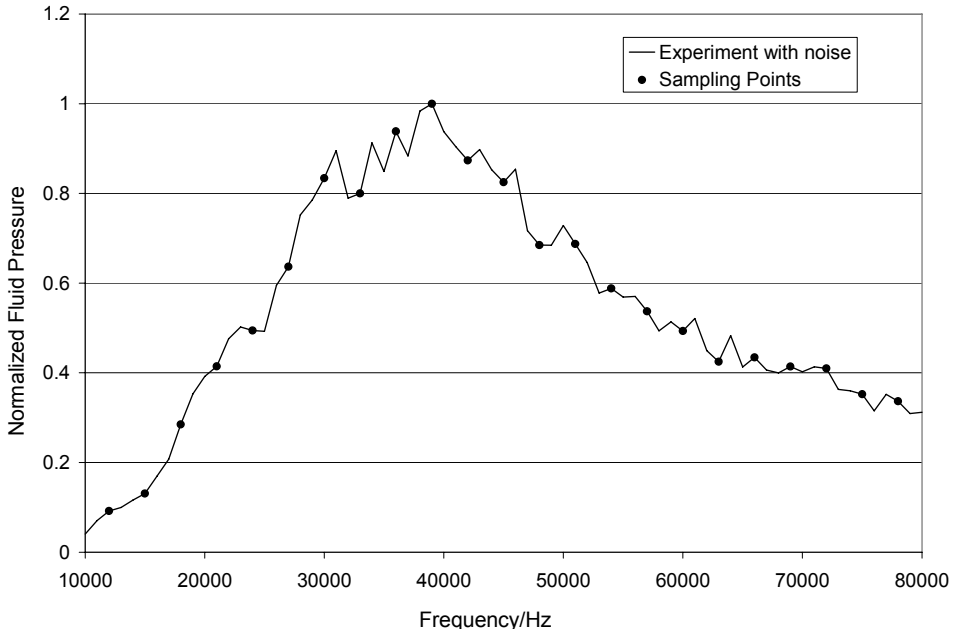

Figure 1.14. Frequency response of normalized acoustic pressure and discrete sampling points used for optimization for Example 3: simulated tissue with ice sphere inclusion.

Figure 1.15 shows the mean and standard deviation of the acoustic pressure frequency responses obtained from the five optimization trials. Table 1.6 shows the parameter results obtained from the optimization trials. Figure 1.16 and Figure 1.17 show the mean and standard deviation of the mechanical loss and equivalent elastic modulus, respectively, for the tissue. It is first important to note that the deviation of the response for the results of the optimization trials was larger for this example than for the previous simulated examples. However, even though the response deviation was larger, it is clear that the SMARS algorithm continued to obtain parameters that matched the target response to a satisfactory extent.

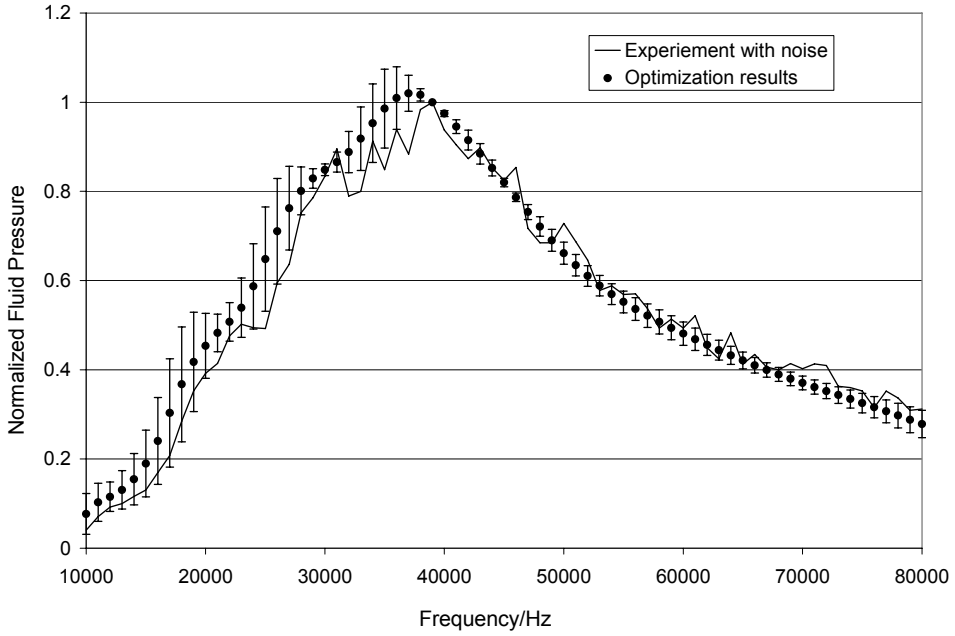

Figure 1.15. Frequency response of normalized acoustic pressure for the optimization results compared to the simulated experiment for Example 3: simulated tissue with ice sphere inclusion. The optimization results show the mean and standard deviation (error bars) of the five trials.

Table 1.6. Optimization results for the five optimization trials for Example 3: simulated tissue with ice sphere inclusion.

	E_1	ν_1	E_2	g_2	τ_2
Actual	7.00×10^{9}	0.33	5.00×10^{5}	0.50	1.00×10^{-6}
Trial 1	6.96×10^{9}	0.37	5.10×10^{5}	0.51	8.90×10^{-7}
Trial 2	6.98×10^{9}	0.38	5.23×10^{5}	0.56	6.06×10^{-7}
Trial 3	6.89×10^{9}	0.31	3.68×10^{5}	0.52	1.53×10^{-6}
Trial 4	6.32×10^{9}	0.36	4.15×10^{5}	0.51	1.01×10^{-6}
Trial 5	6.61×10^{9}	0.29	3.80×10^{5}	0.50	1.39×10^{-6}
Mean	6.75×10^{9}	0.34	4.39×10^{5}	0.52	1.09×10^{-6}
Std. Dev.	2.85×10^{8}	0.041	7.28×10^{4}	0.024	3.76×10^{-7}

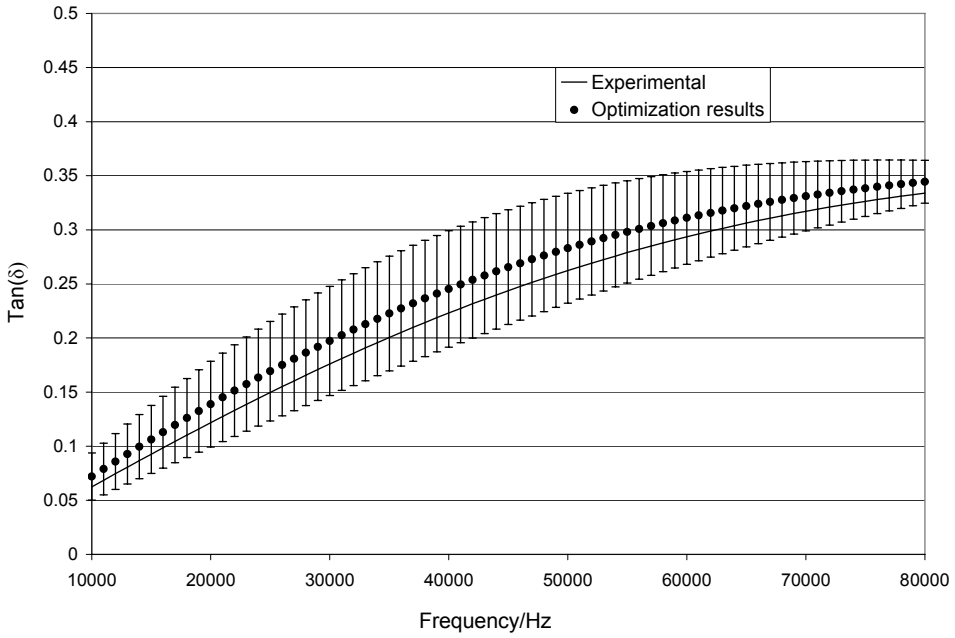

Figure 1.16. Frequency distribution of the mechanical loss ($\tan(\delta)$), for the optimization results for Example 3: simulated tissue with ice sphere inclusion. The optimization results show the mean and standard deviation (error bars) of the five trials.

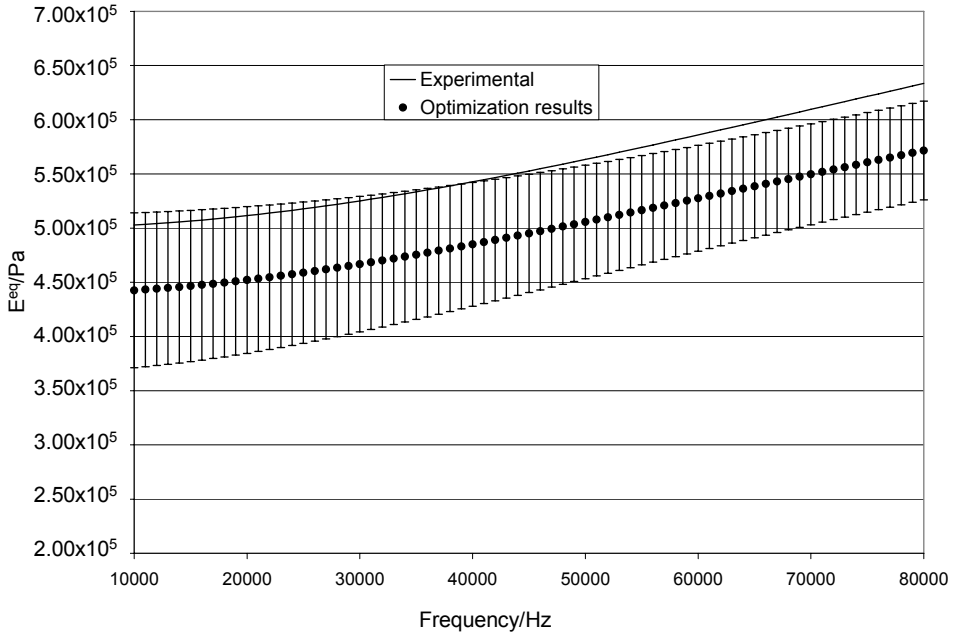

Figure 1.17. Frequency distribution of the equivalient elastic modulus (E^{eq}), for the optimization results for Example 3: simulated tissue with ice sphere inclusion. The optimization results show the mean and standard deviation (error bars) of the five trials.

The elastic modulus of the ice was found with a high level of accuracy, but the results were less accurate for Poisson's ratio. Through sensitivity studies on the material parameters, it was found that the acoustic response displayed little sensitivity to changes in Poisson's ratio of the ice, while the elastic modulus of the ice showed strong sensitivity, which explains the comparative scatter and lack of accuracy for Poisson's ratio. Furthermore, the results found for the mechanical loss of the tissue showed satisfactory accuracy, but with moderate variation, whereas the equivalent elastic modulus of the tissue was found with lower accuracy and larger scatter. The sensitivity studies carried out revealed that the acoustic pressure was more affected by changes in the dimensionless viscous Young's modulus of the tissue than by changes in the long-term elastic Young's modulus of the tissue. Therefore, due to the relative dependencies of the characteristic functions on these parameters, this difference in sensitivity resulted in a more accurate identification of the mechanical loss than the equivalent elastic modulus of the tissue.

Clearly, the modes that appear in the frequency range studied in this example are very sensitive to the Young's modulus of the ice, but not to the equivalent elastic modulus of the tissue. It is likely that a more accurate identification of the equivalent elastic modulus of the surrounding tissue could be obtained if other frequency ranges were investigated. Though, for the purposes of this work and as pertains to cryoablation applications, it was considered more pertinent to identify the ice stiffness accurately, and a frequency range was chosen which was likely to excite the modes of the stiffer material.

1.5.4 Vibroacoustic Experiment: Chalk Sphere in Water

The experiment shown in Mitri [28] consisted of suspending a 15 mm – diameter chalk sphere at the focus of a spherically focused piezoelectric transducer divided into

two equal area elements that produce the ultrasound fields. The acoustic emission was recorded by means of a low-frequency hydrophone (the complete experimental procedure is described in Mitr i[28]). Two resonance peaks were detected at 45.5 and 68.5 kHz, respectively, by varying the difference frequency in the 20–75 kHz frequency bandwidth.

An axisymmetric finite element model was developed to model an idealization of the experiment with the chalk sphere immersed in an infinite water domain, as shown in Figure 1.18 (a) and (b). The material properties were taken to be viscoelastic and represented by a generalized Maxwell model with one Maxwell unit. The density and the Poisson's ratio of the material were known and were taken as $1086\,kg/m^3$ and 0.26, respectively. Table 1.7 shows the search ranges used for the unknown parameters during the optimization process. The parameters to be identified were the long-term elastic Young's modulus, E, the dimensionless viscous Young's modulus, g, and the relaxation time, τ, for the chalk sphere.

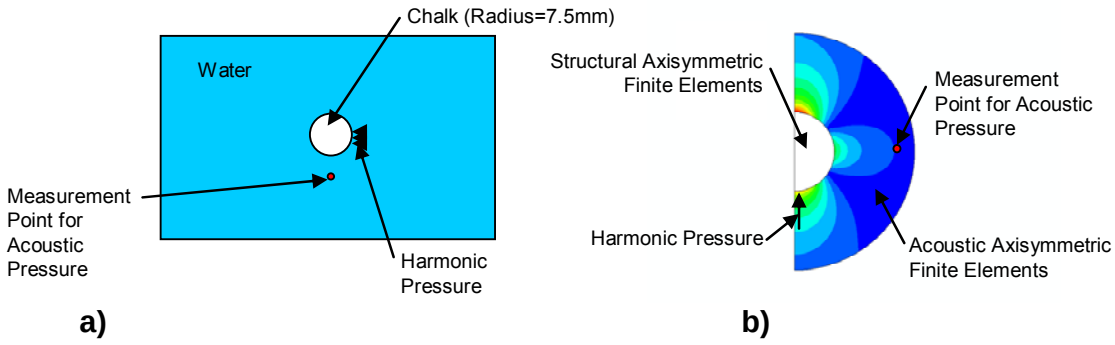

Figure 1.18. (a) Schematic and (b) finite element model for the vibroacoustic experiment (Example 4): chalk sphere in water.

Table 1.7. Optimization search ranges and results for the vibroacoustic experiment, Example 4: chalk sphere in water.

Parameter	Range	Optimization Results
E	$1.0\text{x}10^{9}$-$5\text{x}10^{9}$	$3.45\text{x}10^{9}$
g	0.05-0.95	0.090
τ	$1.0\text{x}10^{-7}$-$1.0\text{x}10^{-3}$	$4.48\text{x}10^{-6}$

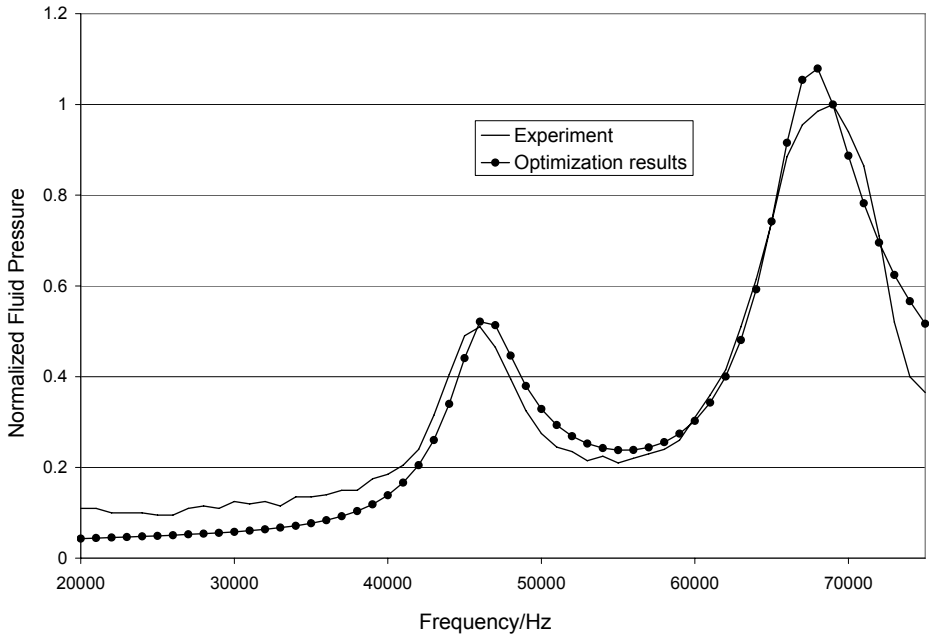

Figure 1.19. Frequency response of normalized acoustic pressure for the optimization results compared to the laboratory experiment for vibroacoustic experiment (Example 4): chalk sphere in water.

Figure 1.19 shows the acoustic pressure frequency response obtained from the inverse problem solution compared to the experimental data. Table 1.7 shows the material parameters estimated by the SMARS algorithm. In Mitri [28], the elastic modulus was reported to be 3.5 GPa. Figure 1.20 shows the equivalent elastic modulus found through the optimization trial compared to the elastic modulus reported in Mitri [28]. It is important to realize that in the approach shown in Mitri [28], the

elastic modulus was considered constant and a bulk viscosity was used to incorporate damping.

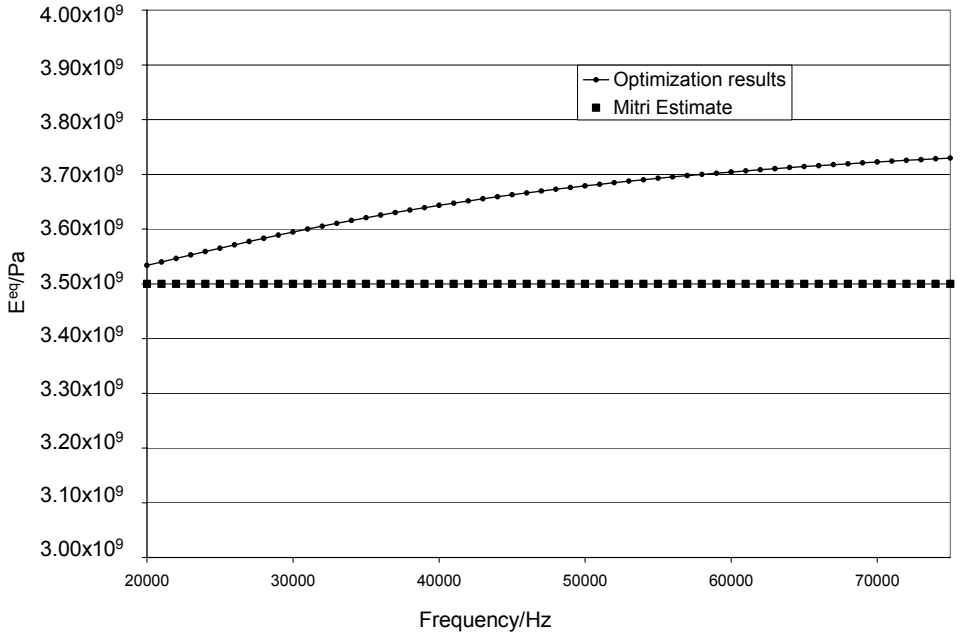

Figure 1.20. Frequency distribution of the equivalient elastic modulus (E^{eq}), for the optimization results for vibroacoustic experiment (Example 4): chalk sphere in water, compared to the elastic modulus results reported in [28].

It is clear from Figure 1.19 that an excellent fit was obtained for the frequency response of the finite element model compared to the experimental frequency response of the chalk sphere. The results are further validated by the strong similarity of the equivalent elastic modulus found through the viscoelastic model, compared to the elastic modulus as reported in Mitri [28].

1.6 Additional Comments

As with all inverse problems, particularly those involving non-invasive testing, the governing limitation to the inverse identification accuracy of the problem is not always the optimization method used, but the information present in the original

experiment. For the vibroacoustic case, the location and number of measurement points, measurement accuracy, and even modeling capabilities are limited by the nature of the experiments. In many vibroacoustic applications, it is likely the structure geometry and the configuration and location of the applied load will be known only to a moderate degree. The authors found, through various numerical simulations that small changes in the fluid measurement location and different loading configurations did not have a significant effect on the model responses, provided the same vibration modes were activated.

On the other hand, errors in the model geometry, such as the inclusion radius, showed a significant effect on the model response. Therefore, the proposed methodology requires that the geometry of the object be confidently known. However, the methodology can be used to search for both geometrical and mechanical properties provided sufficient information is gathered from the acoustic fields during an experiment.

Through extensive numerical trials, Poisson's ratio was consistently shown to have a weak effect on the acoustic response in the experiments studied herein. This would indicate that, in practice, further analysis would be required to ensure excitation of steady-state modes which are strongly affected by Poisson's ratio. A possible solution would be to include additional measurement locations for the acoustic emissions during the experiments. Yet, adding measurement points which increase experimental information and reveal additional behaviors may not be possible in many real applications. However, this may not be a severe drawback since it is often possible to treat soft tissue as an incompressible material, which makes Poisson's ratio to be known. Alternatively, the weak sensitivity shown in the examples to some components of the viscoelastic models may only be improved by extending or altering the frequency range studied in an experiment, and adding additional measurement

points may be less effective.

In all case presented herein the properties of the fluid were assumed to be known. Furthermore, since the objective of this work was not to quantify the effect of varying fluid properties on the behavior of solids, no attempt was made to analyze the sensitivity of the vibroacoustic experiments to changes in the fluid properties. In the work by Nayfeh[29] and Declercq, Van den Abeele, Degrieck, and Leroy[13] the properties of fluids surrounding plates were found to have a significant effect on the dynamic behavior of the plates. Thus, similarly to the geometric uncertainties previously mentioned, the fluid properties could also be incorporated as unknowns in the optimization strategy given sufficient experimental information.

1.7 Conclusions

In this work, a methodology was presented for the inverse estimation of material properties of vibrating solids using acoustic emission. The steady-state acoustic pressure response in a fluid surrounding a harmonically excited solid was shown to provide sufficient information to determine both elastic and viscoelastic material properties for homogeneous and heterogeneous structures. These findings have important implications for non-destructive evaluation of materials, in particular the non-invasive characterization of biological materials through techniques typically reserved for medical imaging, such as vibro-acoustography.

A combination of the classical random search algorithm and a surrogate-model approach, referred to as the surrogate model accelerated random search (SMARS) algorithm was also presented. The SMARS algorithm was shown to be an efficient and robust method for solving the inverse problem at hand. Several simulated examples were shown in which the SMARS algorithm displayed tolerance to measurement noise, and resiliency to inverse problem ill-posedness. An additional

example was shown based on the experiment described in Mitri [28], which confirmed the optimization ability of the SMARS algorithm in real-life problems, and the applicability of acoustic emissions for determining viscoelastic parameters.

REFERENCES

[1] R.A. Albanese, H.T. Banks, and J.K. Raye, Nondestructive evaluation of materials using pulsed microwave interrogating signals and acoustic wave induced reflections, Inverse Problems 18 (2002) 1935-1958.

[2] W. Aquino and J.C. Brigham, Self-learning finite elements for inverse estimation of thermal constitutive models, International Journal of Heat and Mass Transfer 49 (2006) pp 2466-2478.

[3] C. Aristegui and S. Baste, Optimal recovery of the elasticity tensor of general anisotropic materials from ultrasonic velocity data, Journal of the Acoustical Society of America 101 (1997) 813-833.

[4] F. Asma and A. Bouazzouni, Finite element model updating using FRF measurements, Shock and Vibration 12 (2005) 377-388.

[5] B. Audoin, Non-destructive evaluation of composite materials with ultrasonic waves generated and detected by lasers, Ultrasonics 40 (2002) 735-740.

[6] A. Bagchi, Updating the mathematical model of a structure using vibration data, Journal of Vibration and Control 11 (2005) 1469-1486.

[7] R.A. Baldewsing, C.L. De Korte, J.A. Schaar, F. Mastik, and A.F.W. Van Der Steen, A finite element model for performing intravascular ultrasound elastography of human atherosclerotic coronary arteries, Ultrasound in Medicine and Biology 30 (2004) 803-813.

[8] J. Baust, A.A. Gage, H.W. Ma, and C.M. Zhang, Minimally invasive cryosurgery - Technological advances, Cryobiology 34 (1997) 373-384.

[9] S.H. Brooks, A Discussion of Random Methods for Seeking Maxima, Operations Research 6 (1958) 244-251.

[10] S. Catheline, J.L. Gennisson, G. Delon, M. Fink, R. Sinkus, S.

Abouelkaram, and J. Culioli, Measurement of viscoelastic properties of homogeneous soft solid using transient elastography: An inverse problem approach, Journal of the Acoustical Society of America 116 (2004) 3734-3741.
[11] S.G. Chen, M. Fatemi, and J.F. Greenleaf, Remote measurement of material properties from radiation force induced vibration of an embedded sphere, Journal of the Acoustical Society of America 112 (2002) 884-889.
[12] R.D. Cook, D.S. Malkus, M.E. Plesha, and R.J. Witt, Concepts and Applications of Finite Element Analysis. Fourth ed, John Wiley & Sons, New York, NY, 2002.
[13] N.F. Declercq, F. Van den Abeele, J. Degrieck, and O. Leroy, The Schoch effect to distinguish between different liquids in closed containers, Ieee Transactions on Ultrasonics Ferroelectrics and Frequency Control 51 (2004) 1354-1357.
[14] F.A. Duck, Physical properties of tissue: a comprehensive reference book, Academic Press, London; San Diego, Calif., 1990.
[15] M. Fatemi and J.F. Greenleaf, Ultrasound-stimulated vibro-acoustic spectrography, Science 280 (1998) 82-85.
[16] M. Fatemi and J.F. Greenleaf, Vibro-acoustography: An imaging modality based on ultrasound-stimulated acoustic emission, Proceedings of the National Academy of Sciences of the United States of America 96 (1999) 6603-6608.
[17] M. Fatemi, A. Manduca, and J.F. Greenleaf, Imaging elastic properties of biological tissues by low-frequency harmonic vibration, Proceedings of the Ieee 91 (2003) 1503-1519.
[18] W.N. Findley, J.S. Lai, and K. Onaran, Creep and relaxation of nonlinear viscoelastic materials, with an introduction to linear viscoelasticity, North-Holland Pub. Co., Amsterdam, New York, 1976.

[19] Y.C. Fung, Biomechanics: mechanical properties of living tissues. 2nd ed, Springer-Verlag, New York, 1993.

[20] Y.C. Fung, K. Fronek, and P. Patitucci, Pseudoelasticity of Arteries and the Choice of Its Mathematical Expression, American Journal of Physiology 237 (1979) H620-H631.

[21] J.F. Greenleaf, M. Fatemi, and M. Insana, Selected methods for imaging elastic properties of biological tissues, Annual Review of Biomedical Engineering 5 (2003) 57-78.

[22] D. Haemmerich, S. Tungjitkusolmun, S.T. Staelin, F.T. Lee, D.M. Mahvi, and J.G. Webster, Finite-element analysis of hepatic multiple probe radio-frequency ablation, Ieee Transactions on Biomedical Engineering 49 (2002) 836-842.

[23] L.E. Kinsley, A.R. Frey, A.B. Coppens, and J.V. Sanders, Fundamentals of Acoustics. Fourth ed, Wiley, 2000.

[24] S.F. Levinson, M. Shinagawa, and T. Sato, Sonoelastic Determination of Human Skeletal-Muscle Elasticity, Journal of Biomechanics 28 (1995) 1145-1154.

[25] N. Leymarie, C. Aristegui, B. Audoin, and S. Baste, Identification of complex stiffness tensor from waveform, reconstruction, Journal of the Acoustical Society of America 111 (2002) 1232-1244.

[26] Q.S. Li, D.K. Liu, A.Y.T. Leung, N. Zhang, C.M. Tam, and L.F. Yang, Modelling of structural response and optimization of structural control system using neural network and genetic algorithm, Structural Design of Tall Buildings 9 (2000) 279-293.

[27] S.F. Masri, A.W. Smyth, A.G. Chassiakos, M. Nakamura, and T.K. Caughey, Training neural networks by adaptive random search techniques,

Journal of Engineering Mechanics-Asce 125 (1999) 123-132.
[28] F.G. Mitri, Inverse determination of porosity from object's resonances, Journal of Applied Physics 96 (2004) 5866-5869.
[29] A.H. Nayfeh, Wave Propagation in Layered Anisotropic Media: With Applications to Composites, Elsevier, Amsterdam; New York, 1995.
[30] H. Ogi, K. Sato, T. Asada, and M. Hirao, Complete mode identification for resonance ultrasound spectroscopy, Journal of the Acoustical Society of America 112 (2002) 2553-2557.
[31] B. Pichler, R. Lackner, and H.A. Mang, Back analysis of model parameters in geotechnical engineering by means of soft computing, International Journal for Numerical Methods in Engineering 57 (2003) 1943-1978.
[32] E.R. Pounder, The physics of ice, Pergamon Press, Oxford, New York, 1965.
[33] R.D. Reed and R.J. Marks II, Neural smithing: supervised learning in feedforward artificial neural networks, The MIT Press, Cambridge, Mass., 1999.
[34] R.G. Regis and C.A. Shoemaker, Constrained global optimization of expensive black box functions using radial basis functions, Journal of Global Optimization 31 (2005) 153-171.
[35] L.L. Rogers, F.U. Dowla, and V.M. Johnson, Optimal Field-Scale Groundwater Remediation Using Neural Networks and the Genetic Algorithm, Environmental Science & Technology 29 (1995) 1145-1155.
[36] B. Rubinsky, Cryosurgery, Annual Review of Biomedical Engineering 2 (2000) 157-187.
[37] M.A. Sumbatyan, A Method of Global Random Search in Inverse

Problems with Application to the Problem of Recognizing the Shape of a Defect, Pmm Journal of Applied Mathematics and Mechanics 56 (1992) 779-781.

[38] M.W. Urban, R.R. Kinnick, and J.F. Greenleaf, Measuring the phase of vibration of spheres in a viscoelastic medium as an image contrast modality, Journal of the Acoustical Society of America 118 (2005) 3465-3472.

[39] S. Yan and B. Minsker, A dynamic meta-model approach to genetic algorithm solution of a risk-based groundwater remediation design model, Proceeding of the 2004 World Water and Environmental Resources Congress: Critical Transitions in Water and Environmental Resources Management, American Society of Mechanical Engineers, Salt Lake City, UT, United States, 2004, Vol. 3, 1962-1971.

CHAPTER 2

Surrogate-Model Accelerated Random Search Algorithm for Global Optimization with Applications to Inverse Material Identification

2.1 Abstract

An optimization algorithm is proposed which is applicable for the global optimization of computationally expensive functions with specific applications in material identification. The methodology, referred to as the Surrogate-Model Accelerated Random Search (SMARS) algorithm, is a non-gradient based iterative application of a random search algorithm and the surrogate-model method for optimization. The random search algorithm drives the global search portion of SMARS, thoroughly probing the search space to find optimal regions. The surrogate-model method then applies an artificial neural network to map local regions of the search space, and produce computationally inexpensive estimates to the solution, thereby accelerating the search. Through simulated examples, the SMARS algorithm is shown to be both robust and efficient. First, the minimization of a well known function with multiple local minima was considered to demonstrate the SMARS optimization capabilities with a known complex response surface. Then, two examples were considered for the inverse characterization of material properties. The identification of parameters of a rheological viscoelasticity model was considered first, and shows the SMARS algorithm's tolerance to non-uniqueness over a large search space. Lastly, the identification of the distribution of thermal diffusivity for a functionally graded material was considered, and displays the SMARS capabilities to solve high dimensional inverse problems. In all three examples, the performances of two traditional global search algorithms, a genetic algorithm and a random search algorithm, were compared to that of the SMARS algorithm. In all cases, the SMARS

algorithm outperformed both traditional algorithms by attaining more accurate solutions with fewer function evaluations.

2.2 Introduction

Non-destructive methods for material identification have become of strong interest in all fields of engineering. Structures, from biological to industrial, can be evaluated and characterized by their material properties, whether mechanical, electrical, or thermal. Several examples include the work by Albanese et al. [1], Audoin [5], Ogi et al. [22], Aristegui et al. [4], and Aquino and Brigham [3]. By accurately determining material properties of existing structures, without disturbing the current state or behavior, it is possible to predict future responses to various stimuli.

Unfortunately, it is often not possible to find analytical solutions for such inverse problems as obtaining closed-form solutions is realistic only for simple geometries and boundary conditions. Thus, numerical representations of the system (e.g. finite element method (FEM) or boundary element method (BEM)), and nonlinear optimization methods are often necessary to find solutions for these inverse problems [3, 20]. The numerical modeling of complex systems is a formidable task alone, often requiring a large amount of computational time and power. In addition, material properties can vary drastically throughout a structure. As an example, in the case of biological structures, properties of these complex structures depend on the location in the body, age, and presence of disease [6, 10, 15, 16]. Thus, optimization methodologies applied to these problems must be able to search vast ranges of material parameters with the fewest number of numerical analyses possible. Furthermore, optimization problems of this nature tend to have non-convex error surfaces with multiple local solutions, and require the use of non-gradient based methods to locate a global solution.

Many algorithms, such as genetic algorithms [14, 19] and random search techniques [8, 18], have been developed and applied to global optimization problems. Unfortunately, most global search techniques require a large number of function evaluations, and also require significant user-interaction to converge to a global solution. Alternatively, surrogate-model methods have been applied specifically to optimization problems with computationally expensive numerical methods to limit the number of function evaluations required [17, 23, 25, 26, 28-30]. Yet, in many cases the surrogate-model methods can only be expected to converge to a local solution.

In this work, an optimization framework is proposed to combine a stochastic global search technique with a surrogate-model method to form a computationally efficient global optimization algorithm. The algorithm presented is a combination of a classical random search (RS) technique with an artificial neural network (NN) surrogate-model approach forming the Surrogate-Model Accelerated Random Search (SMARS) algorithm. In the SMARS algorithm, the stochastic search and the surrogate-model methods are combined in an iterative manner in which the surrogate-model is applied with an evolving localized search domain based on the stochastic search results. Thus, the method relies solely on the stochastic search to maintain global search capabilities, while relying on the surrogate-model method to accelerate convergence to a global solution.

2.3 Surrogate-Model Accelerated Random Search (SMARS) Algorithm

The basis of the SMARS algorithm is to combine the RS and surrogate-model methods to maintain the strengths of each algorithm while offsetting the weaknesses, and most importantly, minimize the number of function evaluations required to attain a solution. The RS portion of the algorithm is designed to probe the entire search space quickly and efficiently to determine globally optimal regions. Unfortunately,

maintaining the global search capabilities of the RS throughout the optimization process forces the RS to have a slow rate of convergence. Therefore, the surrogate-model approach is applied to rapidly estimate solutions within the locally optimal regions found through the RS. By relying on the random search portion of the algorithm for global search space probing, and applying the surrogate-model only to local regions, the algorithm maintains efficiency at both the global and local search levels, converging quickly to global solutions with a limited number of function evaluations.

2.3.1 Random Search

The RS algorithm, as outlined by Brooks [8], was used as one of the major foundations for this work. The most general form of the RS method consists of probing the solution space by randomly generating sets of parameters and computing the corresponding response error for each set. Next, new sets of parameters are randomly generated and evaluated in a neighborhood of the current best parameter set. The process is repeated until a given error measure decreases below a predefined tolerance or a maximum number of trials is reached. The trial parameter sets are selected based on some probability distribution (e.g. normal distribution) centered about the current best parameter set. Validity was given to the random method in Masri et al. [18], where the RS algorithm was shown to exhibit global convergence in a probabilistic sense.

In addition to the global convergence capabilities, the RS algorithm is not strongly affected by the size of the search space or the selection of initial parameter estimates. The downfall of the RS method is that many function evaluations are often required for the algorithm to converge to a global solution. In cases where computationally expensive numerical models (e.g. finite elements, boundary elements, etc.) are used,

the RS method may become unfeasible. In recent applications of the RS method, heuristic techniques have been developed in an attempt to increase the speed of convergence while maintaining the global search capabilities [18, 27]. Often, these heuristics involve methods to optimally choose the domain in which random parameter sets are generated (e.g. adjusting the standard deviation of normal distributions) throughout the optimization process. Unfortunately, the effectiveness of these heuristics may be strongly problem dependent and require significant user interaction. Therefore, these heuristics may limit the general applicability of the algorithms, and in many cases should be avoided.

2.3.2 Surrogate-Model Method for Optimization

Typically, in a surrogate-model approach, nonlinear mapping tools, such as radial basis functions, artificial neural networks, and support vector machines are used to approximate the response of a computationally expensive numerical model (e.g. a finite element model) [25, 29]. Select analyses are performed with the computationally expensive model to create a data set of optimization parameters and corresponding model responses. This data set is then used to train the surrogate-model to receive model optimization parameters as input and produce an approximation to the response of the numerical model as output. An approximation to the solution is then obtained with the surrogate-model used in place of the expensive numerical model in some chosen optimization algorithm.

The surrogate-model method has been shown to provide accurate approximations to complex problems with very few function evaluations [17, 23, 25, 26, 28-30]. Unfortunately, given a non-descriptive data set, no mapping tool will sufficiently represent the response surface to obtain an accurate optimization estimate. Therefore, the most difficult aspect of the surrogate-model method is the development of a

comprehensive data set for surrogate-model training. Furthermore, the surrogate-model can only provide estimates within the bounds of the given data set, and therefore can only be expected to perform as a local optimization technique in general.

2.3.3 Description of the SMARS Algorithm

In order to describe the SMARS algorithm, it is convenient to define the following functions and sets:

$\vec{f}^{R}\left(\vec{\alpha},\vec{\beta}\right)$, response function computed using a complex numerical model (e.g. FEM, BEM, etc.).

$\vec{f}^{\exp}\left(\vec{\beta}\right)$, experimentally measured response function.

$\vec{f}^{sm}\left(\vec{\alpha},\vec{\beta}\right)$, response function computed using the surrogate-model.

$\vec{\alpha}\in\mathbb{R}^{n}$, vector of n unknown/design parameters (e.g. material constants).

$\vec{\beta}\in B$, vector of state variables within the domain of the experiment, B (e.g. time/frequency over some range, position within a given body, etc.).

$M^{n}\left(\vec{a},\vec{b}\right)=\left\{\vec{\alpha}:a_i\le\alpha_i\le b_i, i=1,2,\ldots,n\right\}$, the n-cell in $\mathbb{R}^{n}$ used to bound initial parameter guess distributions and to construct the surrogate-model training set.

$\left[a_i,b_i\right]$ is the interval of admissible values for the i^{th} unknown parameter.

All functions under consideration are taken to belong to the Hilbert space $L_2\left(B\right)$, which is defined as $L_2\left(B\right)=\left\{f:\int_B\left[f\left(\vec{\beta}\right)\right]^2 d\vec{\beta}<\infty\right\}$, and which is endowed with the norm

$$\left\|f\right\|_{L_2(B)}=\left(\int_B\left[f\left(\vec{\beta}\right)\right]^2 d\vec{\beta}\right)^{\frac{1}{2}}. \tag{1}$$

Two response error measures are defined: γ^{R} and γ^{sm}. The model error, γ^{R}, quantifies the distance between the response computed using the numerical model and

the experimentally measured response of the system. This error functional is defined as

$$\gamma^R(\vec{\alpha}) = \sum_{i=1}^{m} \left\| f_i^R(\vec{\alpha}, \vec{\beta}) - f_i^{\exp}(\vec{\beta}) \right\|_{L_2(B)}, \tag{2}$$

where m is the number of response components (e.g. multiple sensor locations, directional components of the response, etc.). The surrogate-model error, γ^{sm}, quantifies the distance between the response computed using a surrogate-model and the experimentally measured response of the system. This error functional is defined as

$$\gamma^{sm}(\vec{\alpha}) = \sum_{i=1}^{m} \left\| f_i^{sm}(\vec{\alpha}, \vec{\beta}) - f_i^{\exp}(\vec{\beta}) \right\|_{L_2(B)}. \tag{3}$$

The unconstrained optimization problem can then be shown as

$$\underset{\vec{\alpha} \in \mathbb{R}^n}{Minimize} \left(\gamma^R(\vec{\alpha}) \right). \tag{4}$$

The SMARS algorithm to solve the above optimization problem can be laid out as follows (See Figure 2.1 for a flowchart of the SMARS algorithm).

- Set ε. // Specify the tolerance for the model error.//
- Set $maxIter$. // Specify maximum number of algorithm iterations.//
- Set $\vec{a}$ and $\vec{b}$. // Estimate initial search limits for each of the n variables.//
- Generate $\vec{\alpha}^k \in M^n(\vec{a}, \vec{b}),$ for k = $1, 2, \ldots, j$. // Randomly generate a set of j uniformly distributed trial solution vectors over the initial search domain.//
- Compute $\left\{ \gamma^R(\vec{\alpha}^1), \gamma^R(\vec{\alpha}^2), \ldots, \gamma^R(\vec{\alpha}^j) \right\}$. // Evaluate each trial solution through the numerical model of the system and calculate the model error.//
- Find $\vec{\alpha}^*$ corresponding to $\gamma^R(\vec{\alpha}^*) = \min\left\{ \gamma^R(\vec{\alpha}^1), \ldots, \gamma^R(\vec{\alpha}^j) \right\}$. // Identify current best solution approximation from population of evaluated trial solutions.//
- While $\left(\gamma^R(\vec{\alpha}^*) > \varepsilon \text{ and } iterations < maxIter \right)$

- Update $\vec{a}$ and $\vec{b}$. // Select bounds for the subset of the current set of trial solutions which will be used to train the surrogate-model (see Section 2.3.3.2).//
- Train the surrogate-model to create the mapping $f^{sm}:\left(M^n\left(\vec{a},\vec{b}\right)\times B\right)\rightarrow D$. // $D=\left\{\vec{f}^{\,R}\left(\vec{\alpha},\vec{\beta}\right):\vec{\alpha}\in M^n\left(\vec{a},\vec{b}\right),\vec{\beta}\in B\right\}$ is the set of responses computed from the numerical model of the system (see Section 2.3.3.2).//
- Find $\vec{\alpha}^{sm}$ (solution estimate using the surrogate-model) by solving $\underset{\vec{\alpha}\in M^n}{Minimize}\left(\gamma^{sm}\left(\vec{\alpha}\right)\right)$. // (See Section 2.3.3.2).//
- Set $\vec{\alpha}^{j+1}=\vec{\alpha}^{sm}$ and compute $\gamma^R\left(\vec{\alpha}^{j+1}\right)$. // Add $\vec{\alpha}^{sm}$ to the set of trial solutions and evaluate the model error.//
- If $\gamma^R\left(\vec{\alpha}^{j+1}\right)<\varepsilon$ exit while loop.
- Select $\vec{\xi}^{\,i}\in\left\{\vec{\alpha}^1,\vec{\alpha}^2,\ldots,\vec{\alpha}^{j+1}\right\}$, for i = $1,2,\ldots,p$. // Select p parameter vectors from the current set of trial solutions for generating new trial solutions (see Section 2.3.3.1).//
- Generate $\left\{\vec{\alpha}^1,\vec{\alpha}^2\ldots,\vec{\alpha}^q\right\}_i$ and compute $\left\{\gamma^R\left(\vec{\alpha}^1\right),\gamma^R\left(\vec{\alpha}^2\right),\ldots,\gamma^R\left(\vec{\alpha}^q\right)\right\}_i$, for i = $1,2,\ldots,p$, and add to the set of trial solutions // Randomly generate and evaluate q new trial solutions around each $\vec{\xi}^{\,i}$ (see Section 2.3.3.1).//
- Set $j=j+1+pq$. // The set of trial solutions contains all randomly generated trial solutions and the surrogate-model estimated trial solution.//
- Find $\vec{\alpha}^*$ corresponding to $\gamma^R\left(\vec{\alpha}^*\right)=\min\left\{\gamma^R\left(\vec{\alpha}^1\right),\ldots,\gamma^R\left(\vec{\alpha}^j\right)\right\}$.

- End while

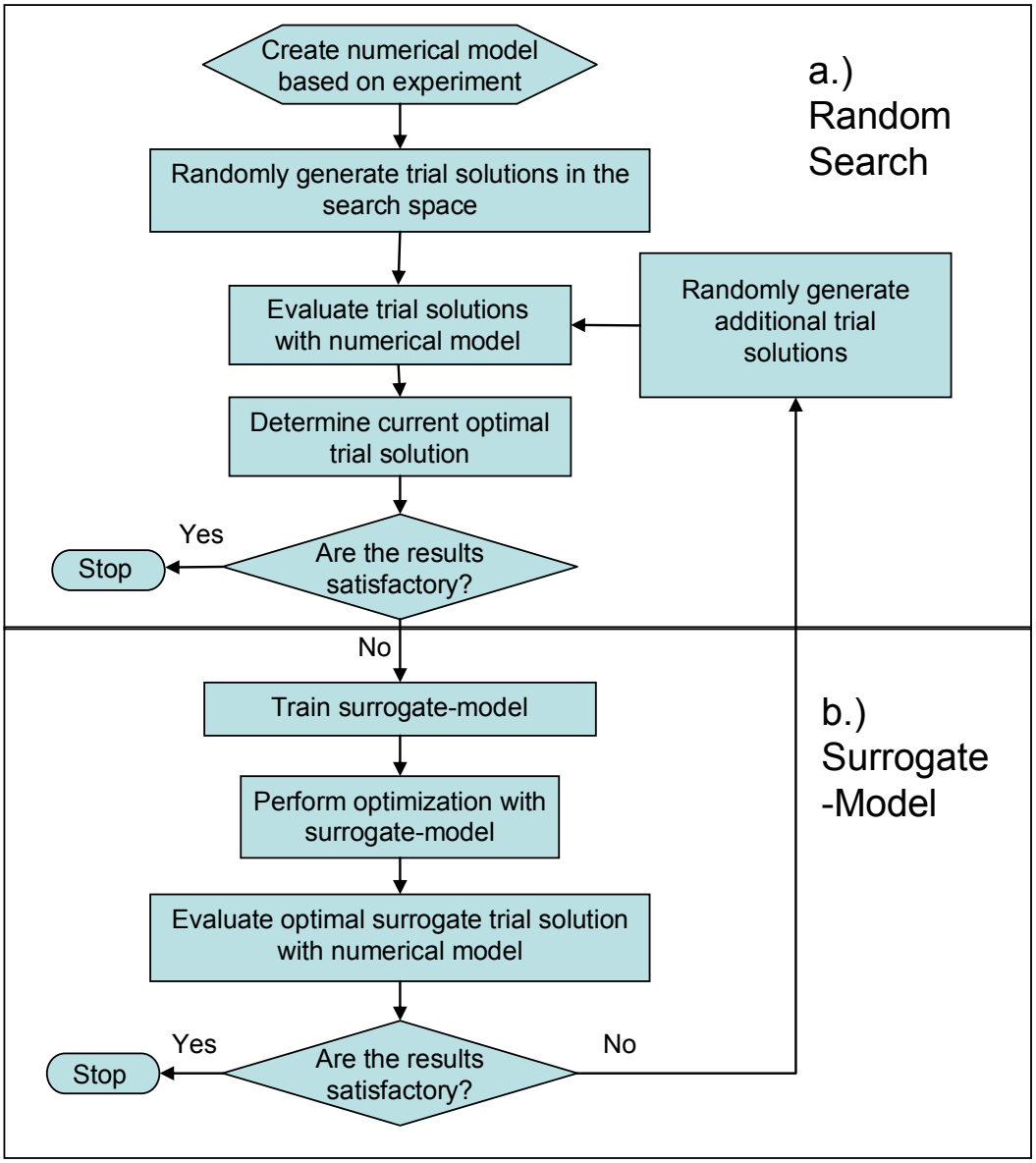

Figure 2.1. Flowchart of the Surrogate-Model Accelerated Random Search (SMARS) algorithm with a.) the random search technique and b.) the surrogate-model technique.

2.3.3.1 Generating Trial Solutions

Another desirable feature of the RS portion of the SMARS algorithm is that in addition to quickly and efficiently identifying globally optimal regions, once identified the RS portion of the SMARS algorithm was designed to increase the number of trial solutions evaluated in this optimal region. By increasing the density of trial solutions

evaluated in the globally optimal region, the surrogate-model is able to more accurately represent this region and produce improved estimates to the solution.

It was found that in order to efficiently search globally, it is important to maintain diversity in the regions being probed by the RS during early iterations of the algorithm. Therefore, for the applications shown here, two trial solutions (i.e. $p = 2$) were chosen from the current set to be centers for the generation of the new trial solutions.

The two trial solutions chosen, $\vec{\xi}^1$ and $\vec{\xi}^2$, are called search poles and were defined as follows:

$\vec{\xi}^1 = \vec{\alpha}^*$.

$\vec{\xi}^2$ is found by first ranking the current population of trial solutions using the model error, γ^R, from lowest to highest. Then, $\vec{\xi}^2$ corresponds to $\left\|\vec{\xi}^2 - \vec{\alpha}^*\right\|_{l^2} = \max\left\{\left\|\vec{\alpha}^1 - \vec{\alpha}^*\right\|_{l^2}, \ldots, \left\|\vec{\alpha}^n - \vec{\alpha}^*\right\|_{l^2}\right\}$, where $\left\{\vec{\alpha}^1, \vec{\alpha}^2, \ldots, \vec{\alpha}^n\right\}$ are the trial solutions in the top 20% of the ranked population. In the above expression, the discrete l^2-norm of the vectors was used, and is given by

$$\left\|\vec{\alpha}\right\|_{l^2} = \left(\sum_{i=1}^{n} (\alpha_i)^2\right)^{\frac{1}{2}}. \tag{5}$$

The search poles $\vec{\xi}^1$ and $\vec{\xi}^2$ can be described, respectively, as the trial solution with lowest model error, γ^R, from the current set, and the trial solution which is farthest, according to the l^2-norm, from $\vec{\xi}^1$, but is still within the best 20% of the current set. By choosing the search poles in this manner, diversity can be expected in the search space probed by the RS during early iterations. Then, as the algorithm continues and a globally optimal region in the search space is identified, the search poles, $\vec{\xi}^1$ and $\vec{\xi}^2$, would be expected to become progressively closer to each other. Therefore, the number of trial solutions evaluated in close proximity to the current optimal trial solution will gradually increase as the iterations increase.

For the applications presented, the new trial solutions were generated using normal distributions centered on the search poles. That is, for each pole, a set $\left\{\vec{\alpha}^1, \vec{\alpha}^2, \ldots \vec{\alpha}^q\right\}$ was randomly generated and each component of these parameter vectors was computed as $\alpha_i^v = N\left(\xi_i^k, d_i^\kappa\right)$. α_i^v is the i[th] component of the parameter vector $\vec{\alpha}^v$ and $N\left(\xi_i^k, d_i^k\right)$ denotes a normally distributed random variable with mean ξ_i^k and standard deviation d_i^k.

In the SMARS algorithm, the surrogate-model replaces the need to use heuristics to continuously adjust the domain of the random trial generation to accelerate convergence. As such, for this work, the standard deviation of the normally distributed random parameters was set to be a fixed percentage of the search pole parameter values. This percentage was chosen based on the size of the parameter search space. A value around 100% would be sufficient for a search range which covers several orders of magnitude, whereas a value around 10% would be sufficient for a search range which is less than one order of magnitude. Using a percentage of the search pole parameter values along with the search poles defined above was found to be suitable for maintaining global search capabilities of the random search, while allowing the surrogate-model to receive enough information about optimal regions to accelerate the search towards a global solution.

2.3.3.2 Development of Surrogate-Model

In this work, the surrogate-model was chosen to be represented by a fully connected feed- forward neural network (NN). NNs were chosen because of their universal function approximation capabilities. In addition, NNs can be trained to map a data set quickly through various methods, and once trained, NNs produce interpolated results in fractions of a second. As is typical for NNs of the type used here, a gradient based approach known as resilient propagation was applied to train the

NN to learn the model behavior. See [24] for a complete description of NNs and NN training approaches.

In order to train a NN, it is first necessary to create a data set, or training set, of inputs and corresponding outputs which is representative of the desired system behavior. In this work, the SMARS algorithm relies on the trial solutions which are selected and evaluated throughout the RS portion of the algorithm to create the training set for the NN. Unfortunately, it is often not possible to know *a priori* whether a given training set is representative of the true behavior of a system. Furthermore, the nature of the trial solution generation through the RS will lead to a biased distribution of trial solutions, which can severely affect the generalization capabilities of NNs. In other words, if a NN was applied to map the entire parameter space probed by the RS, it would be expected that the NN would produce poor predictions in many regions of the search space. Alternatively, this potential difficulty can be prevented by limiting the region being mapped by the NN to be a smaller window of the search space around the current optimal trial solution. For example, in this work, the search window was defined by $M^n\left(\vec{a},\vec{b}\right)$, and the bounds of the window, $\vec{a}$ and $\vec{b}$, were chosen as scalar multiples of $\vec{\alpha}^*$. Therefore, only the evaluated trial solutions produced by the RS which lie within the search window will be used to train the NN. Since a large portion of the trial solutions produced by the RS will be generated around the current optimal, the NN will receive a higher concentration of training information within this region. Thus, the NN should provide more consistent predictions of the solution throughout the optimization process.

Once trained, the surrogate-model is used to obtain an estimate of the solution by solving an additional minimization problem, as stated in the description of the SMARS algorithm. For this work, a genetic algorithm (GA) was used in the surrogate-model minimization problem. GAs provide excellent global search

capabilities, but require large numbers of function evaluations to obtain solutions. However, since the NN surrogate-model provides computationally inexpensive function evaluations, the use of a GA is feasible. It is important to bear in mind that any other global optimization method (e.g. simulated annealing, direct search, etc.) can be used to obtain the surrogate-model estimate to the solution within the SMARS algorithm.

2.4 Examples

To explore the robustness and effectiveness of the SMARS algorithm, three example problems were considered: minimization of a non-convex mathematical function, inverse identification of viscoelastic material properties using vibroacoustic techniques, and inverse characterization of a functionally graded diffusivity using discrete temperature measurements. All three examples can be shown to have highly non-convex response surfaces over the search ranges considered and, therefore, would present considerable difficulty to gradient-based methods of optimization. To compare the performance of the SMARS algorithm to other solution methods, each example was also solved with a GA and a pure RS algorithm. Due to the stochastic nature of the algorithms investigated in this work, each case was evaluated ten times, and the mean and standard deviation of the results were examined.

For the first two examples, the maximum number of function evaluations was fixed to simulate computing limitations associated with computationally expensive function evaluations. In addition, to analyze the effect of the training set window for the surrogate-model method, the first two example problems were solved using three different training set approaches with the SMARS algorithm. First, two different window sizes were applied to the examples to show the sensitivity of the performance of the SMARS algorithm to the window size. Window 1 was defined by $\vec{a} = 0.5\vec{\alpha}^*$

and $\vec{b} = 1.5\vec{\alpha}^*$, and Window 2 was defined by $\vec{a} = \vec{0}$ and $\vec{b} = 2\vec{\alpha}^*$. Alternatively, it can be stated that Window 1 includes trial solutions with entries within $\pm 50\%$ of the current optimal trial solution, and Window 2 includes trial solutions with entries within $\pm 100\%$ of the current optimal trial solution. Lastly, the SMARS algorithm was applied without a training set window to show the general benefits of the windowing approach. Note that without a training set window, the surrogate-model is expected to map the entire search space probed by the RS.

For the final example, the maximum number of function evaluations was drastically increased and an error tolerance was set to provide a comparison of the number of function evaluations required by each algorithm to reach this given tolerance. The SMARS search window for the third example was defined by $\vec{a} = 0.1\vec{\alpha}^*$ and $\vec{b} = 1.1\vec{\alpha}^*$, or $\pm 10\%$ of the current optimal trial solution, due to the much smaller search range considered compared to the first two examples.

The pure RS algorithm applied to the three examples followed the same format as the RS described for the SMARS algorithm, including the use of two search poles for generating trial solutions. The only difference between the pure RS algorithm and the SMARS algorithm is that the surrogate-model portion of the algorithm is not used in the pure RS case. The GA used for the first two examples had single-point crossover and uniform mutation with a rate of 10%. The GA used for the third example had two-point crossover and uniform mutation with a rate of 10%. The general theory behind GA is out of the scope of this paper and can be found in [14, 19].

2.4.1 Rastrigin's Function

The minimization of the Rastrigin's function was considered first to display the benefits of the SMARS algorithm for a problem with a well known non-convex error surface with many local minima and one global minimum. The two-dimensional

Rastrigin's function was offset so that the global minimum was located at $(100, 9000)$. Notice that the function was offset so that the solution parameters were an order of magnitude apart, forcing the algorithms to search over multiple orders of magnitude, and effectively increasing the difficulty of the optimization problem.

The function to be minimized was given by

$$R(x,y) = 20 + (x\text{-}100)^2 + (y-9000)^2 - 10\left(\cos\left[2\pi(x-100)\right] + \cos\left[2\pi(y-9000)\right]\right). \quad (6)$$

The minimum value of $R(x,y)$ is 0, and x and y are the optimization parameters. Figure 2.2 shows a graphical representation of Equation (6). In the optimization problem, $\vec{\alpha} = \{x,\ y\}$ and $\gamma^R(\vec{\alpha}) = R(x,y)$, $x, y \in [0, \infty)$.

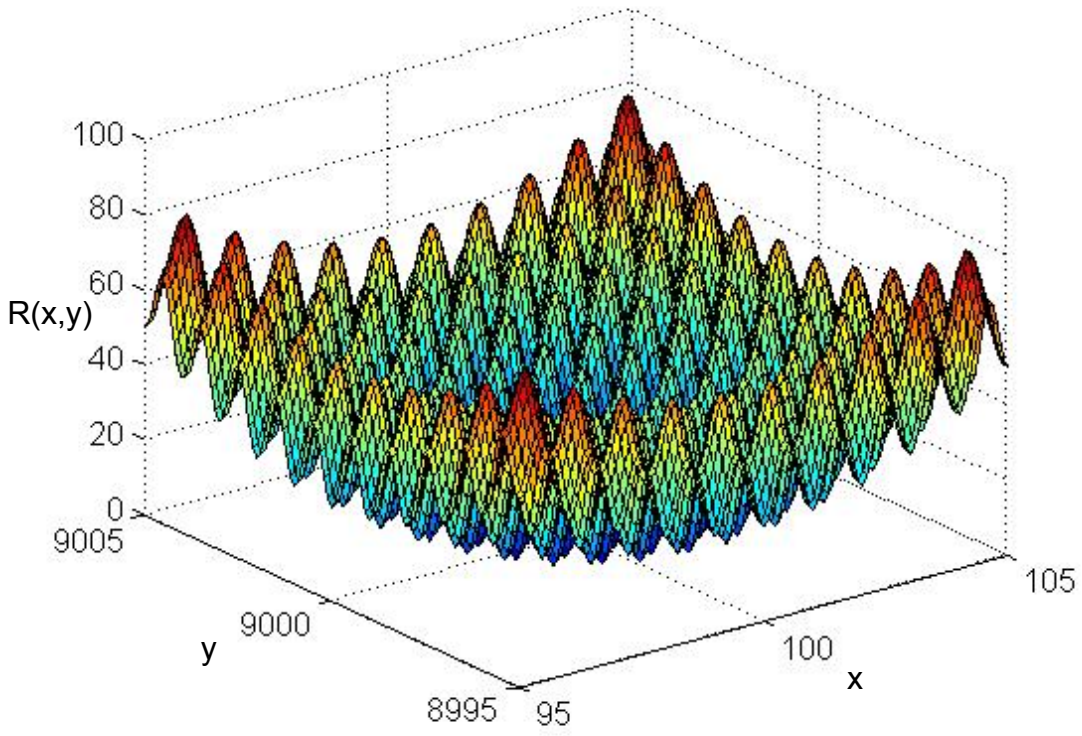

Figure 2.2. Graphical representation of Rastrigin's function.

For this example, a maximum of 300 function evaluations was used for the optimization algorithms. The GA had a population of 20 individuals (trial solutions) and was limited to 15 generations. The RS algorithm had an initial set of 80 trial

solutions, and five trial solutions were created randomly about each of the two search poles for 22 iteration. The SMARS algorithm had an initial set of 65 trial solutions, and five trial solutions were created randomly about each of the two search poles along with one trial solution generated by the surrogate-model method for 21 iterations. The standard deviation percentage was set to 100% for the SMARS and pure RS algorithms, to account for the size of the parameter ranges.

2.4.1.1 Results and Discussion

For this example, a solution error was defined to compare the optimization solutions, and was defined as

$$\gamma^{sol}\left(\vec{\alpha}^{*}\right)=\left\|\vec{\alpha}^{*}-\vec{\alpha}^{sol}\right\|_{l^{2}}, \tag{7}$$

where $\vec{\alpha}^{sol}=(100,9000)$ is the known solution for the problem. Figure 2.3 shows the average and standard deviation of the solution error for the 10 trials of each algorithm. In all cases, the GA performed poorly compared to the SMARS and the pure RS algorithms with the limited number of function evaluations. The results of the SMARS trials and the pure RS trials were further analyzed separately, and the average and standard deviation of the solution error for those trials is shown in Figure 2.4. Clearly the trials of the SMARS algorithm with training set windows outperformed the pure RS algorithm by displaying a lower average and standard deviation of the solution error, with the Window 1 case having slightly better results than the Window 2 case. Alternatively, the SMARS algorithm without a training set window had only a small improvement in the average solution error compared to the pure RS, but the standard deviation of the solution error was again much smaller for the SMARS algorithm.

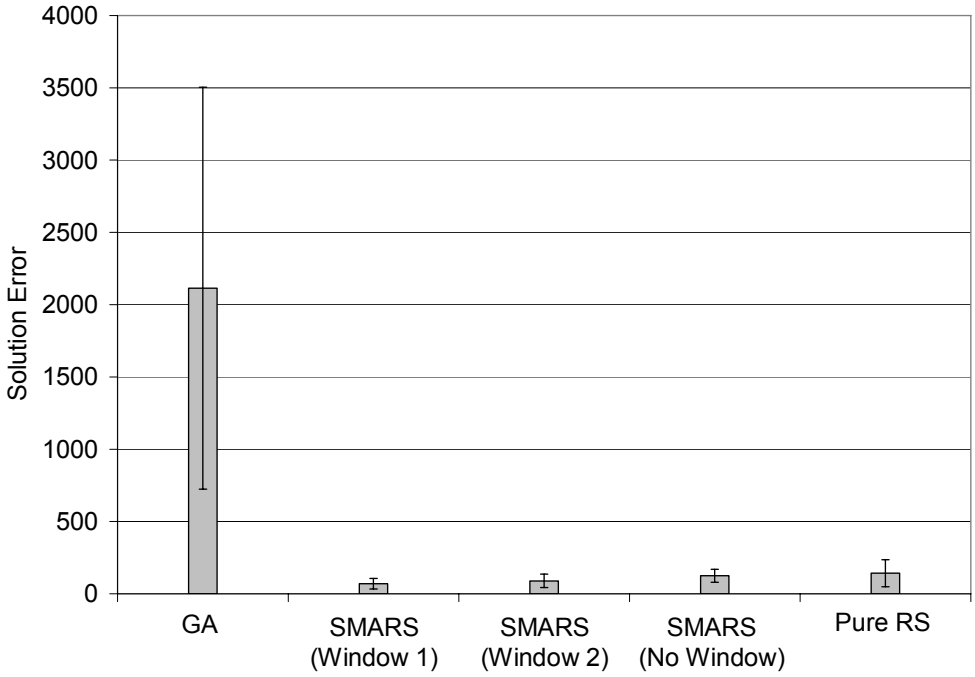

Figure 2.3. Average and standard deviation (error bars) of the solution error, γ^{sol}, for each algorithm for Example 1.

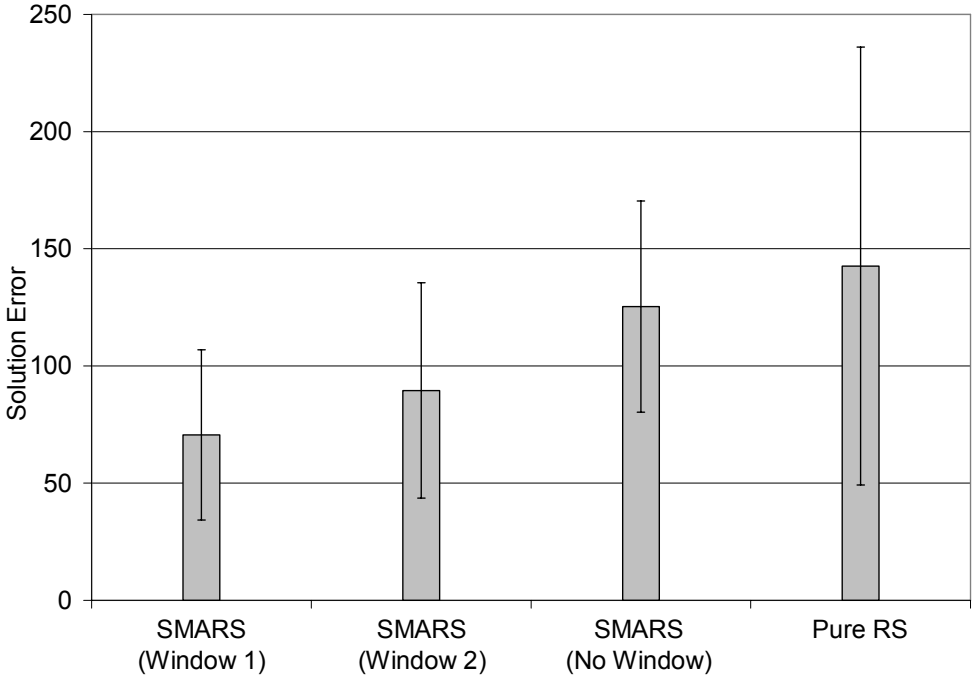

Figure 2.4. Average and standard deviation (error bars) of the solution error, γ^{sol}, for the SMARS and pure RS test cases for Example 1.

The results indicate that the use of the surrogate-model method in the SMARS algorithm leads to less variation in the solution, as compared to the pure RS. Furthermore, a progressive improvement can be seen in the SMARS algorithm as the window in the search space being mapped by the surrogate-model becomes smaller. Though, a less significant improvement was found when comparing the two cases with windows, indicating a relatively weak sensitivity of the results to the chosen window size.

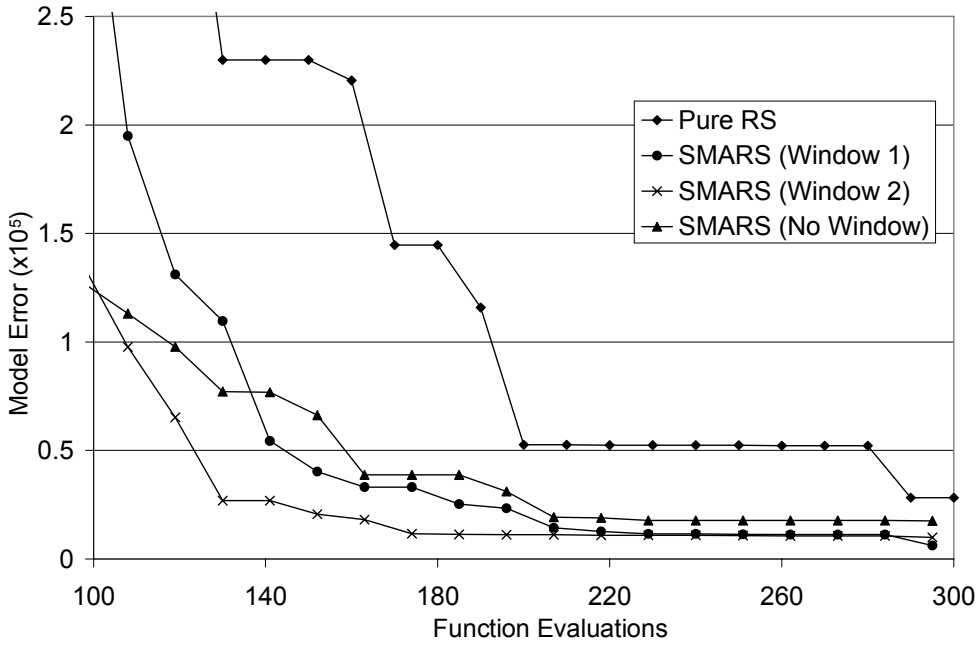

Figure 2.5. Average model error, γ^R, versus the number of function evaluations for the SMARS and pure RS test cases for Example 1.

To assess the performance of the SMARS and pure RS algorithms throughout the iterative optimization process, the average model error for the current optimal trial solution, $\gamma^R\left(\vec{\alpha}^*\right)$, at each iteration versus the number of function evaluations for these cases is shown in Figure 2.5. The results show that the model errors of all three SMARS test cases, particularly in the cases with training set windows, decreased at a

smoother and faster rate than the pure RS trials. Moreover, Figure 2.5 shows that the average model error for the SMARS cases reached a value at 180 function evaluations comparable to that of the pure RS case at 300 function evaluations, which represents about a 40% reduction in computational cost in terms of the solution estimates.

Lastly, the effect of the training set windows on the surrogate-model performance was examined. Figure 2.6 shows the average and standard deviation of the model error for the current optimal trial solution, $\gamma^R\left(\vec{\alpha}^*\right)$, compared to the model error of the surrogate-model estimates, $\gamma^R\left(\vec{\alpha}^{sm}\right)$, at each iteration versus the number of function evaluations for the three SMARS test cases. The results show that as the window size increases, the accuracy of the surrogate-model predictions decreases, and the surrogate-model is less effective in accelerating solution convergence. The SMARS trials without a training set window show a particularly large average and standard deviation of model error for the surrogate-model predictions. Clearly the complexity of the search space for this example and the biased distribution of the surrogate-model training set limited the ability of the surrogate-model to map large regions of the search space.

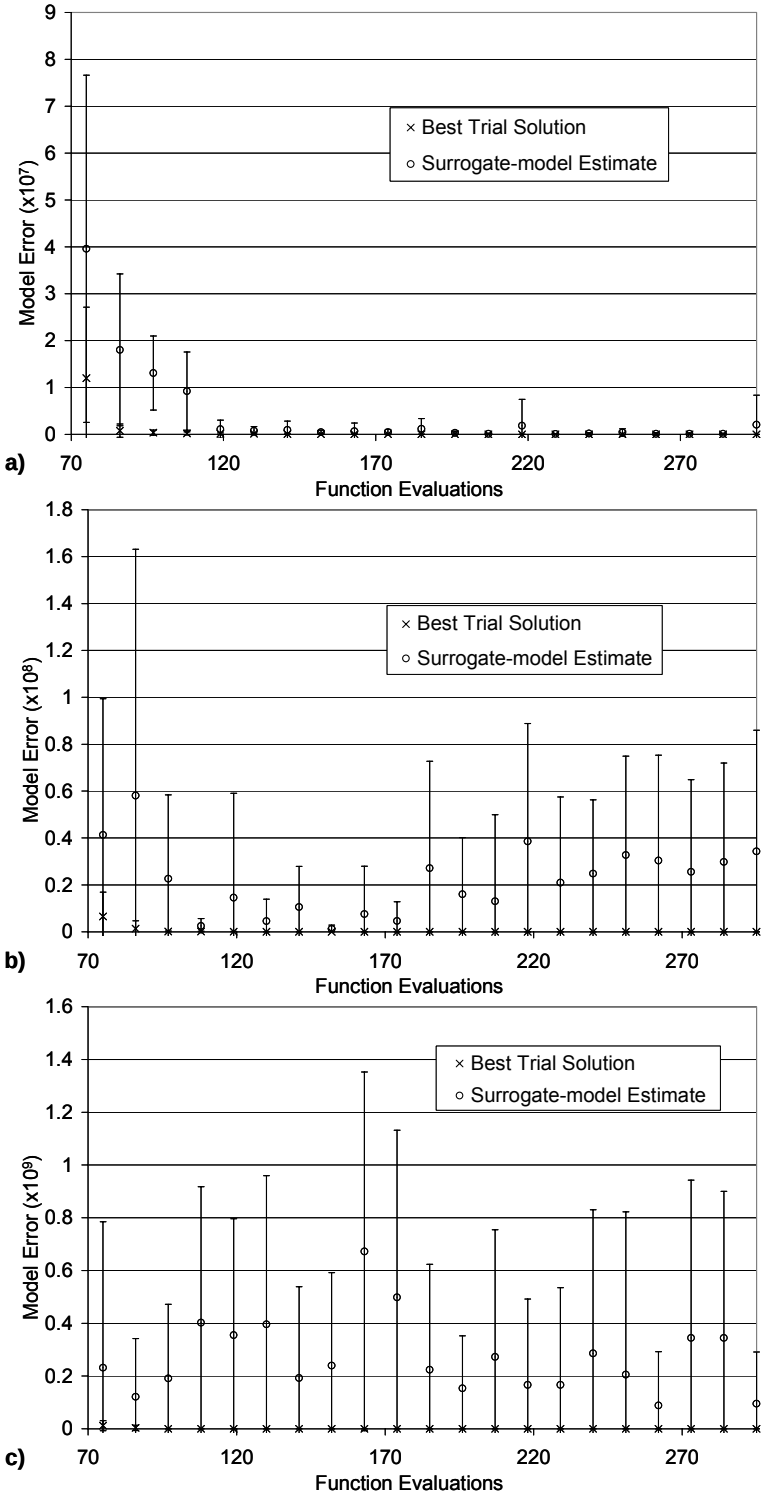

Figure 2.6. Average and standard deviation (error bars) of the model error, γ^R, of the best trial solutions and the model error of the surrogate-model estimates, versus the number of function evaluations for SMARS with (a) Window 1, (b) Window 2, and (c) no window for Example 1.

2.4.2 Inverse Material Identification Using Acoustic Emissions

Next, an example was considered to show the performance of the SMARS algorithm in a realistic engineering application in which the solution variables are known to be non-unique and can realistically have values covering several orders of magnitude. This example is based on the work by Brigham et. al. [7], in which the vibro-acoustography (VA) methodology [11, 12], which is currently used for medical imaging, was applied to provide quantitative viscoelastic material properties of solids immersed in fluids. The VA method is a non-invasive and non-destructive testing procedure in which ultrasound radiation is used to remotely produce an oscillating force on a structure, while a hydrophone measures the resulting acoustic pressure in the surrounding fluid caused by the vibrating solid. In the VA procedure considered here, the structure is excited harmonically to a steady-state condition at various excitation frequencies, and the amplitude of the acoustic emissions is measured at each frequency.

The inverse problem then becomes the identification of the viscoelastic properties of the structure based solely on the measured acoustic pressure amplitudes for a discrete set of frequencies. Thus, the model error for the optimization procedure for this problem was defined as

$$\gamma^R(\vec{\alpha}) = \left\| \vec{P}^R(\vec{\alpha}) - \vec{P}^{\exp} \right\|_{l^2}. \tag{8}$$

Where $\vec{\alpha}$ is the vector containing the unknown viscoelastic parameters and $\vec{P}^R(\vec{\alpha})$ and $\vec{P}^{\exp}$ are the vectors of computed and experimentally measured pressures, respectively, at a given fluid point for a set of excitation frequencies. A steady-state dynamic FEM was used as the numerical representation of the VA experiment (for a complete description of the FE fluid-structure interaction problem see [7]).

In this work, the frequency dependent stress-strain relationship in the solid was considered to be defined by an isotropic linear viscoelastic model based on the

relationship derived from a rheological model of n parallel sets of springs and dashpots in series (Maxwell elements), with an additional spring in parallel, and is referred to as the generalized Maxwell model (See [7, 13] for a more detailed formulation). The viscoelastic material was defined by a constant Poisson's ratio and a complex Young's modulus defined by a one-unit generalized Maxwell model in the frequency domain as

$$E^*(\omega) = E + \tilde{E}\left(\frac{\omega^2\tau^2 + i\omega\tau}{1+\omega^2\tau^2}\right). \tag{9}$$

Where E is the long-term elastic Young's modulus, $\tilde{E}$ is the viscous Young's modulus, and τ is the relaxation time. In the results presented, the viscous Young's modulus is expressed through the dimensionless viscous Young's modulus, g, given by

$$g = \frac{\tilde{E}}{E+\tilde{E}}. \tag{10}$$

An additional consideration for the characterization of viscoelastic materials is that different combinations of viscoelastic parameters (i.e. $E, \tilde{E}, \tau$), or even different viscoelastic rheological representations can result in the same material behavior over a given frequency range. This non-uniqueness not only causes difficulty in deriving physical meaning from the viscoelastic parameters, but also causes problems for any inverse characterization strategy. Alternatively, a viscoelastic material may be uniquely characterized by physically relevant quantities, such as energy storage and dissipation over the frequency range. Energy dissipation and storage can be expressed through the mechanical loss parameter, $\tan\left[\delta(\omega)\right]$, which is associated with viscous damping, and the equivalent elastic modulus, $E^{eq}(\omega)$, respectively. The mechanical loss and equivalent elastic modulus are defined as the ratio of the imaginary to the real portion of the complex modulus, and the magnitude of the complex modulus, respectively. For the complex Young's modulus considered here, these quantities are

given by

$$\tan(\delta) = \left[\tilde{E}\left(\frac{\omega\tau}{1+\omega^2\tau^2}\right)\right] \Big/ \left[E + \tilde{E}\left(\frac{\omega^2\tau^2}{1+\omega^2\tau^2}\right)\right], \tag{11}$$

and

$$E^{eq}(\omega) = \left\{\left[\tilde{E}\left(\frac{\omega\tau}{1+\omega^2\tau^2}\right)\right]^2 + \left[E + \tilde{E}\left(\frac{\omega^2\tau^2}{1+\omega^2\tau^2}\right)\right]^2\right\}^{1/2}. \tag{12}$$

Although the generalized Maxwell model parameters defining these characteristics may be non-unique, the characteristic functions themselves uniquely define the material behavior. Therefore, in the following examples the quality of the inversely obtained viscoelastic models is shown through comparisons of the viscoelastic characteristic functions, $\tan\left[\delta(\omega)\right]$ and $E^{eq}(\omega)$.

The experiment was numerically simulated, and consisted of a viscoelastic cylinder immersed in water with a harmonic pressure line applied to the surface of the cylinder as shown in Figure 2.7 (a). The experiment was simulated with a plane strain finite element model as shown in Figure 2.7 (b), which was thoroughly checked for mesh convergence, and the surrounding fluid was modeled as an infinite domain. Plane strain was selected for this example to decrease computation time. The density of the solid and the water were assumed to be known and were taken as $1050\,kg/m^3$ and $1000\,kg/m^3$, respectively. The bulk modulus of the water was also assumed known and taken to be $2.2\ GPa$.

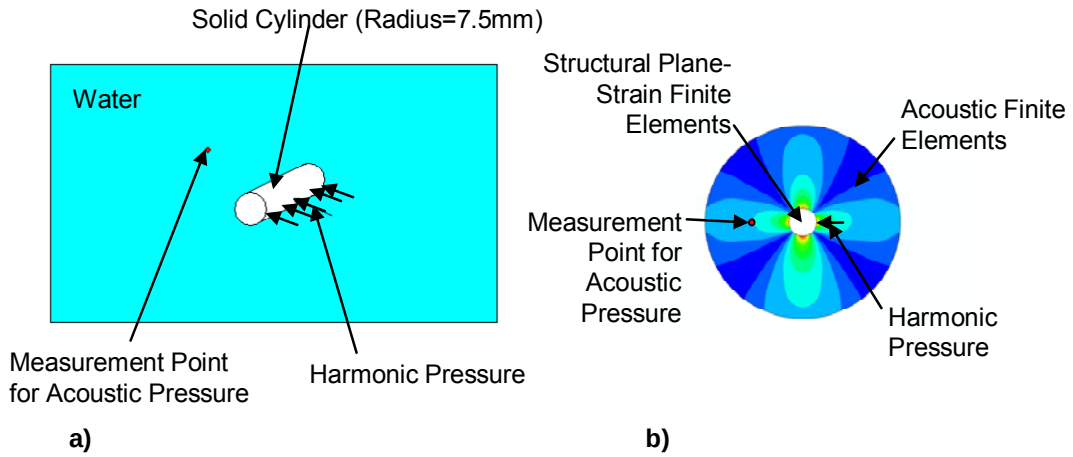

Figure 2.7. (a) Schematic and (b) finite element model of the simulated experiment for Example 2.

The frequency response of the system was obtained by solving the coupled FE equations for the harmonic pressure applied to the body over a range of frequencies while monitoring the amplitude of the steady-state acoustic field (i.e. fluid pressure) at a point in the surrounding fluid. The frequency response was then normalized by the maximum pressure amplitude occurring over the frequency spectrum. This normalization was done to account for the fact that the magnitude of the applied force is generally not accurately known in vibroacoustic applications. Due to the linearity of the fluid-structure equations with respect to this force, by normalizing the response, any uncertainty in the force magnitude is removed from the problem. It was found through several simulated and laboratory examples shown in [20] and [7] that the normalized frequency response of the acoustic emissions provides sufficient information to quantify material characteristics including viscoelastic properties.

Random Gaussian noise was added to the response data in order to add realism to the experiment and to explore the tolerance of the optimization algorithms to imperfect data. The random Gaussian noise was introduced in the simulated data as

$$P_i^{\exp} = P_i^{FEM}\left(1+0.1\eta\right) \tag{13}$$

Where $P_i^{\exp}$ is the i^{th} component of the experimental pressure response with noise, P_i^{FEM} is the i^{th} component of the FE simulated experimental pressure response, and η is a normally distributed random variable with unit variance and zero mean. This equation was found to produce realistic values of acoustic pressure deviations.

For this example, the viscoelastic parameters were constrained to a specific search range. Although the optimization algorithms considered here are all methods for unconstrained optimization, it is reasonable to assume that material parameters can be bound within a certain physical range. Unfortunately, due to the non-uniqueness of the rheological parameters and the fact that *a priori* material estimation to constrain the search range is strongly limited in many engineering applications including vibroacoustics, the search range must be very large, spanning multiple orders of magnitude. Table 2.1 shows the material properties used for the simulated experiment and the search ranges used for the optimization process. The parameters to be identified were the long-term elastic Young's modulus, E, the dimensionless viscous Young's modulus, g, Poisson's ratio, ν, and the relaxation time, τ, of the cylinder.

Table 2.1. Experimental material properties and optimization search ranges for Example 2.

Optimization Parameter	Target Value	Optimization Minimum	Optimization Maximum
E	**$3.19\text{x}10^{9}$**	**$1.0\text{x}10^{8}$**	**$1.0\text{x}10^{10}$**
ν	**0.26**	**0.20**	**0.48**
g	**0.1**	**0.01**	**0.99**
τ	**$1.0\text{x}10^{-6}$**	**$1.0\text{x}10^{-7}$**	**$1.0\text{x}10^{-5}$**

A maximum of 250 function evaluations (i.e. FE analyses) was used for the optimization algorithms. The GA had a population of 25 individuals and was limited to 10 generations. The RS algorithm had an initial set of 40 trial solutions, and five trial solutions were created randomly about each of the two search poles for 21 iterations. The SMARS algorithm also had an initial set of 40 trial solutions, and five trial solutions were created randomly about each of the two search poles along with one trial solution generated by the surrogate-model method for 19 iterations. Again, the standard deviation percentage was set to 100% for the SMARS and pure RS algorithms, to account for the size of the parameter ranges.

2.4.2.1 Results and Discussion

Since the viscoelastic parameter values are non-unique, the solution error, as was presented for the Rastrigin's example, is not applicable for this example, and is not shown. Figure 2.8 shows the average and standard deviation of the model error for the optimal trial solution, $\gamma^R\left(\vec{\alpha}^*\right)$, and Figure 2.9(a)-Figure 2.13(a) show the average and standard deviation of the simulated frequency responses of the normalized fluid pressure for the optimal trial solution compared to the experimental data for the ten trials of each algorithm. Similarly to the Rastrigin's function example, the genetic algorithm performed poorly compared to the other algorithms, while the SMARS cases with windows outperformed both the SMARS case without a window and the pure RS algorithm. Clearly from the frequency response shown in Figure 2.13 (a), given the limited number of function evaluations, the GA was unable to obtain a solution to even coarsely approximate the experimental frequency response.

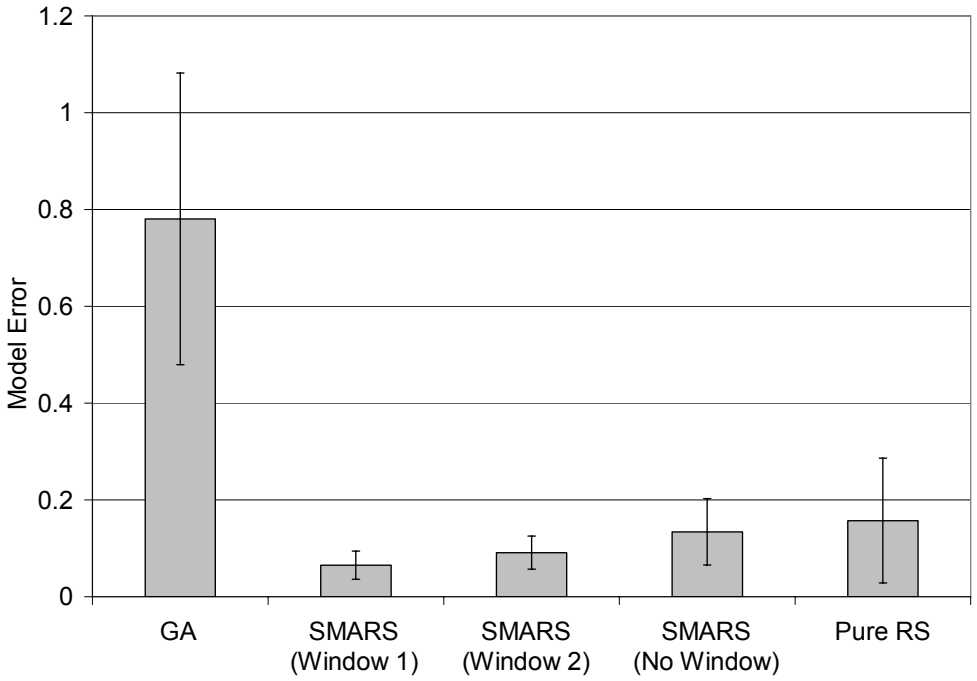

Figure 2.8. Average and standard deviation (error bars) of the model error, γ^R, for each algorithm for Example 2.

Figure 2.9(b)-Figure 2.13(b) show the average and standard deviation of the mechanical loss, $\tan\left[\delta(\omega)\right]$, and Figure 2.9(c)-Figure 2.13(c) show the average and standard deviation of the equivalent elastic modulus, $E^{eq}(\omega)$, for the solutions of the ten trials of each algorithm compared to the respective quantities defined by the parameters used to simulate the experiment. In general, the accuracy of the viscoelastic characteristics directly corresponds to the accuracy of the acoustic response. However, in all cases the accuracy of the mechanical loss parameter was significantly less than the accuracy of the equivalent elastic modulus. As shown in [7], the inaccuracy of the mechanical loss and the corresponding lack of effect on the acoustic response are likely due to the low amount of damping included in the system through viscoelasticity, which resulted in the low sensitivity of the acoustic response to relatively large deviations of that characteristic.

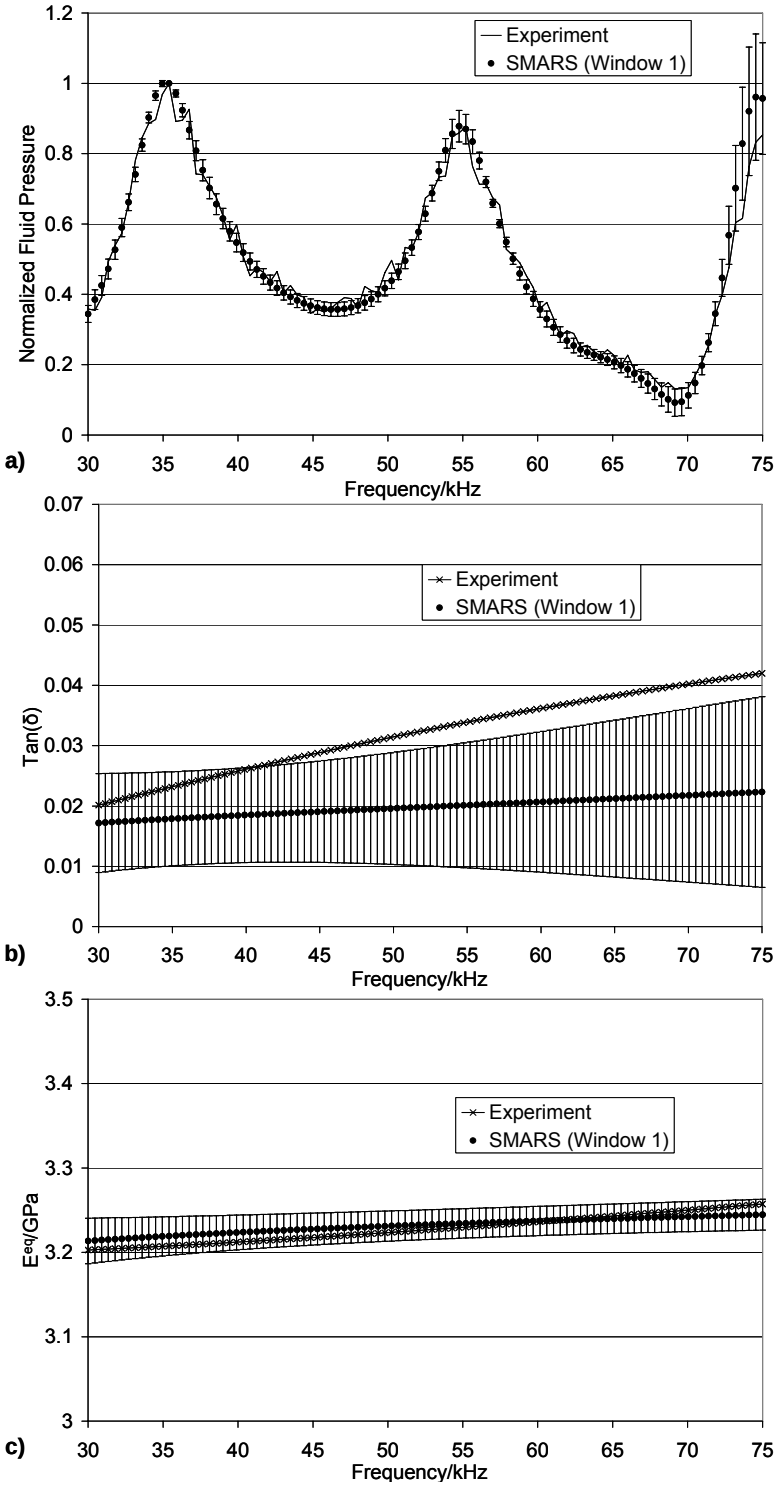

Figure 2.9. Average and standard deviation (error bars) of the frequency responses of (a) the normalized fluid pressure, (b) the mechanical loss, tan[δ(ω)], and (c) the equivalent elastic modulus, $E^{eq}(\omega)$, for the optimized parameter values compared to the simulated experimental data, for SMARS with Window 1 for Example 2.

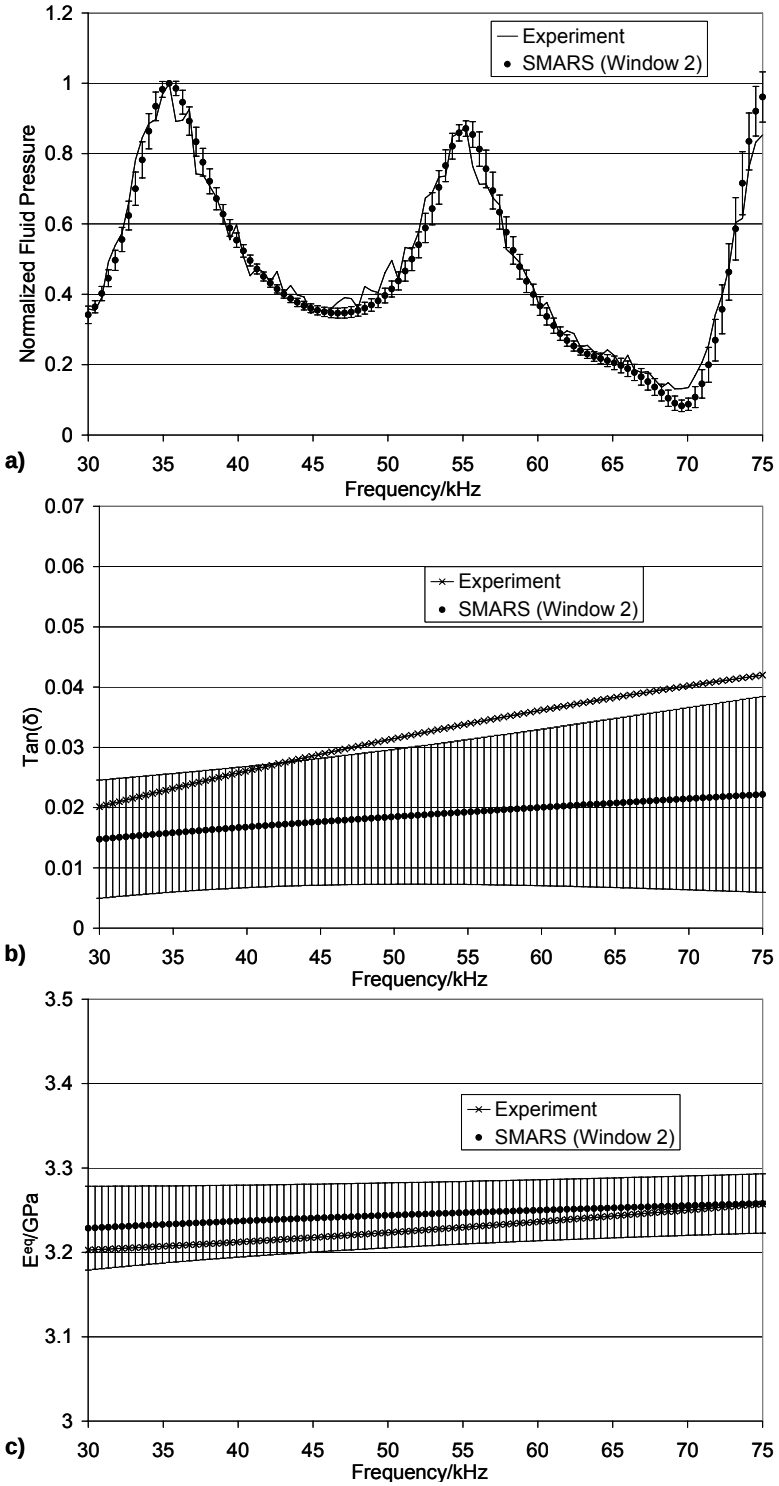

Figure 2.10. Average and standard deviation (error bars) of the frequency responses of (a) the normalized fluid pressure, (b) the mechanical loss, tan[δ(ω)], and (c) the equivalent elastic modulus, $E^{eq}(\omega)$, for the optimized parameter values compared to the simulated experimental data, for SMARS with Window 2 for Example 2.

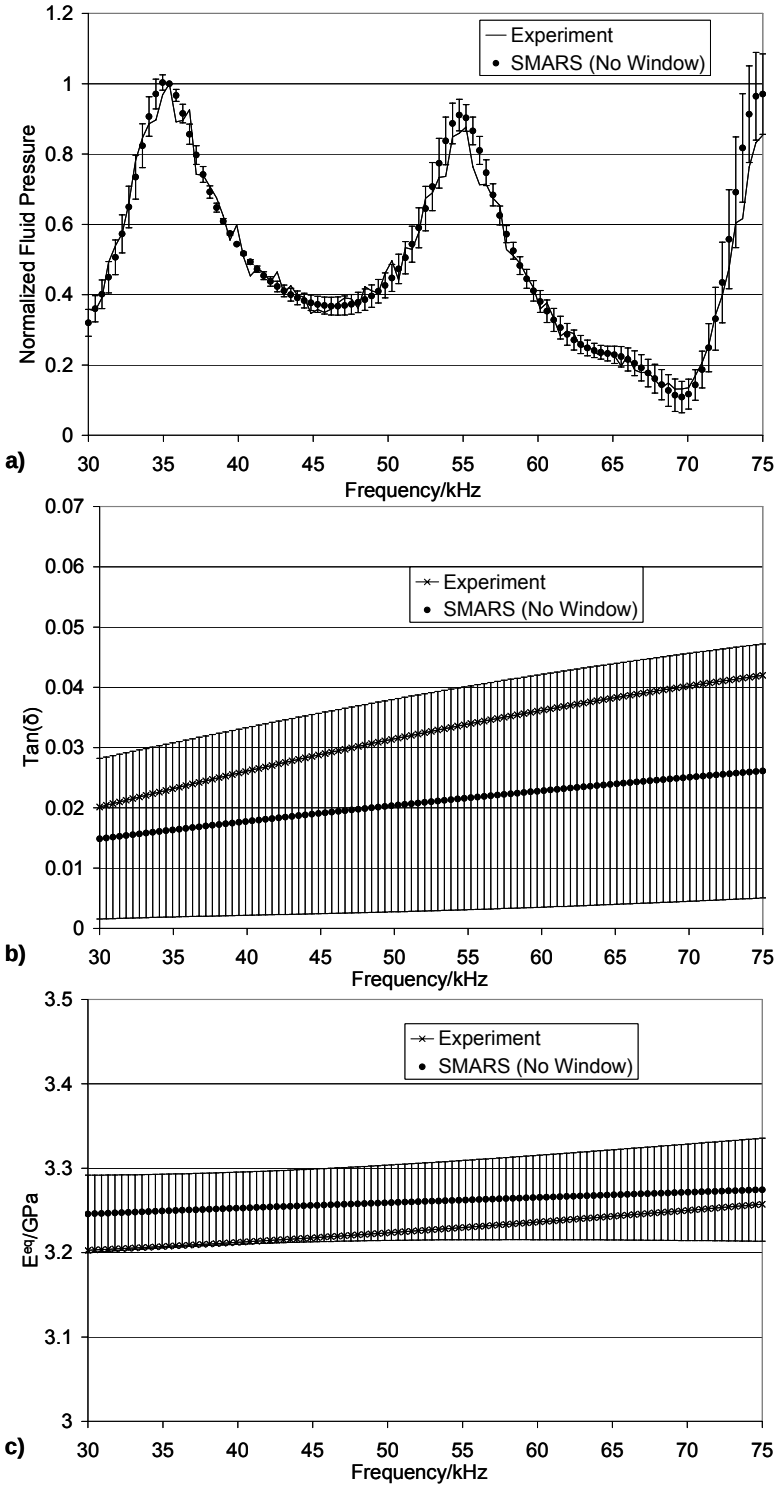

Figure 2.11. Average and standard deviation (error bars) of the frequency responses of (a) the normalized fluid pressure, (b) the mechanical loss, tan[δ(ω)], and (c) the equivalent elastic modulus, $E^{eq}(\omega)$, for the optimized parameter values compared to the simulated experimental data, for SMARS with no window for Example 2.

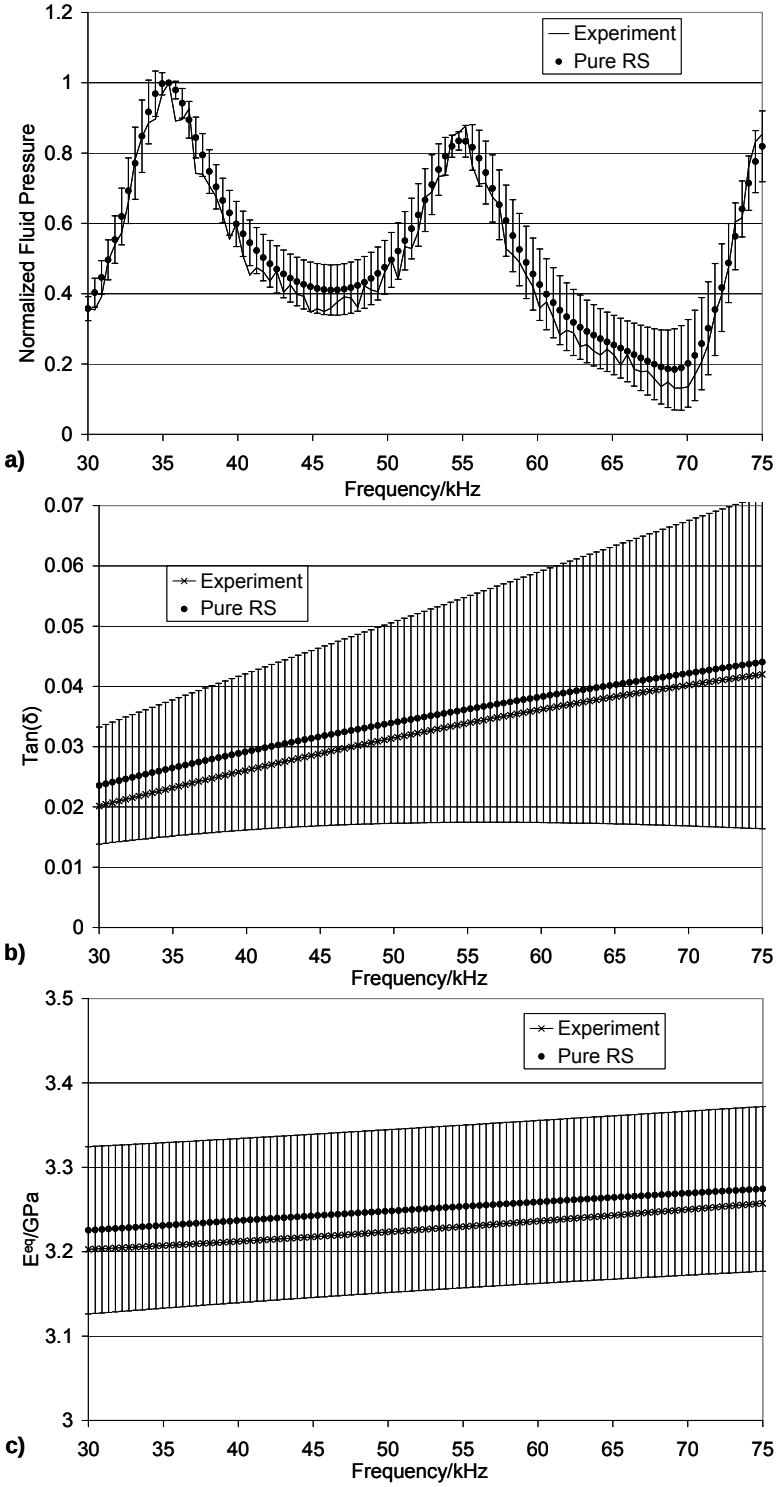

Figure 2.12. Average and standard deviation (error bars) of the frequency responses of (a) the normalized fluid pressure, (b) the mechanical loss, tan[δ(ω)], and (c) the equivalent elastic modulus, $E^{eq}(\omega)$, for the optimized parameter values compared to the simulated experimental data, for the pure RS for Example 2.

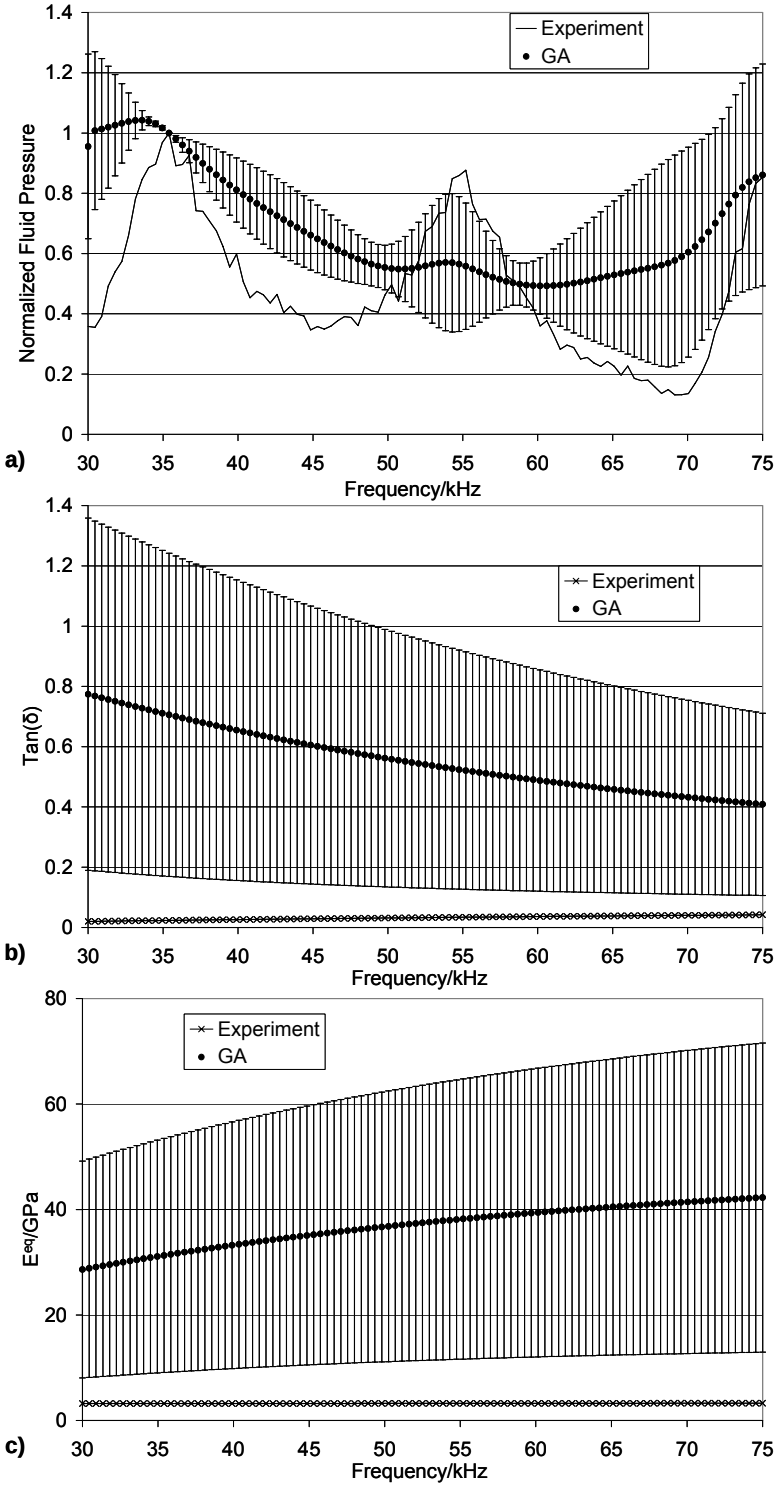

Figure 2.13. Average and standard deviation (error bars) of the frequency responses of (a) the normalized fluid pressure, (b) the mechanical loss, tan[δ(ω)], and (c) the equivalent elastic modulus, $E^{eq}(\omega)$, for the optimized parameter values compared to the simulated experimental data, for the GA for Example 2.

Table 2.2 shows the average and standard deviation of the optimal Poisson's ratio, ν, for the 10 trials of each algorithm compared to the actual solution. Again the SMARS cases with windowing consistently obtained more accurate results than the other algorithms, while the GA, SMARS without a window, and the pure RS obtained similar results. Unfortunately, for this experiment, the results for Poisson's ratio provide little insight into the optimization performance. It was found for this experiment that the results for Poisson's ratio were generally less accurate than the viscoelastic characteristics due to the lack of sensitivity of the experiment to Poisson's ratio [7], regardless of the optimization algorithm used. With this in consideration, for this example, all five test cases produced what would be considered acceptable results for Poisson's ratio. The solution capabilities of all optimization algorithms are similarly limited by insensitivity of parameters and general ill-posedness which occur in many inverse problems.

Table 2.2. Results for Poisson's ratio, ν, for Example 2.

Optimization Algorithm	Average	Standard Deviation
Actual	**0.26**	**-**
GA	**0.272**	**0.069**
SMARS (Window 1)	**0.236**	**0.034**
SMARS (Window 2)	**0.232**	**0.026**
SMARS (No Window)	**0.292**	**0.069**
Pure RS	**0.254**	**0.053**

Figure 2.14 shows the average model error for the current optimal trial solution, $\gamma^R\left(\vec{\alpha}^*\right)$, at each iteration versus the number of function evaluations for the SMARS and RS test cases. In this example, the results show that the SMARS trials

without a window behaved almost identically to the pure RS trials. Both SMARS cases with windows show improved convergence rates over the other methods, and again these two cases behaved similarly to each other throughout the optimization process. Again, the SMARS cases with windows obtained comparable average model errors in nearly 100 fewer function evaluations to that of the pure RS case at 250 function evaluations.

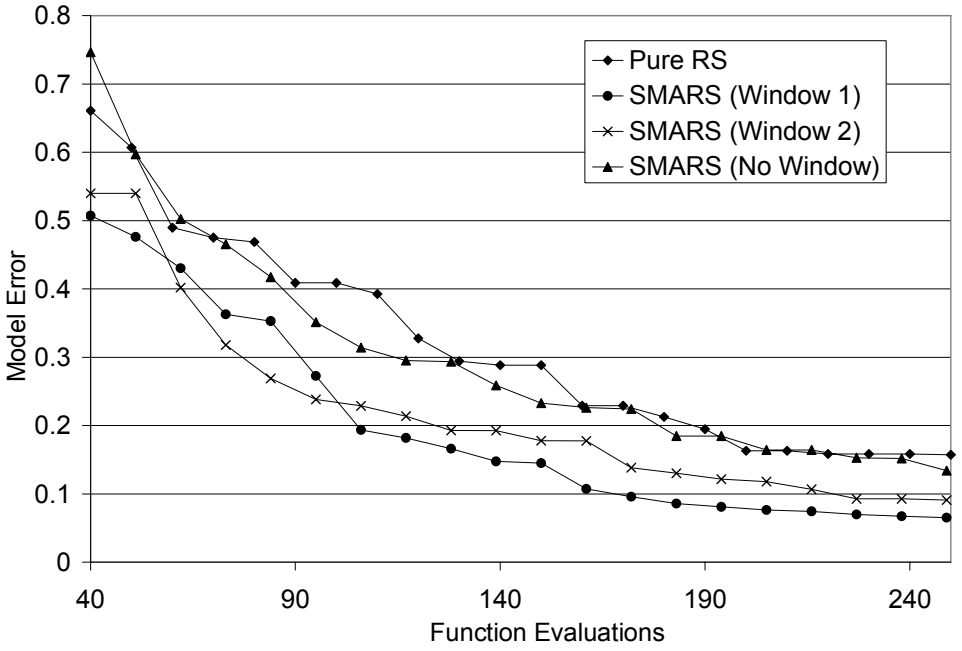

Figure 2.14. Average model error, γ^R, versus the number of function evaluations for the SMARS and pure RS test cases for Example 2.

Figure 2.15 shows the average and standard deviation of the model error for the current optimal trial solution, $\gamma^R\left(\vec{\alpha}^*\right)$, compared to the model error of the surrogate-model estimates, $\gamma^R\left(\vec{\alpha}^{sm}\right)$, at each iteration versus the number of function evaluations for the three SMARS test cases. The Window 1 trials clearly exhibit a significant increase in convergence rate due to the surrogate-model throughout the iterations. Also, the low standard deviation of the model error of the surrogate-model estimates

for the Window 1 case indicates that the surrogate-model accurately mapped the response surface consistently throughout the optimization process, resulting in fewer false predictions. Alternatively, the surrogate-model estimates for the Window 2 case show a similar average model error, but a larger standard deviation of model error, while the SMARS case without a window showed both a larger average and standard deviation of model error over the optimization iterations.

The increase in standard deviation of the model error in the Window 2 case and the overall ineffectiveness of the surrogate-model in the case without a window indicates that as the size of the window increases the effectiveness of the surrogate-model method decreases. This result is due to the failure of the surrogate-model to accurately map the response surface when the window size becomes too large. However, notice that the response surface being mapped for the Window 2 case is approximately twice the size of the Window 1 case, yet in both cases the surrogate-model remains effective in increasing the convergence speed of the SMARS algorithm in comparison to the SMARS case without a window. This shows that the search space being mapped by the surrogate-model must be restricted in order to obtain consistent and accurate estimates of the solution. The lack of sensitivity of window size is important as this indicates that although a smaller window size is preferable, there is less of a need for user interaction during the optimization process to choose an optimal window size.

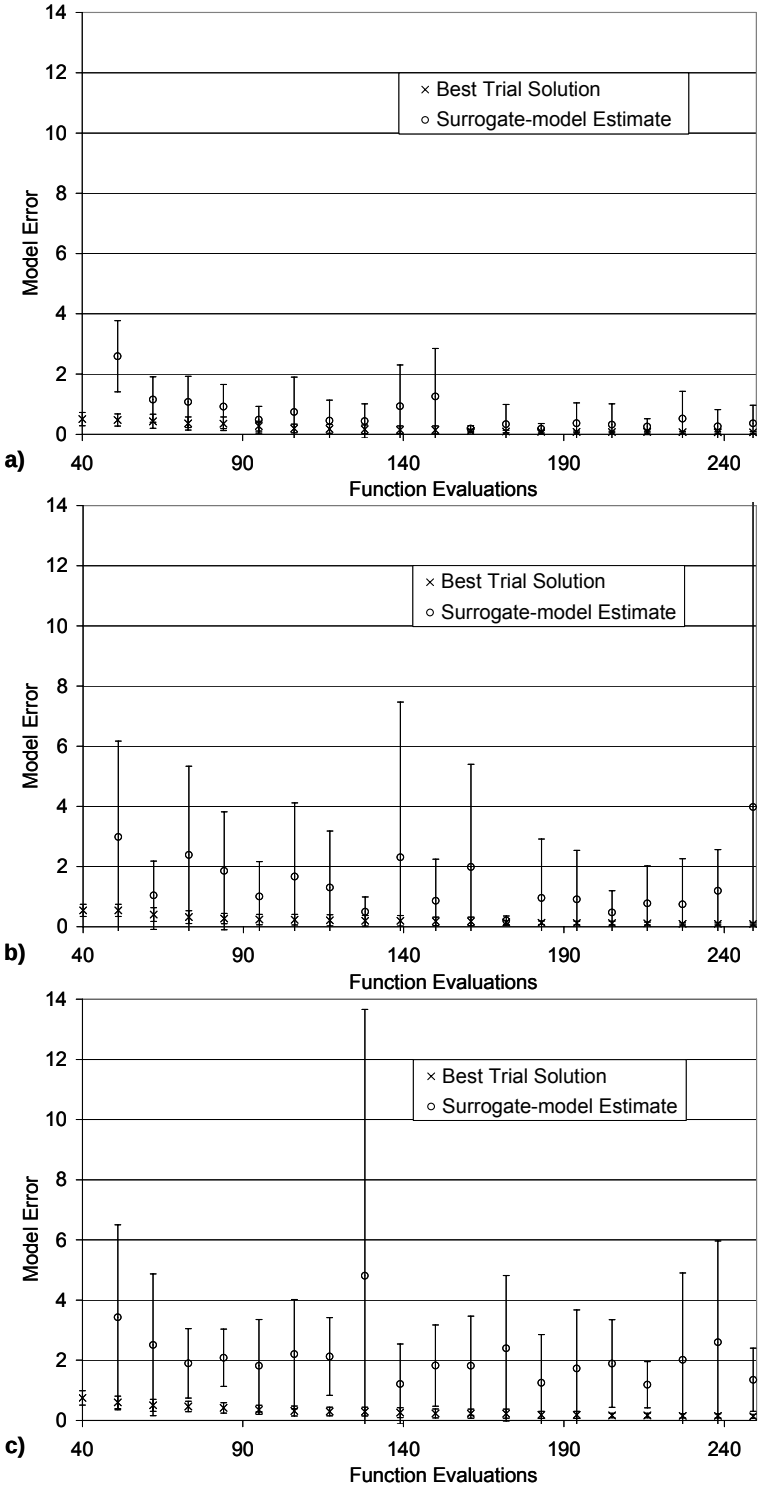

Figure 2.15. Average and standard deviation (error bars) of the model error, γ^R, of the best trial solutions and the model error of the surrogate-model estimates, versus the number of function evaluations for SMARS with (a) Window 1, (b) Window 2, and (c) no window for Example 2.

For this example, an additional set of tests was performed to further assess the increased optimization speed of the SMARS algorithm. The GA was applied to solve the problem again, but with the number of functions evaluations increased to 1200 FE analyses. Figure 2.16 shows the average and standard deviation of the model error for the GA with 250 function evaluations, the GA with 1200 function evaluations, and the SMARS algorithm with Window 1 with 250 function evaluations. The GA results with 1200 function evaluations are clearly greatly improved over the GA with 250 function evaluations, yet the SMARS algorithm still outperforms the GA even with 950 fewer function evaluations.

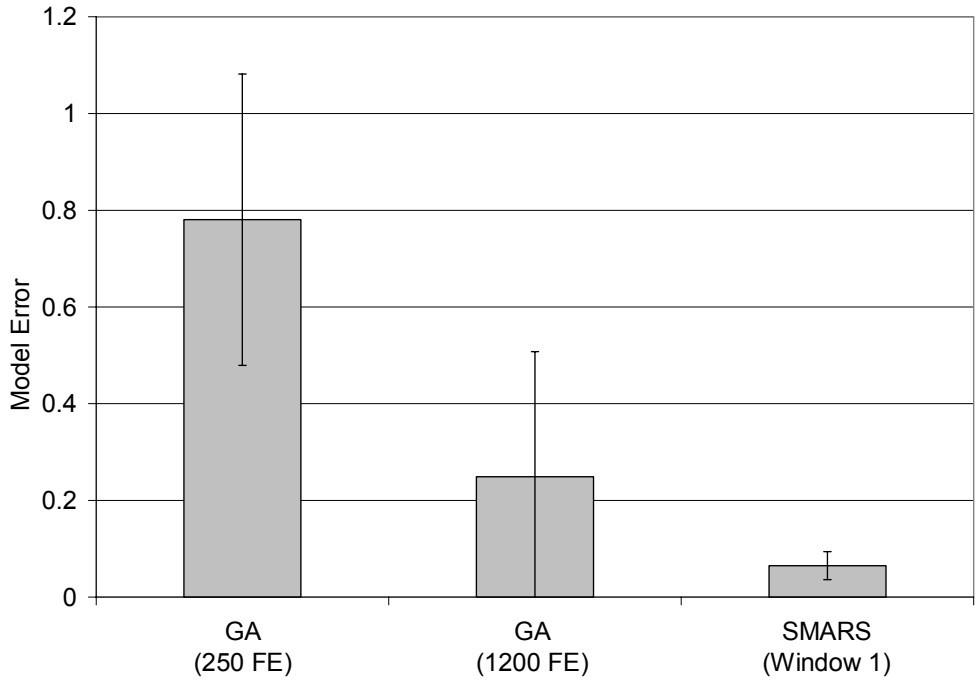

Figure 2.16. Average and standard deviation (error bars) of the model error, γ^R, for the GA with 250 function evaluations (FE), the GA with 1200 FE, and SMARS with Window 1 with 250 FE for Example 2.

2.4.3 Inverse Diffusivity Identification Using Temperature Measurements

Lastly, an example was considered to show the capabilities of the SMARS algorithm for a problem with a high dimensional parameter space. The problem consisted of the characterization of the spatial distribution of thermal diffusivity in a functionally graded material (FGM) given applied thermal boundary conditions and a discrete set of transient temperature measurements throughout the solid.

In addition, to eliminate spurious oscillatory solutions for the inverse problem a first-order Tikhonov regularization approach was used. Thus, the model error for the optimization procedure for this problem was defined as

$$\gamma^R\left(D(\vec{x})\right) = \left\|\vec{T}^R\left(D(\vec{x})\right) - \vec{T}^{exp}\right\|_{l_2} + \lambda\left\|\frac{\partial D(\vec{x})}{\partial \vec{x}}\right\|_{L_2}. \tag{14}$$

Where $D(\vec{x})$ is the spatial distribution of thermal diffusivity, $\vec{T}^R\left(D(\vec{x})\right)$ and $\vec{T}^{exp}$ are the vectors of computed and experimentally measured temperatures, respectively, sampled at discrete times for a given set of sensor locations, and λ is the regularization parameter. For a thorough treatment of Tikhonov regularization see [2]. A transient heat transfer FEM was used as the numerical representation of the experiment [9].

In order to represent the spatially varying thermal diffusivity of the FGM, a separate mesh (in addition to the FE mesh) was defined over the solid domain, and the diffusivity was approximated within each element of the mesh as

$$D(\vec{x}) = \left[N(\vec{x})\right]\left\{D^e\right\}. \tag{15}$$

Where $\left[N(\vec{x})\right]$ is a row-vector containing interpolation function and $\left\{D^e\right\}$ is a column-vector containing nodal diffusivity values for a given element of the mesh. Therefore, the inverse problem becomes the identification of the nodal diffusivity values based on the measured temperatures and constrained by the first-order regularization.

For the inverse problem, two separate experiments were simulated using FEM. The experiments consisted of a plate with convective boundary conditions on the top and bottom and insulated on all other sides (i.e. a one-dimensional problem). The temperature was measured at five equally spaced locations along the length of the plate, as shown in Figure 2.17. The initial temperature of the plate was taken to be $25^{o}C$ and the convective coefficients (normalized by heat capacity) were taken to be $0.1m/s$ on the top and bottom of the plate. The first experiment consisted of a hot fluid applied to the top of the plate and a cold fluid applied to the bottom, while the second experiment reversed the applied boundary conditions (i.e. cold fluid on the top, hot fluid on the bottom). This approach was deemed necessary in order to obtain a unique spatial variation of the thermal properties.

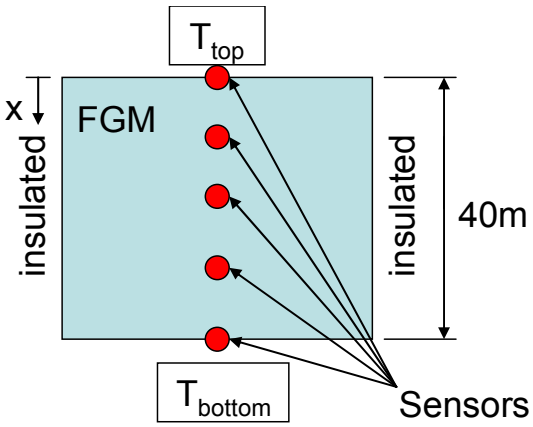

Figure 2.17. Schematic of the simulated experiment for Example 3.

The external temperature at the top and bottom boundaries were taken as $100^{o}C$ and $0^{o}C$ respectively for the first experiment, then $0^{o}C$ and $100^{o}C$ respectively for the second experiment. The temperature was sampled at the sensors every 100 seconds for a total duration of 500 seconds for both experiments. The thermal diffusivity for the plate was based on the properties of an Al_2O_3 / Al FGM [21], and

the distribution is shown in Figure 2.18. For the optimization process, the diffusivity was constrained to be between $1 m^2/s$ and $5 m^2/s$, which is a feasible range for the properties of the given FGM. The mesh used for the representation of diffusivity was taken to have 21 equally spaced nodes along the length of the plate with linear interpolation.

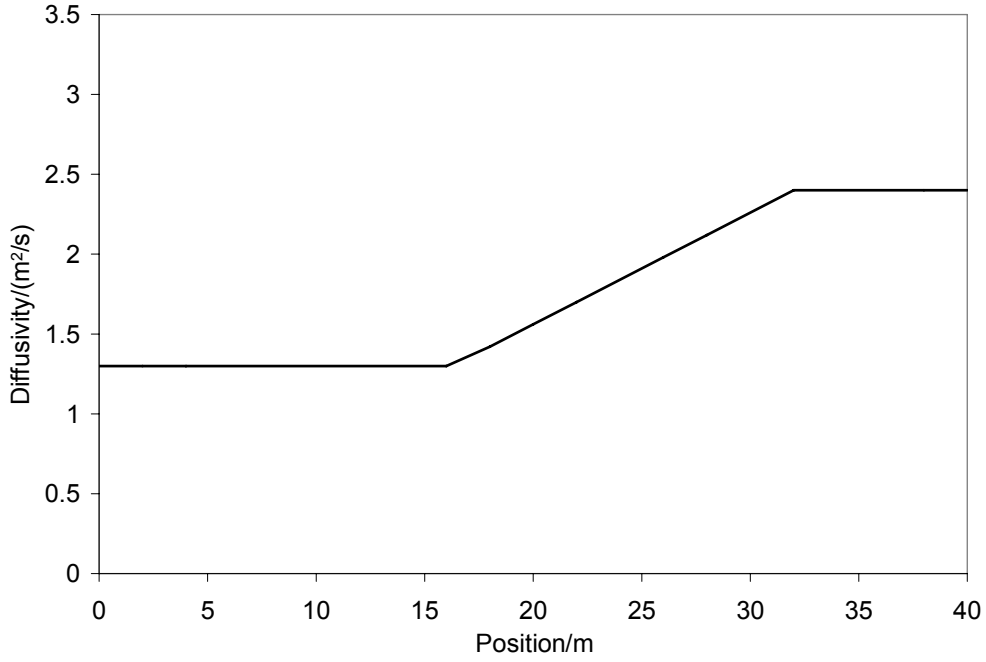

Figure 2.18. Functionally graded spatial distribution of the experimental diffusivity for Example 3.

A maximum of 5,000 function evaluations was used for the optimization algorithms and the model error tolerance was set to 3.0. This error value was found to be adequate for this problem through trial runs. The GA had a population of 50 individuals and was limited to a maximum of 100 generations. The RS algorithm had an initial set of 50 trial solutions, and five trial solutions were created randomly about each search pole for a maximum of 495 iterations. The SMARS algorithm also had an initial set of 40 trial solutions, and five trial solutions were created randomly about

each search pole along with one trial solution generated by the surrogate-model method for a maximum of 450 iterations. For this example, the standard deviation percentage was set to 10% for the SMARS and pure RS algorithms, to account for the smaller size of the parameter ranges.

2.4.3.1 Results and Discussion

Figure 2.19 shows the average and standard deviation of the number of function evaluations performed to reach the error tolerance, and Figure 2.20-Figure 2.22 show the average and standard deviation of the diffusivity solutions for the 10 trials of each algorithm. Again, the SMARS algorithm outperformed both the GA and pure RS algorithms. In all cases the SMARS algorithm was able to reach the error tolerance in less than one fifth of the number of function evaluations required by the other two algorithms. Furthermore, the SMARS algorithm was the only one that reached the error tolerance in all of the 10 trials, thereby attaining highly accurate diffusivity representations in all trials. The GA again proved to be the weakest method for the selected problem. The GA was never able to reach the specified error tolerance within 5,000 function evaluations. More importantly, the diffusivity results obtained by the GA were far less accurate than for the other two algorithms. The pure RS algorithm only reached the specified error tolerance in half of the trials, and the diffusivity results show a noticeable deterioration compared to the SMARS results.

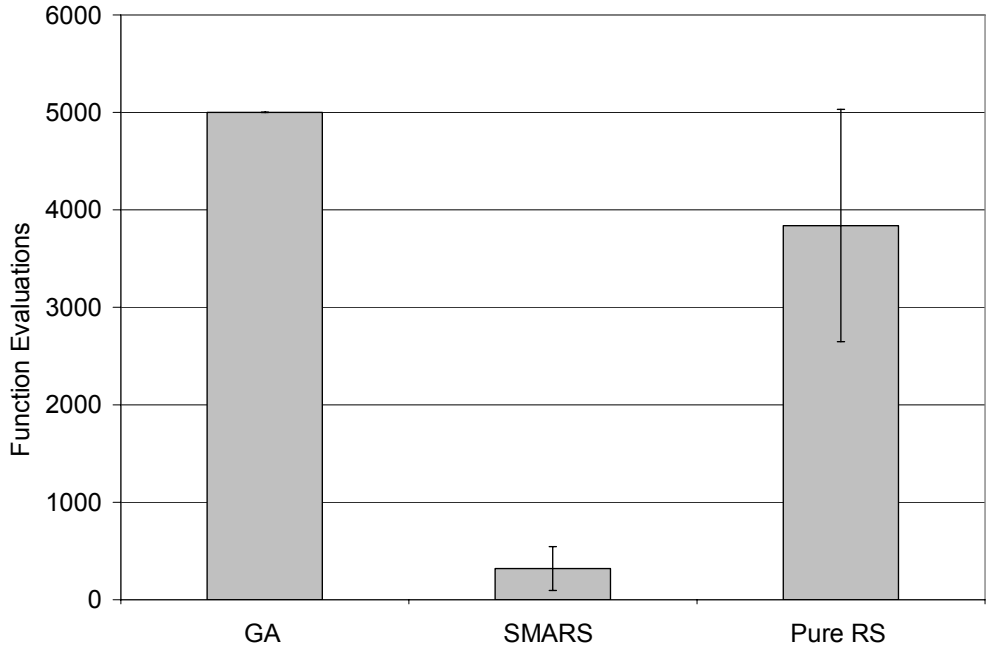

Figure 2.19. Average and standard deviation (error bars) of the number of function evaluations for each algorithm for Example 3.

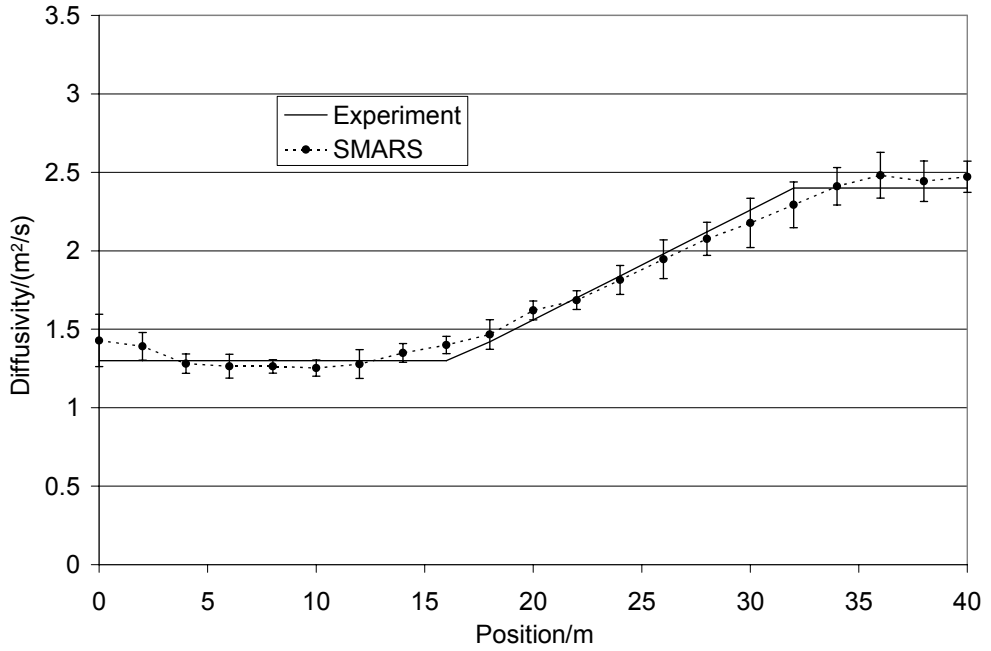

Figure 2.20. Average and standard deviation (error bars) of the optimized diffusivity distribution compared to the experimental data, for SMARS for Example 3.

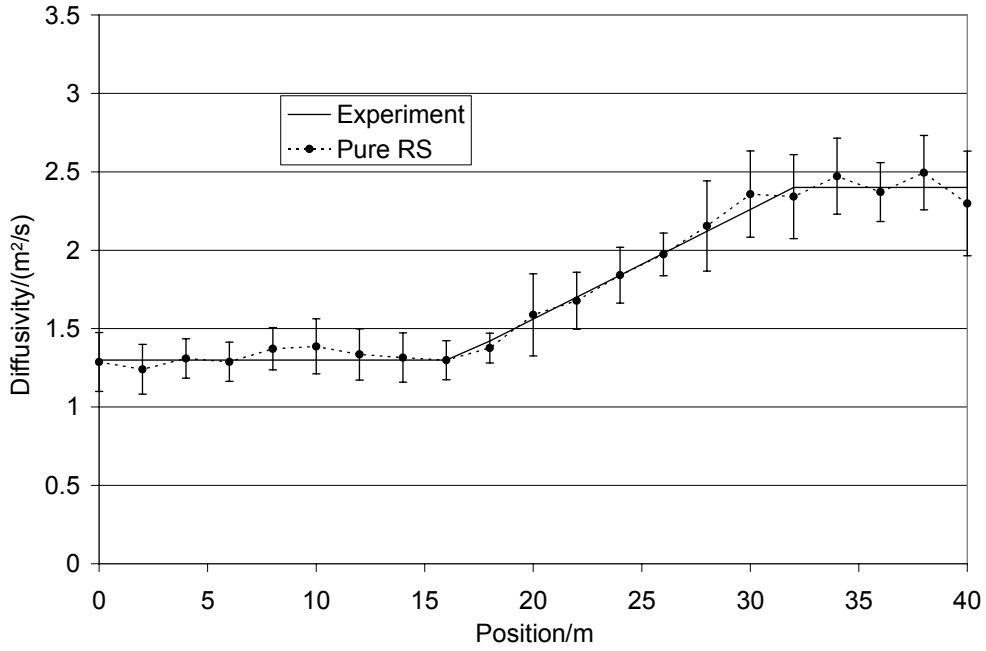

Figure 2.21. Average and standard deviation (error bars) of the optimized diffusivity distribution compared to the experimental data, for the pure RS for Example 3.

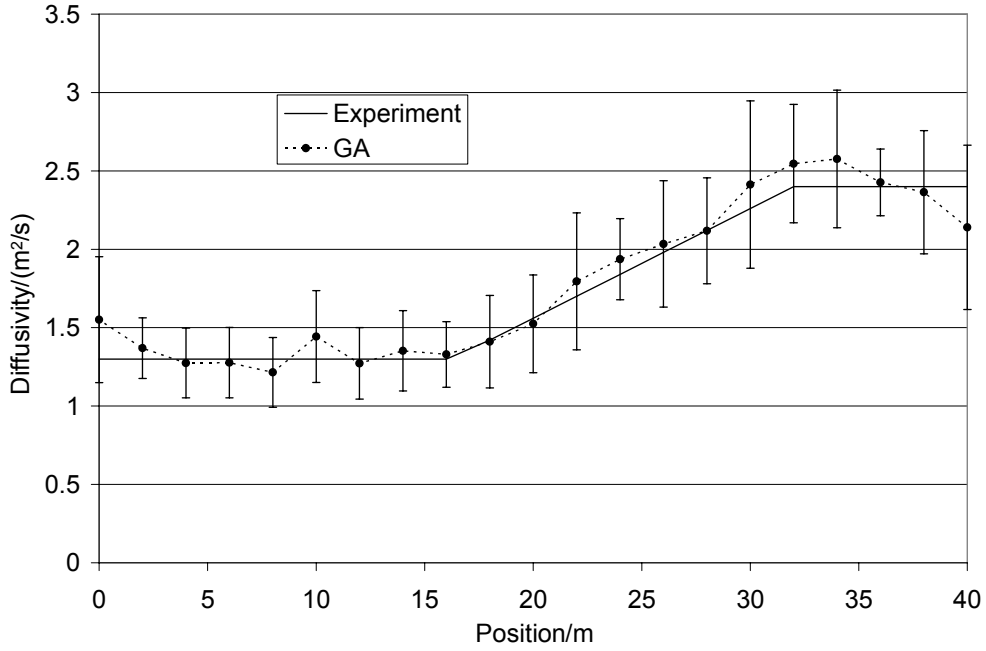

Figure 2.22. Average and standard deviation (error bars) of the optimized diffusivity distribution compared to the experimental data, for the GA for Example 3.

Figure 2.23 shows the average model error for the current optimal trial solution, γ^R, at each iteration versus the number of function evaluations for the SMARS and RS test cases. The results show that the SMARS algorithm has a much higher rate of convergence than the Pure RS algorithm, and the surrogate-model portion of the SMARS algorithm clearly accelerates the RS towards a solution.

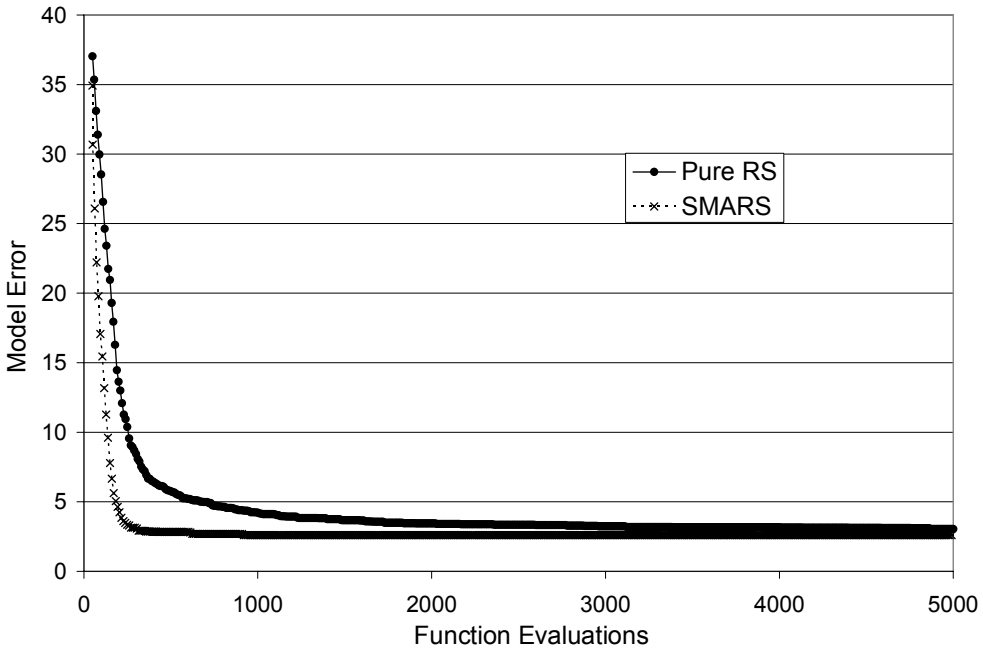

Figure 2.23. Average model error, γ^R, versus the number of function evaluations for the SMARS and pure RS test cases for Example 3.

2.5 Conclusions

The Surrogate-Model Accelerated Random Search (SMARS) Algorithm for global optimization with computationally expensive objective functions was presented. The SMARS algorithm was shown to efficiently combine the random search algorithm for global search space probing with the surrogate-model method applied to local regions of the search space, thereby taking advantage of the benefits of both algorithms, while

offsetting their respective weaknesses. Through several numerical examples, the SMARS algorithm demonstrated the ability to be robust in the presence of highly non-convex response surfaces, search vast ranges of parameter values, and be tolerant to high-dimensional parameter spaces, while consistently obtaining accurate solutions in a limited number of function evaluations. Furthermore, the algorithm was shown through the examples to be able to locate solutions in far fewer function evaluations than both a genetic algorithm and a random search algorithm.

REFERENCES

[1] R.A. Albanese, H.T. Banks, and J.K. Raye, Nondestructive evaluation of materials using pulsed microwave interrogating signals and acoustic wave induced reflections, Inverse Problems 18 (2002) 1935-1958.

[2] O.M. Alifanov, Inverse Heat Transfer Problems, Springer-Verlag, Berlin; New York, 1994.

[3] W. Aquino and J.C. Brigham, Self-learning finite elements for inverse estimation of thermal constitutive models, International Journal of Heat and Mass Transfer 49 (2006) pp 2466-2478.

[4] C. Aristegui and S. Baste, Optimal recovery of the elasticity tensor of general anisotropic materials from ultrasonic velocity data, Journal of the Acoustical Society of America 101 (1997) 813-833.

[5] B. Audoin, Non-destructive evaluation of composite materials with ultrasonic waves generated and detected by lasers, Ultrasonics 40 (2002) 735-740.

[6] J. Bercoff, S. Chaffai, M. Tanter, L. Sandrin, S. Catheline, M. Fink, J.L. Gennisson, and M. Meunier, In vivo breast tumor detection using transient elastography, Ultrasound in Medicine and Biology 29 (2003) 1387-1396.

[7] J.C. Brigham and W. Aquino, Inverse Estimation of Viscoelastic Material Properties for Solids Immersed in Fluids using Vibroacoustic Techniques, Journal of Applied Physics 101 (2007) 23509-1-14.

[8] S.H. Brooks, A Discussion of Random Methods for Seeking Maxima, Operations Research 6 (1958) 244-251.

[9] R.D. Cook, D.S. Malkus, M.E. Plesha, and R.J. Witt, Concepts and Applications of Finite Element Analysis. Fourth ed, John Wiley & Sons, New

York, NY, 2002.

[10] F.A. Duck, Physical properties of tissue: a comprehensive reference book, Academic Press, London; San Diego, Calif., 1990.

[11] M. Fatemi and J.F. Greenleaf, Ultrasound-stimulated vibro-acoustic spectrography, Science 280 (1998) 82-85.

[12] M. Fatemi and J.F. Greenleaf, Vibro-acoustography: An imaging modality based on ultrasound-stimulated acoustic emission, Proceedings of the National Academy of Sciences of the United States of America 96 (1999) 6603-6608.

[13] W.N. Findley, J.S. Lai, and K. Onaran, Creep and relaxation of nonlinear viscoelastic materials, with an introduction to linear viscoelasticity, North-Holland Pub. Co., Amsterdam, New York, 1976.

[14] D.E. Goldberg, Genetic algorithms in search, optimization, and machine learning, Addison-Wesley, Reading, Mass., 1989.

[15] J. Ladeji-Osias and N.A. Langrana, Analytical Evaluation of Tumors Surrounded by Soft Tissue, Proceeding of the 22nd Annual EMBS International Conference, IEEE, Chicago, IL, 2000, Vol. 3, 2114-2117.

[16] B.M. Learoyd and M.G. Taylor, Alterations with Age in Viscoelastic Properties of Human Arterial Walls, Circulation Research 18 (1966) 278-&.

[17] Q.S. Li, D.K. Liu, A.Y.T. Leung, N. Zhang, C.M. Tam, and L.F. Yang, Modelling of structural response and optimization of structural control system using neural network and genetic algorithm, Structural Design of Tall Buildings 9 (2000) 279-293.

[18] S.F. Masri, A.W. Smyth, A.G. Chassiakos, M. Nakamura, and T.K. Caughey, Training neural networks by adaptive random search techniques, Journal of Engineering Mechanics-Asce 125 (1999) 123-132.

[19] M. Mitchell, An introduction to genetic algorithm, MIT Press, Cambridge,

Mass., 1998.

[20] F.G. Mitri, Inverse determination of porosity from object's resonances, Journal of Applied Physics 96 (2004) 5866-5869.

[21] A. Neubrand, H. Becker, and T. Tschudi, Spatially resolved thermal diffusivity measurements on functionally graded materials, Journal of Materials Science 38 (2003) 4193-4201.

[22] H. Ogi, K. Sato, T. Asada, and M. Hirao, Complete mode identification for resonance ultrasound spectroscopy, Journal of the Acoustical Society of America 112 (2002) 2553-2557.

[23] B. Pichler, R. Lackner, and H.A. Mang, Back analysis of model parameters in geotechnical engineering by means of soft computing, International Journal for Numerical Methods in Engineering 57 (2003) 1943-1978.

[24] R.D. Reed and R.J. Marks II, Neural smithing: supervised learning in feedforward artificial neural networks, The MIT Press, Cambridge, Mass., 1999.

[25] R.G. Regis and C.A. Shoemaker, Constrained global optimization of expensive black box functions using radial basis functions, Journal of Global Optimization 31 (2005) 153-171.

[26] L.L. Rogers, F.U. Dowla, and V.M. Johnson, Optimal Field-Scale Groundwater Remediation Using Neural Networks and the Genetic Algorithm, Environmental Science & Technology 29 (1995) 1145-1155.

[27] M.A. Sumbatyan, A Method of Global Random Search in Inverse Problems with Application to the Problem of Recognizing the Shape of a Defect, Pmm Journal of Applied Mathematics and Mechanics 56 (1992) 779-781.

[28] V. Torczon and M.W. Trosset, Using Approximations to Accelerate Engineering Design Optimization, ICASE Report No. 98-33 NASA/CR, Sept. 1998

[29] S. Yan and B. Minsker, A dynamic meta-model approach to genetic algorithm solution of a risk-based groundwater remediation design model, Proceeding of the 2004 World Water and Environmental Resources Congress: Critical Transitions in Water and Environmental Resources Management, American Society of Mechanical Engineers, Salt Lake City, UT, United States, 2004, Vol. 3, 1962-1971.

[30] C. Zhang and R. Ordonez, Decentralized Adaptive Coordination and Control of Uninhabited Autonomous Vehicles via Surrogate Optimization, Proceeding of the American Control Conference, IEEE, Denver, CO, 2003, Vol. 3, 2205-2210.

CHAPTER 3

Inverse Viscoelastic Material Characterization using POD Reduced-Order Modeling in Acoustic-Structure Interaction

3.1 Abstract

A strategy is presented for applying the proper orthogonal decomposition (POD) technique for model reduction in computational inverse solution strategies for viscoelastic material characterization. POD is used to derive a basis of optimal dimension from a selection of possible solution fields which are generated through a traditional acoustic-structure interaction finite element model for a given vibroacoustic experiment. The POD bases are applied with the Galerkin weak-form finite element method to create a reduced-order numerical model with decreased computational cost, but which still maintains accuracy close to that of the original full-order finite element model. The reduced-order model is then combined with a global optimization technique to identify estimates to the viscoelastic material properties of a fluid immersed solid from vibroacoustic tests. A strategy is also presented to select the viscoelastic parameters of the initial full-order analyses used to create the POD bases. The selection process is shown through an example to maximize the generalization capabilities of the reduced-order model over the material search space for a minimal number of full-order analyses. Two examples are then presented in which the parameters of rheological viscoelastic models are identified for solids immersed in water, which are subject to a steady-state harmonic pressure while the acoustic response is measured at a point in the surrounding fluid. The POD reduced-order models were able to generalize over the material search domains for the inverse problems. Therefore, the reduced-order solution strategy was capable of identifying accurate estimates to the viscoelastic behavior of the solids with minimal computational expense.

3.2 Introduction

The use of ultrasound radiation force has shown considerable promise for nondestructive and noninvasive imaging and characterization of biological soft tissues [13, 31, 35]. The particular testing methodology considered here uses the radiation force of ultrasound to produce a low frequency (normally kilohertz) oscillating localized force on a solid immersed in fluid (e.g. internal biological structure). The solid is vibrated to a steady-state condition, and the amplitude of the resulting acoustic emission is measured with a hydrophone. The measured acoustic emission contains significant information about the rate dependent mechanical behavior of the tissue, and minimal measurements have been shown to provide sufficient information to characterize both stiffness and damping properties of solids [11].

Like many other inverse characterization problems in engineering (e.g. [4, 5, 7]), with any degree of complexity in the system, closed-form solutions for the characterization of material properties from vibroacoustic tests becomes intractable. Therefore, the typical approach is to combine a numerical representation of the system (e.g. finite element or boundary element methods) with a nonlinear optimization technique to identify the properties which minimize the difference between the numerical representation and the experiment. Yet, the computational expense of numerical representations of biological systems along with the simulation demands of global optimization can make these solution strategies impractical, even considering modern developments in scientific supercomputing.

In previous work [10], an optimization strategy was developed to ease the computational cost for the vibroacoustic inverse problem by reducing the number of computationally expensive numerical analyses necessary to identify a solution. However, the computational expense is particularly significant for the numerical solution of the Helmholtz-type equations occurring in the steady-state analysis of soft-

tissues in the frequency ranges used in vibroacoustic testing methods [19, 20]. Therefore, for applications of this type it becomes necessary to identify methods to further reduce the expense of the numerical simulations.

Proper orthogonal decomposition (POD) is a technique which can be used with either experimental or simulated field data to derive a reduced-order set of basis functions capable of being used in a numerical representation of the system [3]. These basis functions are the optimal set, in an average sense, for representing the field data for the given order. Therefore, the basis is expected to produce an accurate and efficient numerical representation of the system, provided sufficient information exists in the field data.

POD reduced-order modeling has been shown in many cases to provide accurate numerical representations for complex systems with minimal computational cost [17, 18, 27]. In addition, POD has been applied to several inverse problem methodologies, such as optimal control [6, 26, 28, 33], microstructural design [2, 15], and non-destructive testing and system identification [8, 23, 32]. However, work has yet to be shown (to our knowledge) for using POD reduced-order modeling for inverse viscoelastic material characterization from steady-state dynamic testing. Furthermore, if using simulated field data to create the POD bases (as is the case in this work), a particular challenge is deciding how to select the parameter realizations for the full-order analyses to create a POD basis which is capable of accurately capturing a wide range of solutions.

In the following section, the inverse problem and corresponding solution strategy are described for the characterization of material properties from vibroacoustic tests. Next, the formulation of the steady-state dynamic acoustic-structure interaction finite element (FE) method used to model the vibroacoustic test is presented. The FE formulation is shown for both the full-order and POD reduced-order cases. Then the

methodology is presented for choosing the material realizations for generating the fields used to create the POD bases for maximum generalization. Lastly, one example is shown to display the generalization capabilities of the proposed sampling method, and two example inverse characterization problems are presented, followed by the conclusions.

3.3 Inverse Problem Formulation and Solution Strategy

The inverse problems considered here consist of identifying the parameters of viscoelastic constitutive representations for solids immersed in fluid. For this identification a harmonic force was applied at some location in the solid, and the magnitude of the resulting steady-state dynamic acoustic pressure response was measured at some point(s) in the surrounding fluid. In addition, the pressure response was normalized by the maximum pressure amplitude occurring over the frequency spectrum. This normalization was done to account for the fact that the magnitude of the applied force is generally not accurately known in vibroacoustic applications. Assuming the acoustic response to be linear with respect to the force magnitude (i.e. that the acoustic response due to the excitation is a linear perturbation), any uncertainty in the force magnitude is removed from the problem. It was found through several simulated and laboratory examples shown in [30] and [11] that the normalized frequency response of the acoustic emissions provides sufficient information to quantify material characteristics including viscoelastic properties.

In order to obtain a solution, the inverse problem was cast as an optimization problem where parameters were to be identified which minimize an error functional that characterizes the difference between the experimentally measured pressure response and the pressure response obtained from a numerical model of the system. For this work the error functional will be defined as

$$J(\vec{\gamma}) = \frac{1}{N^p} \left\| p^{exp}(\vec{x}, \omega) - p^{sim}(\vec{\gamma}, \vec{x}, \omega) \right\|_{l_2(\vec{x},\omega)} \quad (1)$$

$\vec{\gamma}$ is the vector of material parameters to be identified, $p^{exp}(\vec{x}, \omega)$ is the normalized experimentally measured pressure response at a given position, $\vec{x}$, and frequency, ω, $p^{sim}(\vec{\gamma}, \vec{x}, \omega)$ is the normalized pressure response from the numerical model (in this work a POD reduced-order numerical model) for a given set of parameters at a given position and frequency, and N^p is the total number of discrete sampling points in space and frequency. $\| \|_{l_2(\vec{x},\omega)}$ is the discrete $l_2 - norm$ (SRSS) over the measurement points and frequencies, therefore, $J(\vec{\gamma})$ can also be referred to as the discrete $L_2 - error$ of the approximation.

Through several numerical studies, the typical optimization search spaces for these inverse problems were found to be non-convex, which is common in applications which use sparse measurement data such as nondestructive and noninvasive characterization. Thus, a global optimization algorithm was applied to solve the above minimization problem. Furthermore, biological applications often require a broad search range for the material parameters, as the properties can vary drastically depending on the location in the body, age, and presence of disease [9, 12, 24, 25]. Therefore, the surrogate-model accelerated random search (SMARS) algorithm was applied to identify the parameters which minimize the functional described in Equation (1). The SMARS algorithm is a global stochastic search algorithm, which is capable of searching over large parameter domains with a minimal number of evaluations of the error functional [10].

3.4 Forward Vibroacoustic Problem

As vibroacoustic methods for characterization are still a developing technology, it is necessary to analyze the current laboratory testing systems, while also addressing the intended uses and challenges therein. As such, this work will consider simple

systems (compared to *in vivo* biological systems) of viscoelastic solids immersed in semi-infinite domains of water with negligible flow, which is a suitable representation of the gel tissue phantoms and water tank used in a developmental system. However, the general methodologies presented, with only some modification of the governing partial differential equations (PDEs) and corresponding boundary/initial conditions, are applicable to any given vibroacoustic-based system.

3.4.1 Steady-State Dynamic Acoustic-Structure Governing Equations

In the following derivations vectors are shown with arrows (or curved brackets for discretization), second order tensors are shown in bold, and matrices are shown with square brackets. Assuming the system variables vary harmonically in time with angular frequency ω, the coupled viscoelastic solid and acoustic fluid system can be represented by a system of Helmholtz-type PDEs derived from the conservation of linear momentum, and given respectively by

$$\nabla \cdot \boldsymbol{\sigma}(\vec{x},\omega) + \omega^2 \rho_s(\vec{x}) \vec{u}\left(\vec{x},\omega\right) = \vec{0} \quad \text{on } \Omega \tag{2}$$

and

$$\nabla^2 p(\vec{x},\omega) + \frac{\rho_f\left(\vec{x}\right)\omega^2}{B_f\left(\vec{x}\right)} p(\vec{x},\omega) = 0 \quad \text{on } \Phi\,. \tag{3}$$

$\vec{x}$ is the spatial position vector, $\boldsymbol{\sigma}(\vec{x},\omega)$ is the solid stress tensor, $\rho_s(\vec{x})$ and $\rho_f(\vec{x})$ are the mass densities of the solid and fluid, respectively, $\vec{u}(\vec{x},\omega)$ is the solid displacement vector, $p(\vec{x},\omega)$ is the scalar acoustic fluid pressure in excess of hydrostatic pressure, $B_f\left(\vec{x}\right)$ is the bulk modulus of the fluid, Ω is the solid domain, and Φ is the fluid domain. The boundary conditions for the system considered are given by

$$\boldsymbol{\sigma}(\vec{x},\omega)\vec{n}_s(\vec{x}) = \vec{T}(\vec{x},\omega) \quad \text{on } \Gamma_T\,, \tag{4}$$

$$\vec{u}(\vec{x},\omega) = \vec{u}^o(\vec{x},\omega) \quad \text{on } \Gamma_u\,, \tag{5}$$

and

$$\frac{\partial p(\vec{x},\omega)}{\partial \vec{n}_f(\vec{x})} = -f\left(i\omega\sqrt{\frac{\rho_f(\vec{x})}{B_f(\vec{x})}}p(\vec{x},\omega) + \beta p(\vec{x},\omega)\right) \quad \text{on } \Psi_R . \tag{6}$$

$\vec{T}(\vec{x},\omega)$ is the applied traction vector, Γ_T is the portion of the solid boundary where external traction is specified, $\vec{u}^o(\vec{x},\omega)$ is the prescribed displacement vector, Γ_u is the portion of the solid boundary where the displacement is specified, $\vec{n}_s(\vec{x})$ and $\vec{n}_f(\vec{x})$ are the unit outward vector normals to the solid and fluid surfaces, respectively, f and β are the geometry-specific parameters for improved non-reflecting radiation conditions [1], and Ψ_R is the portion of the fluid boundary where the radiation condition is specified. The prescribed traction will be used to excite the solid, in lieu of modeling the radiation force of ultrasound, and Equation (6) represents the Sommerfeld radiation (non-reflecting) boundary condition to approximate a semi-infinite fluid domain.

The solid and acoustic fluid are coupled through the continuity of the solid and fluid particle displacements and the equivalence of acoustic pressure with solid stress along the interface surfaces. In other words, the acoustic fluid pressure at the fluid-structure interface translates to an applied traction on the surface of the solid, and the solid particle accelerations at the interface translate to the normal derivative of pressure on the surface of the fluid. These coupling conditions can be shown as

$$\boldsymbol{\sigma}(\vec{x},\omega)\vec{n}_s(\vec{x}) = -p(\vec{x},\omega)\vec{n}_s(\vec{x}) \quad \text{on } \Gamma_{fs} \tag{7}$$

and

$$\frac{\partial p(\vec{x},\omega)}{\partial \vec{n}_f(\vec{x})} = \rho_f(\vec{x})\omega^2\vec{u}(\vec{x},\omega)\cdot\vec{n}_f(\vec{x}) \quad \text{on } \Gamma_{fs} . \tag{8}$$

Γ_{fs} is the fluid-structure interface portion of the domain boundaries.

For simplicity, the solids were considered to be isotropic for this proof of concept, which is contrary to most biological tissues. However, the following methodologies can be clearly and easily extended to anisotropic media. As such, the solid

constitutive model was defined by a rate dependent (complex valued) Young's modulus, $E^*(\vec{x},\omega)$, and a Poisson's ratio, $\nu(\vec{x})$. The complex Young's modulus was assumed to be defined by a version of the standard linear solid rheological model consisting of a spring in parallel with a Maxwell model [14], and shown as

$$E^*(\vec{x},\omega) = E_\infty(\vec{x}) + \frac{\widehat{E}(\vec{x})\omega^2\tau(\vec{x})^2}{1+\omega^2\tau(\vec{x})^2} + i\frac{\widehat{E}(\vec{x})\omega\tau(\vec{x})}{1+\omega^2\tau(\vec{x})^2}. \tag{9}$$

$E_\infty(\vec{x})$ is the long-term Young's modulus, $\widehat{E}(\vec{x})$ is the viscous Young's modulus, and $\tau(\vec{x})$ is the relaxation time. The stress-strain relationship for the solid can then be shown in terms of the shear and volumetric components as

$$\boldsymbol{\sigma}(\vec{x},\omega) = 2G^*(\vec{x},\omega)\boldsymbol{\varepsilon}_d(\vec{x},\omega) + K^*(\vec{x},\omega)Tr\left[\boldsymbol{\varepsilon}(\vec{x},\omega)\right]\mathbf{I}, \tag{10}$$

where

$$G^*(\vec{x},\omega) = \frac{E^*(\vec{x},\omega)}{2(1+\nu(\vec{x}))}, \tag{11}$$

$$K^*(\vec{x},\omega) = \frac{E^*(\vec{x},\omega)}{3(1-2\nu(\vec{x}))}, \tag{12}$$

and

$$\boldsymbol{\varepsilon}_d(x,\omega) = \boldsymbol{\varepsilon}(x,\omega) - \frac{1}{3}Tr\left[\boldsymbol{\varepsilon}(x,\omega)\right]\mathbf{I}. \tag{13}$$

$\boldsymbol{\varepsilon}(\vec{x},\omega)$ is the strain tensor, $G^*(\vec{x},\omega)$ is the viscoelastic shear modulus, $K^*(\vec{x},\omega)$ is the viscoelastic bulk modulus $\boldsymbol{\varepsilon}_d(\vec{x},\omega)$ is the deviatoric strain tensor, $Tr[\ ]$ is the trace operator, and $\mathbf{I}$ is the identity tensor. Again for simplicity, the typical small strain definition was used to relate the strains to the displacements as

$$\boldsymbol{\varepsilon}(\vec{x},\omega) = \frac{1}{2}\left[\nabla\vec{u}(\vec{x},\omega) + \left(\nabla\vec{u}(\vec{x},\omega)\right)^T\right]. \tag{14}$$

Typical biological systems are subject to large strains under normal conditions. However, the vibroacoustic testing methods produce small strain perturbations to the

system. Therefore, the testing, modeling, and the characterization performed can be considered to define a linear perturbation to the nonlinear state of the system.

3.4.2 Finite Element Formulation

The Galerkin weak-form finite element method (FEM) was applied to solve the coupled system of PDEs shown above [34]. Taking the inner product of each PDE with a virtual field which satisfies homogeneous essential boundary conditions, integrating over the corresponding domains, applying the divergence theorem where possible, and substituting the natural boundary conditions produces the weak forms for the solid and acoustic PDEs, which are given respectively by

$$\begin{aligned} &\int_{\Omega} \nabla \delta \vec{u}\left(\vec{x}\right) : \boldsymbol{\sigma}\left(\vec{x},\omega\right) dV - \int_{\Omega} \omega^2 \rho_s\left(\vec{x}\right) \delta \vec{u}\left(\vec{x}\right) \cdot \vec{u}\left(\vec{x},\omega\right) dV + \cdots \\ &\cdots - \int_{\Gamma_T} \delta \vec{u}\left(\vec{x}\right) \cdot \vec{T}\left(\vec{x},\omega\right) dS + \int_{\Gamma_{fs}} \delta \vec{u}\left(\vec{x}\right) \cdot \vec{n}_s\left(\vec{x}\right) p\left(\vec{x},\omega\right) dS = 0 \end{aligned} \tag{15}$$

and

$$\begin{aligned} &\int_{\Phi} \nabla \delta p\left(\vec{x}\right) \cdot \nabla p\left(\vec{x},\omega\right) dV - \int_{\Phi} \omega^2 \delta p\left(\vec{x}\right) \frac{\rho_f\left(\vec{x}\right)}{B_f\left(\vec{x}\right)} p\left(\vec{x},\omega\right) dV + \cdots \\ &\cdots - \int_{\Gamma_{fs}} \omega^2 \delta p\left(\vec{x}\right) \rho_f\left(\vec{x}\right) u\left(\vec{x},\omega\right) \cdot \vec{n}_f\left(\vec{x}\right) dS + \cdots \\ &\cdots + \int_{\Psi_R} i\omega \delta p\left(\vec{x}\right) f \sqrt{\frac{\rho_f\left(\vec{x}\right)}{B_f\left(\vec{x}\right)}} p\left(\vec{x},\omega\right) dS + \int_{\Psi_R} \delta p\left(\vec{x}\right) f \beta p\left(\vec{x},\omega\right) dS = 0 \end{aligned} \tag{16}$$

$\delta \vec{u}\left(\vec{x}\right)$ is the virtual displacement field and $\delta p\left(\vec{x}\right)$ is the virtual pressure field. To obtain an algebraic system of equations, the domain is divided into finite elements and the fields are approximated within each element as

$$\vec{u}\left(\vec{x},\omega\right) \approx \left[N\left(\vec{x}\right)\right]\left\{u^e\left(\omega\right)\right\} \tag{17}$$

$$\delta \vec{u}\left(\vec{x}\right) \approx \left[N\left(\vec{x}\right)\right]\left\{\delta u^e\right\} \tag{18}$$

$$p(\vec{x},\omega) \approx \left[H(\vec{x})\right]\left\{p^e(\omega)\right\} \tag{19}$$

$$\delta p(\vec{x}) \approx \left[H(\vec{x})\right]\left\{\delta p^e\right\} \tag{20}$$

$\left\{u^e(\omega)\right\}$, $\left\{\delta u^e\right\}$, $\left\{p^e(\omega)\right\}$, and $\left\{\delta p^e\right\}$ are the vectors of nodal displacements, virtual displacements, pressures, and virtual pressures for a given element, respectively, and $\left[N(\vec{x})\right]$ and $\left[H(\vec{x})\right]$ are the matrices of polynomial interpolating functions (associated in this work with the full-order modeling) for the solid and fluid fields, respectively. Substituting the field approximations into the weak forms of the governing equations, assuming the fluid density to be a constant, and separating real and imaginary terms, the block-structured algebraic system of equations for the full-order model (FOM) of the coupled steady-state acoustic-structure interaction is given by

$$\begin{bmatrix} [A_D] & -[A_{OD}] & -[S] & [0] \\ [A_{OD}] & [A_D] & [0] & -[S] \\ -\omega^2\rho_f[S]^T & [0] & [B_D] & -[B_{OD}] \\ [0] & -\omega^2\rho_f[S]^T & [B_{OD}] & [B_D] \end{bmatrix} \begin{Bmatrix} \Re\{u(\omega)\} \\ \Im\{u(\omega)\} \\ \Re\{p(\omega)\} \\ \Im\{p(\omega)\} \end{Bmatrix} = \begin{Bmatrix} \Re\{R_T(\omega)\} \\ \Im\{R_T(\omega)\} \\ \{0\} \\ \{0\} \end{Bmatrix}, \tag{21}$$

where

$$\begin{aligned} [A_D] = & \sum_{\substack{solid \\ elements}} \int_{\Omega^e} 2\Re\left(G^*(\vec{x},\omega)\right)\left[B(\vec{x})\right]^T[C_g]\left[B(\vec{x})\right]dV + \cdots \\ & \cdots + \sum_{\substack{solid \\ elements}} \int_{\Omega^e} \Re\left(K^*(\vec{x},\omega)\right)\left[B(\vec{x})\right]^T[C_k]\left[B(\vec{x})\right]dV + \cdots \\ & \cdots - \sum_{\substack{solid \\ elements}} \omega^2 \int_{\Omega^e} \rho_s(\vec{x})\left[N(\vec{x})\right]^T\left[N(\vec{x})\right]dV \end{aligned} , \tag{22}$$

$$\begin{aligned} [A_{OD}] = & \sum_{\substack{solid \\ elements}} \int_{\Omega^e} 2\Im\left(G^*(\vec{x},\omega)\right)\left[B(\vec{x})\right]^T[C_g]\left[B(\vec{x})\right]dV + \cdots \\ & \cdots + \sum_{\substack{solid \\ elements}} \int_{\Omega^e} \Im\left(K^*(\vec{x},\omega)\right)\left[B(\vec{x})\right]^T[C_k]\left[B(\vec{x})\right]dV \end{aligned} , \tag{23}$$

$$\left\{R_T(\omega)\right\} = \sum_{\substack{solid\\elements}} \int_{\Gamma_T^e} \left[N(\vec{x})\right]^T \vec{T}(\vec{x},\omega) dS \tag{24}$$

$$\begin{aligned}\left[B_D\right] = &\sum_{\substack{fluid\\elements}} \left(-\omega^2 \int_{\Phi^e} \frac{\rho_f}{B_f(\vec{x})} \left[H(\vec{x})\right]^T \left[H(\vec{x})\right] dV \right) + \cdots \\ \cdots + &\sum_{\substack{fluid\\elements}} \left(\int_{\Phi^e} \left[F(\vec{x})\right]^T \left[F(\vec{x})\right] dV + \int_{\Psi_R^e} f\beta \left[H(\vec{x})\right]^T \left[H(\vec{x})\right] dS \right)\end{aligned}, \tag{25}$$

$$\left[B_{OD}\right] = \sum_{\substack{fluid\\elements}} \omega \int_{\Psi_R^e} f \sqrt{\frac{\rho_f}{B_f(\vec{x})}} \left[H(\vec{x})\right]^T \left[H(\vec{x})\right] dS\,, \tag{26}$$

and

$$\begin{aligned}\left[S\right] = &\sum_{\substack{solid\\elements}} -\int_{\Gamma_{fs}^e} \left[N(\vec{x})\right]^T \vec{n}_s(\vec{x}) \left[H(\vec{x})\right] dS = \cdots \\ \cdots = &\left(\sum_{\substack{fluid\\elements}} \int_{\Gamma_{fs}^e} \left[H(\vec{x})\right]^T \vec{n}_f(\vec{x})^T \left[N(\vec{x})\right] dS \right)^T\end{aligned} \tag{27}$$

$\Re(\ )$ and $\Im(\ )$ represent the real and imaginary components, respectively, and the summation over elements refers to the traditional FE assembly. $\left[B(\vec{x})\right]$ and $\left[F(\vec{x})\right]$ are the matrices of spatial derivatives of the solid interpolating polynomials based on the interpolation of the strain definition and the fluid interpolating polynomials based on the interpolation of the gradient, respectively, in Voigt (vector) notation [34], such that

$$\left\{\boldsymbol{\varepsilon}(\vec{x},\omega)\right\} \approx \left[B(\vec{x})\right]\left\{u^e(\omega)\right\} \tag{28}$$

and

$$\left\{\nabla p(\vec{x},\omega)\right\} \approx \left[F(\vec{x})\right]\left\{p^e(\omega)\right\}. \tag{29}$$

$\left[C_g\right]$ and $\left[C_k\right]$ are the matrices used to obtain the deviatoric and dilatational components of the strain tensor in Voigt notation, respectively, such that

$$\left\{\boldsymbol{\varepsilon}_d\left(\vec{x},\omega\right)\right\}=\left[C_g\right]\left\{\boldsymbol{\varepsilon}\left(\vec{x},\omega\right)\right\} \tag{30}$$

and

$$\left\{Tr\left[\boldsymbol{\varepsilon}\left(\vec{x},\omega\right)\right]\mathbf{I}\right\}=\left[C_k\right]\left\{\boldsymbol{\varepsilon}\left(\vec{x},\omega\right)\right\}. \tag{31}$$

3.4.3 POD Reduced-Order FEM

POD is used in this work is to create a low-order basis to replace the polynomial interpolating functions in the FEM for the vibroacoustic problem (Equations (17)-(20)), to create a reduced-order model (ROM) which will then be used as the numerical model of the system for the inverse solution strategy (Section 3.3). The POD basis is expected to drastically improve computational efficiency of the FEM while maintaining accuracy, provided sufficient information is provided to the POD algorithm. (See [3] and the references therein for a complete discussion of the POD method).

3.4.3.1 POD Bases

The first step in creating a POD basis is to obtain a set of possible solution fields over the domain of the given problem (solid displacements or acoustic pressure in this case). These fields will be generated through FOM FE analyses as described above, and are referred to as snapshots. The snapshot selection is crucial to the generalization capabilities of the POD basis, and a strategy to create the set of snapshots will be discussed in detail in the next section. The ensemble of n snapshots will be referred to as $\left\{u_k\left(\vec{x}\right)\right\}_{k=1}^{n}\in L_2\left(\Omega\right)$. $L_2\left(\Omega\right)$ is the Hilbert space of square integrable functions endowed with an inner product and norm, which are given respectively by

$$\left(f\left(\vec{x}\right),g\left(\vec{x}\right)\right)=\int_\Omega f\left(\vec{x}\right)g\left(\vec{x}\right)d\vec{x},\quad \forall f\left(\vec{x}\right),g\left(\vec{x}\right)\in L_2\left(\Omega\right) \tag{32}$$

and

$$\left\|f\left(\vec{x}\right)\right\|_{L_2(\Omega)}=\left(f\left(\vec{x}\right),f\left(\vec{x}\right)\right)^{1/2},\quad \forall f\left(\vec{x}\right)\in L_2\left(\Omega\right). \tag{33}$$

The snapshot fields can be the acoustic pressure or any one of the displacement component fields at some selected frequencies, depending on which basis is being built, and the domain Ω would correspond accordingly. The m basis functions to be constructed are referred to as $\{\phi_i(\vec{x})\}_{i=1}^{m} \in L_2(\Omega)$, and they form a subspace $V_m = span\{\phi_i(\vec{x})\}_{i=1}^{m} \subset L_2(\Omega)$. Thus, the field itself, and therefore, each snapshot of the field can be approximated with the POD basis as

$$u_k(\vec{x}) \approx \sum_{i=1}^{m} a_{ki}\phi_i(\vec{x}). \tag{34}$$

The best approximation to a snapshot, $u_k^*(\vec{x})$, for the basis is defined such that

$$\left\|u_k(\vec{x}) - u_k^*(\vec{x})\right\|_{L_2(\Omega)} = \inf\left\|u_k(\vec{x}) - v(\vec{x})\right\|_{L_2(\Omega)}, \quad \forall v(\vec{x}) \in V_m. \tag{35}$$

Furthermore, for an orthogonal basis, the best approximation for a field can be found by the projection of that field onto the basis, which is shown as

$$u_k^*(\vec{x}) = \sum_{i=1}^{m} \frac{\left(\phi_i(\vec{x}), u_k(\vec{x})\right)}{\left\|\phi_i(\vec{x})\right\|_{L_2(\Omega)}^2}\phi_i(\vec{x}). \tag{36}$$

Choosing to define the optimal basis as that which minimizes the average of the $L_2 - norm$ of the difference between each snapshot and the best approximation to the snapshot leads to the following optimization problem

$$\underset{\{\phi_i(\vec{x})\}_{i=1}^{m} \in L_2(\Omega)}{\text{minimize}} \quad \left\langle \left\|u_k(\vec{x}) - u_k^*(\vec{x})\right\|_{L_2(\Omega)}^2 \right\rangle \tag{37}$$

where

$$\langle u_k \rangle = \frac{1}{n}\sum_{k=1}^{n} u_k \tag{38}$$

Through some manipulations, the minimization problem can be converted into a maximization problem shown as

$$\underset{\{\phi_i(\vec{x})\}_{i=1}^{m} \in L_2(\Omega)}{\text{maximize}} \quad \left[\left\langle \left(u_k(\vec{x}), \phi_i(\vec{x})\right)^2 \right\rangle - \lambda\left(\left\|\phi_i(\vec{x})\right\|_{L_2(\Omega)}^2 - 1\right)\right] \tag{39}$$

λ is a Lagrange multiplier to force the basis to have a unit norm. Considering the

maximization with respect to a single basis function and using the necessary condition for extrema of a functional, the optimization problem can be transformed into the following eigenvalue problem

$$\int_{\Omega} \left\langle u_k\left(\vec{x}\right) u_k\left(\vec{\xi}\right) \right\rangle \phi_i\left(\vec{x}\right) d\vec{x} = \lambda \phi_i\left(\vec{\xi}\right) \tag{40}$$

The eigenvalue problem (Equation (40)) can be discretized and solved directly, however to reduce the size of the problem, and therefore the computational expense, the method of snapshots is applied [3]. Taking the inner product of Equation (40) with each snapshot field yields the following $n \times n$ eigenvalue problem

$$\frac{1}{n} \sum_{k=1}^{n} A_{jk} C_k = \lambda C_j \tag{41}$$

where

$$A_{jk} = \int_{\Omega} u_j\left(\vec{x}\right) u_k\left(\vec{x}\right) d\vec{x} \tag{42}$$

After solving the eigenvalue problem, the n orthogonal basis functions are given by

$$\phi_i\left(\vec{x}\right) = \frac{1}{\lambda^i n} \sum_{k=1}^{n} u_k\left(\vec{x}\right) C_k^i \,. \tag{43}$$

The i^{th} eigenvalue, λ^i, can be shown to be a measure of the approximation capabilities of the i^{th} basis function, $\phi_i\left(\vec{x}\right)$. Typically only m basis functions are used for the field approximation, where $m < n$, so that the sum of the eigenvalues of the chosen bases is around 99% of the total sum of the n eigenvalues.

3.4.3.2 POD-FEM Implementation

After obtaining POD bases for the real and imaginary acoustic pressure and the real and imaginary parts of each component of the displacement field, the field approximations can be shown as

$$\Re\left(\vec{u}\left(\vec{x},\omega\right)\right) \approx \left[\Phi^{UR}\left(\vec{x}\right)\right]\left\{a^{UR}\left(\omega\right)\right\}, \tag{44}$$

$$\Im\left(\vec{u}\left(\vec{x},\omega\right)\right) \approx \left[\Phi^{UI}\left(\vec{x}\right)\right]\left\{a^{UI}\left(\omega\right)\right\}, \tag{45}$$

$$\Re\left(p\left(\vec{x},\omega\right)\right)\approx\left[\Phi^{PR}\left(\vec{x}\right)\right]\left\{a^{PR}\left(\omega\right)\right\}, \tag{46}$$

and

$$\Im\left(p\left(\vec{x},\omega\right)\right)\approx\left[\Phi^{PI}\left(\vec{x}\right)\right]\left\{a^{PI}\left(\omega\right)\right\}. \tag{47}$$

$\left[\Phi^{UR}\left(\vec{x}\right)\right]$ and $\left[\Phi^{UI}\left(\vec{x}\right)\right]$ are the $3\times 3m_U$ matrices of POD bases for the real and imaginary components of the displacement, respectively, $\left\{a^{UR}\left(\omega\right)\right\}$ and $\left\{a^{UI}\left(\omega\right)\right\}$ are the $3m_U\times 1$ modal coefficient vectors for the real and imaginary components of the displacement, respectively, $\left[\Phi^{PR}\left(\vec{x}\right)\right]$ and $\left[\Phi^{PI}\left(\vec{x}\right)\right]$ are the $1\times m_P$ matrices of POD bases for the real and imaginary components of the acoustic pressure, respectively, and $\left\{a^{PR}\left(\omega\right)\right\}$ and $\left\{a^{PI}\left(\omega\right)\right\}$ are the $m_P\times 1$ modal coefficient vectors for the real and imaginary components of the acoustic pressure, respectively, where m_U is the number of basis functions chosen for the displacement components and m_P is the number of basis functions chosen for the acoustic pressure.

Since the snapshot fields themselves will be obtained through FE analyses, and are defined in terms of a FE mesh with interpolation functions as shown above, it is clear from Equation (43) that the POD bases can be defined similarly. Therefore, the POD bases can be shown for the displacement and pressure respectively as

$$\phi^{U}\left(\vec{x}\right)=\sum_{i=1}^{n_{Ue}}N_i\left(\vec{x}\right)\phi_i^{Ue} \tag{48}$$

and

$$\phi^{P}\left(\vec{x}\right)=\sum_{i=1}^{n_{Pe}}H_i\left(\vec{x}\right)\phi_i^{Pe}\ . \tag{49}$$

ϕ_i^{Ue} and ϕ_i^{Pe} are the nodal values of a given element for any one of the displacement components and any one of the pressure components, respectively, and n_{Ue} and n_{Pe} are the number of nodes in a solid and a fluid element, respectively.

The field approximations (Equations (44)-(47)) can then be defined in terms of the FE interpolating polynomials (Equations (48) and (49)), and applied to the weak-form

Galerkin method analogously to the procedure shown in Section 3.4.2. The final discretized system of equation for the POD ROM for steady-state acoustic-structure interaction can then be shown as

$$\begin{bmatrix} \left[A^{POD}\right]_{11} & \left[A^{POD}\right]_{12} & \left[A^{POD}\right]_{13} & [0] \\ \left[A^{POD}\right]_{21} & \left[A^{POD}\right]_{22} & [0] & \left[A^{POD}\right]_{24} \\ \left[A^{POD}\right]_{31} & [0] & \left[A^{POD}\right]_{33} & \left[A^{POD}\right]_{34} \\ [0] & \left[A^{POD}\right]_{42} & \left[A^{POD}\right]_{43} & \left[A^{POD}\right]_{44} \end{bmatrix} \begin{Bmatrix} \{a^{UR}(\omega)\} \\ \{a^{UI}(\omega)\} \\ \{a^{PR}(\omega)\} \\ \{a^{PI}(\omega)\} \end{Bmatrix} = \begin{Bmatrix} \{R_T^R(\omega)\} \\ \{R_T^I(\omega)\} \\ \{0\} \\ \{0\} \end{Bmatrix}, \quad (50)$$

where

$$\begin{aligned}
\left[A^{POD}\right]_{11} &= \left[\{\phi^{UR}\}\right]^T \left([A_D]\right)\left[\{\phi^{UR}\}\right] \\
\left[A^{POD}\right]_{12} &= \left[\{\phi^{UR}\}\right]^T \left(-[A_{OD}]\right)\left[\{\phi^{UI}\}\right] \\
\left[A^{POD}\right]_{13} &= \left[\{\phi^{UR}\}\right]^T \left(-[S]\right)\left[\{\phi^{PR}\}\right] \\
\left[A^{POD}\right]_{21} &= \left[\{\phi^{UI}\}\right]^T \left([A_{OD}]\right)\left[\{\phi^{UR}\}\right] \\
\left[A^{POD}\right]_{22} &= \left[\{\phi^{UI}\}\right]^T \left([A_D]\right)\left[\{\phi^{UI}\}\right] \\
\left[A^{POD}\right]_{24} &= \left[\{\phi^{UI}\}\right]^T \left(-[S]\right)\left[\{\phi^{PI}\}\right] \\
\left[A^{POD}\right]_{31} &= \left[\{\phi^{PR}\}\right]^T \left(-\omega^2 \rho_f [S]^T\right)\left[\{\phi^{UR}\}\right] \\
\left[A^{POD}\right]_{33} &= \left[\{\phi^{PR}\}\right]^T \left([B_D]\right)\left[\{\phi^{PR}\}\right] \\
\left[A^{POD}\right]_{34} &= \left[\{\phi^{PR}\}\right]^T \left([-B_{OD}]\right)\left[\{\phi^{PI}\}\right] \\
\left[A^{POD}\right]_{42} &= \left[\{\phi^{PI}\}\right]^T \left(-\omega^2 \rho_f [S]^T\right)\left[\{\phi^{UI}\}\right] \\
\left[A^{POD}\right]_{43} &= \left[\{\phi^{PI}\}\right]^T \left([B_{OD}]\right)\left[\{\phi^{PR}\}\right] \\
\left[A^{POD}\right]_{44} &= \left[\{\phi^{PI}\}\right]^T \left([B_D]\right)\left[\{\phi^{PI}\}\right] \quad . \quad (51) \\
\{R_T^R(\omega)\} &= \left[\{\phi^{UR}\}\right]^T \left(\Re\{R_T(\omega)\}\right) \\
\{R_T^I(\omega)\} &= \left[\{\phi^{UI}\}\right]^T \left(\Im\{R_T(\omega)\}\right)
\end{aligned}$$

$\left[\left\{\phi^{UR}\right\}\right]$ and $\left[\left\{\phi^{UI}\right\}\right]$ are the $3n_U \times 3m_U$ matrices containing the FE nodal values of the real and imaginary displacement POD bases, respectively, $\left[\left\{\phi^{PR}\right\}\right]$ and $\left[\left\{\phi^{PI}\right\}\right]$ are the $n_P \times m_P$ matrices containing the FE nodal values of the real and imaginary pressure POD bases, respectively, and n_U and n_P are the total number of nodes in the solid mesh and the fluid mesh, respectively. Therefore, after reduction, the ROM system to be solved consists of a $\left(6m_U + 2m_P\right)\times\left(6m_U + 2m_P\right)$ dense matrix, leading to a substantial reduction in computational cost compared to the $\left(6n_U + 2n_P\right)\times\left(6n_U + 2n_P\right)$ sparse matrix for the FOM, where n_U and n_P are the total number of nodes in the solid and fluid FE meshes, respectively.

Through this procedure, the assembly process for the ROM remains essentially unchanged from the typical full-order FEM, the only difference being the additional matrix multiplications by the basis nodal values. Therefore, the computational implementation using this method is extremely straight-forward and efficient.

3.5 POD Snapshot Generation for Viscoelastic Material Generalization

A FE FOM for a given system can be represented in a general way as an operator $F : X \to V$, which maps a metric space of some input model parameters X to a metric space of solution fields V. As such, the snapshot fields used to create a POD ROM can be defined as a subset of the space of solution fields $V_n \subset V$, which are generated by a subset of the space of input parameters $X_n \subset X$, such that $F : X_n \to V_n$. The POD ROM can then be represented as an operator that also maps the input parameters to the solution fields, but one which is a function of the snapshots as $\widehat{F}\left(V_n\right) : X \to V$. Therefore, the main challenge in developing a POD ROM is selecting the subset of input parameters used to generate the snapshots, such that for $F : x \to y_1$ and $\widehat{F}\left(V_n\right) : x \to y_2,\ \forall\ x \in X$ and $y_1, y_2 \in Y$, the resulting difference between the solution fields $\left\|y_1 - y_2\right\|$ will be minimal.

The entire foundation of the POD method is that the basis will be optimal in an average sense for representing the snapshot fields provided. Therefore, it is necessary for the snapshots to be indicative of the nature of solutions which can be expected for a given boundary value problem, in order for the basis to be able to generalize over all possible solutions (i.e. solutions outside of the set of snapshots). Furthermore, when using these ROMs for inverse characterization it is crucial to have a broad range of generalization in order to accurately assess the observability of the problem, and then ultimately identify a solution.

For the inverse problems considered here, the sampling frequencies, the geometry, the boundary conditions, and some of the material properties will be assumed to be known *a priori*, and therefore fixed for the numerical analyses. In addition, the spatial variation of the material parameters, in the form of discrete regions of homogeneity, will be assumed to be known. In many applications an imaging methodology can be applied to obtain a qualitative distribution of parameters prior to the quantitative inverse characterization. The only unknowns are the parameters defining the rate dependent viscoelastic behavior of the solid. Therefore, the snapshot fields will be generated by varying these viscoelastic parameters.

The general principles of maximum entropy [21] indicate that if no information is available *a priori* about the variable distribution, then a uniform distribution is the optimal choice. Furthermore, the work by Joyner [22] showed for a damage identification inverse problem that creating the POD snapshots by uniformly varying the damage parameters lead to as good, and many times better, inverse identification capabilities than a random sampling. However, there are typically far too many parameters defining viscoelastic material models to afford uniform sampling of each parameter, particularly for heterogeneous structures. Also, the sensitivity of the solution fields to the parameters shown in Section 3.4.1 for the standard linear solid

viscoelastic model, and those of many other commonly used constitutive models which have similarly nonphysical parameters, is highly nonlinear. Therefore, a uniform distribution of these parameters will in most cases lead to a strongly biased set of snapshot fields. The sampling method proposed here for viscoelastic material models builds from this notion of uniform sampling being optimal. However, the sampling is applied to the physically meaningful characteristics of the viscoelastic model, rather than the parameter values.

It is well known that rheological models for viscoelasticity are highly non-unique, in that different parameter values, or even different rheological models, can produce the same mechanical behavior for a given time or frequency range. Alternatively, the mechanical behavior can be defined uniquely by, and is significantly more sensitive to, characteristics which are directly related to the energy storage and dissipation of the material. Two such characteristics are the mechanical loss, which is associated with viscous damping, and the equivalent elasticity. The mechanical loss corresponds to the tangent of the phase angle of the complex modulus, and is given for the standard linear solid shown in Equation (9) by

$$\tan\left[\delta(\omega)\right] = \left[\hat{E}\left(\frac{\omega\tau}{1+\omega^2\tau^2}\right)\right] \Big/ \left[E_\infty + \hat{E}\left(\frac{\omega^2\tau^2}{1+\omega^2\tau^2}\right)\right]. \tag{52}$$

The equivalent elasticity corresponds to the magnitude of the complex modulus, and is given for the standard linear solid shown above by

$$E^{eq}(\omega) = \left\{\left[\hat{E}\left(\frac{\omega\tau}{1+\omega^2\tau^2}\right)\right]^2 + \left[E_\infty + \hat{E}\left(\frac{\omega^2\tau^2}{1+\omega^2\tau^2}\right)\right]^2\right\}^{1/2}. \tag{53}$$

Therefore, in the proposed sampling method, parameters will be identified to maximize the diversity of the material characteristics (i.e. $\tan\left[\delta(\omega)\right]$ and $E^{eq}(\omega)$) for each region of homogeneity over the frequency range considered. In other words, parameters will be sought which produce mechanical loss functions and equivalent

elasticity functions which are as close as possible to uniformly spaced within the material search ranges.

This problem to maximize the diversity of the characteristic functions can be shown as the following minimization problem

$$\underset{\vec{\alpha}\in\mathbb{R}^{3n}}{\text{minimize}}\left\{\begin{array}{l}\left\|\dfrac{S_n^{\delta}\left(\vec{\alpha},\omega\right)-U_n\left[\tan\left(\delta\right)_{\min},\tan\left(\delta\right)_{\max}\right]}{U_n\left[\tan\left(\delta\right)_{\min},\tan\left(\delta\right)_{\max}\right]}\right\|_{l_2(n,\omega)}+\cdots \\ \cdots+\left\|\dfrac{S_n^{E}\left(\vec{\alpha},\omega\right)-U_n\left[E_{\min}^{eq},E_{\max}^{eq}\right]}{U_n\left[E_{\min}^{eq},E_{\max}^{eq}\right]}\right\|_{l_2(n,\omega)}\end{array}\right\}. \tag{54}$$

$\vec{\alpha}$ is the vector of material parameters for the snapshots (i.e. $\left\{E_{\infty}^{1},\widehat{E}^{1},\tau^{1},\ldots,E_{\infty}^{n},\widehat{E}^{n},\tau^{n}\right\}$), $S_n^{\delta}\left(\vec{\alpha},\omega\right)$ is the n^{th} component of the sorted (by magnitude) vector of the $\tan\left[\delta\left(\omega\right)\right]$ values for each snapshot at a given frequency, $S_n^{E}\left(\vec{\alpha},\omega\right)$ is the n^{th} component of the sorted vector of the $E^{eq}\left(\omega\right)$ values for each snapshot at a given frequency, $U_n\left[\min,\max\right]$ is the n^{th} component of the sorted vector of uniformly spaced values between $\min$ and $\max$, and $\|\ \|_{l_2(n,\omega)}$ is the discrete l_2-norm (SRSS) over the snapshots and sampling frequencies. Therefore, to obtain a set of snapshot fields, it becomes necessary to solve a nonlinear optimization problem. Fortunately, the objective function (Equation (54)) is inexpensive to evaluate, and a stochastic global search algorithm such as a genetic algorithm [16, 29], which was used in this work, can be applied to solve the optimization problem. As such the methodology can be robustly and efficiently applied to a wide variety of viscoelastic representations to obtain a diverse set of snapshots.

3.6 Examples and Discussion

Three computational examples were considered to show the validity of using the proposed methodology. In the first example the capabilities of the POD bases to approximate a plane wave solution for a viscoelastic medium was analyzed. This first example was intended to explore the robustness and effectiveness of the proposed methodology for material sampling to produce POD bases for ROMs which are capable of accurately representing a wide range of material properties, with a minimal number of FOM analyses. The next two examples consisted of simulated inverse problems of the characterization of viscoelastic parameters of a homogeneous solid and a two-material discretely heterogeneous solid, respectively, through vibroacoustic testing methods. In most cases soft tissue can be considered nearly incompressible and the density is known to be approximately the same as water. Therefore, for the inverse problems considered, the density and Poisson's ratio of the solids were assumed to be known *a priori,* in addition to the surrounding fluid properties. Furthermore, the intention of this proof of concept is not to display the well known computational benefits of POD reduced-order modeling, but rather, to show an approach to maximize the capabilities of such reduced-order modeling to be used for inverse viscoelastic characterization. As such, to alleviate the computational expense of the forward modeling, the material properties used for the simulated experiments were considerably stiffer than those typical of healthy soft tissues. However, the relative search ranges for the material properties (i.e. the required generalization ranges of the POD ROMs) and the frequency ranges considered were on par with those expected in biological applications.

3.6.1 Shear Plane Wave POD Best Approximation

A two-dimensional homogeneous $1m \times 1m$ square domain was considered, with the

displacement field defined by a shear plane wave of unit magnitude traveling through the medium, which is given by

$$\vec{u}\left(\vec{x},\omega\right)=\begin{Bmatrix}-\sin\left(\theta\right)\\ \cos\left(\theta\right)\end{Bmatrix}\exp\left[ik\left\{\cos\left(\theta\right)x_1+\sin\left(\theta\right)x_2\right\}\right]. \tag{55}$$

θ is the direction of the wave propagation, which was chosen arbitrarily for this example to be $\pi/3$, and k is the wave number, which is given for the isotropic viscoelastic medium described in Section 3.4.1 by

$$k=\omega\sqrt{\frac{\rho_s}{G^*}}. \tag{56}$$

Nine discrete frequency samples were considered between $1Hz$ and $5Hz$ at $0.5Hz$ increments.

In order to quantify the approximation capabilities of the POD bases it is sufficient to analyze the best approximation (Equation (36)) of the bases to the known solution, as the error of the Galerkin FEM is bounded with respect to this error. Therefore, the methodology described to maximize the snapshot diversity was applied to generate POD bases for a given number of snapshots between one and five, and the continuous L_2-norm of the difference between the best approximation for the POD bases and the actual solution (i.e. continuous $L_2-error$) for 100 random material realizations was calculated. For comparison purposes, POD bases were also generated by choosing random material parameters ($G_\infty,\widehat{G},\tau$) from uniform distributions, and the corresponding $L_2-error$ was calculated for the 100 test realizations.

Table 3.1 shows the minimum and maximum values for the material characteristics used to generate the snapshots which maximize the diversity, as well as the minimum and maximum values for the material parameters used to generate the random snapshots. An important note is that an additional challenge when sampling the parameters directly is that the given ranges constitute a significantly larger

distribution of material behaviors than when sampling the characteristics. However, this is required when sampling the parameters to avoid biasing the data, and to ensure the parameters will cover the entire space of the material characteristics. In all cases, the maximum number of modes was used for the approximations to avoid any inconsistency.

Table 3.1. Ranges for the parameters used to generate the maximum diversity snapshots and the random snapshots for Example 1.

Parameter	Minimum	Maximum
G^{eq}	**1.0Pa**	**100.0Pa**
$\tan(\delta)$	**0.01**	**1.0**
G_{∞}	**1.0Pa**	**100.0Pa**
$\widehat{G}$	**1.0Pa**	**100.0Pa**
τ	**0.01s**	**1.0s**

Figure 3.1 shows the mean and standard deviation of the average relative $L_2 - error$ for the 100 test material realizations versus the number of material samples for five trials of the proposed maximum diversity sampling methodology compared to the random parameter sampling. Clearly for very few material samples, the maximum diversity method is capable of very accurately generalizing over the material search space. With only two material samples, the maximum diversity method has better generalization than even the five samples for the random sampling. With only three material samples, the maximum diversity method appears to reach the optimal approximation capabilities for the given problem. In addition, the maximum diversity method is shown to be very robust, in that over each of the five trials the approximation capabilities remain accurate and consistent, particularly compared to

the random sampling method which displays greater scatter.

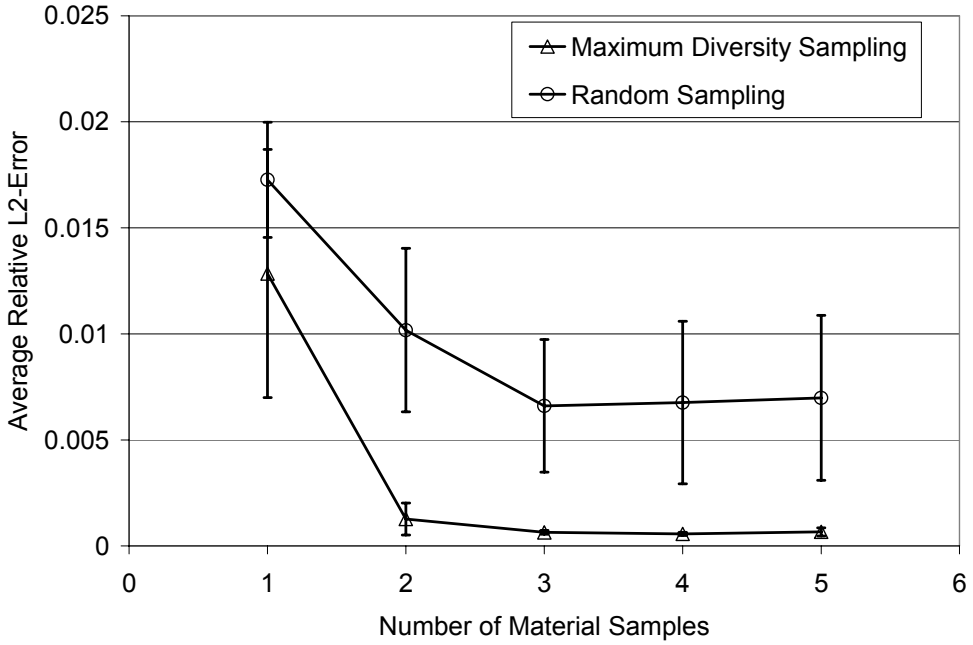

Figure 3.1. Mean and standard deviation (error bars) of the average $L_2 - error$ for the maximum diversity sampling methodology and the random parameter sampling for Example 1.

3.6.2 Inverse Characterization of a Cylinder in Water

The first inverse problem consisted of a simulated experiment of a $15mm$ diameter viscoelastic cylinder immersed in water with a harmonic pressure line applied to the surface of the cylinder, as shown in Figure 3.2. The frequency response of the system was obtained through the full-order plane strain FEM for a range of frequencies between $30kHz$ and $65kHz$, and the steady-state acoustic pressure response was measured at a single point in the water. To add realism to the experiment and relieve the inverse crime inherent in simulated experiments, a different mesh was used for the FOM to generate the experiment (an alternative to adding random noise) than was used for the FOM to generate the POD snapshots. Figure 3.3 shows the frequency

response of the normalized acoustic pressure at the chosen measurement location, and the 11 frequency points which were sampled and used to solve the inverse problem through the methodology described in Section 3.3. Note that the computational expense of the numerical simulations increases with each additional frequency for which the model will be evaluated. Therefore, the minimum number of frequencies were chosen which sufficiently define the shape of the measured frequency response.

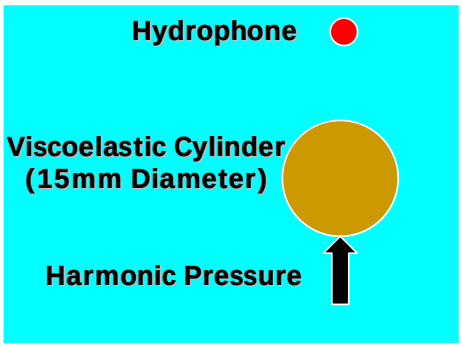

Figure 3.2. Schematic of Example 2.

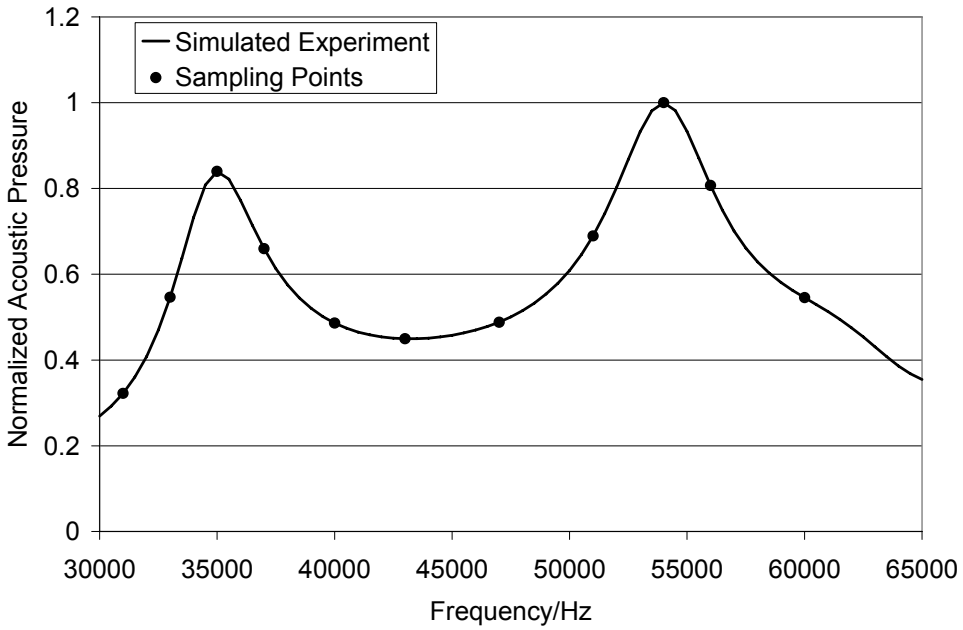

Figure 3.3. Frequency response of normalized acoustic pressure and discrete sampling points used for the inverse problem for Example 2.

The cylinder had a Poisson's ratio of 0.25, the density of the solid and the water were both taken as $1000\,kg/m^3$, and the bulk modulus of the water was taken to be $2.2\ GPa$. Table 3.2 shows the values of the viscoelastic moduli used to simulate the experiment and the search ranges considered for the optimization solution strategy for the inverse characterization problem.

Table 3.2. Experimental material properties and optimization search ranges for Example 2.

Optimization Parameter	Experimental Value	Optimization Minimum	Optimization Maximum
E_∞	**3.0GPa**	**0.1GPa**	**10.0GPa**
$\hat{E}$	**0.375GPa**	**0.1GPa**	**10.0GPa**
τ	**$1.0\text{x}10^{-6}$s**	**$1.0\text{x}10^{-7}$s**	**$1.0\text{x}10^{-5}$s**

Based on the results from the previous example, three material realizations for the POD snapshots were deemed sufficient for creating ROMs with generalization capabilities to be used in the inverse solution strategy (Section 3.3). The minimum and maximum values for creating the snapshots to maximize diversity were $0.1GPa$ and $10GPa$ for the equivalent elasticity, and 0.01 and 1.0 for the mechanical loss. All 11 of the sampling frequencies were used to generate the snapshots, therefore, producing a total of 33 POD bases. Through preliminary tests it was found for the search range considered that nearly all of the POD bases were required in the ROMs for accurate generalization. As such, 31 bases were used for all solid and acoustic components in the ROMs for the solution process.

Due to the stochastic nature of both the generation of the material realizations for the snapshots and the optimization solution strategy, the process of creating the ROM and then solving the inverse problem was repeated five times to quantify the accuracy

and consistency of the methodology. Furthermore, since the viscoelastic parameters themselves are non-unique representations of the material behavior, the quality of the solutions will be displayed directly through the material characteristics (i.e. the equivalent elasticity and the mechanical loss).

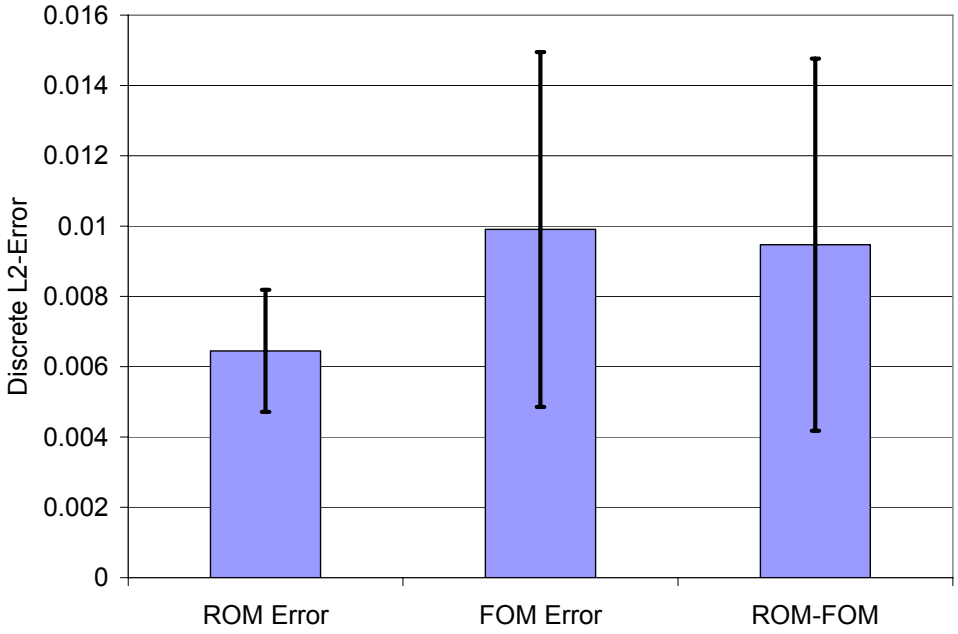

Figure 3.4. Mean and standard deviation (error bars) of the discrete $L_2-error$ of the pressure responses from the inverse solutions with the ROM and the FOM, and the discrete L_2-norm of the difference between the pressure responses of the ROM and FOM for Example 2.

Figure 3.4 shows the mean and standard deviation of the discrete $L_2-error$ of the experimental pressure response compared to the ROM response with the inverse characterization solutions (i.e. Equation (1)), the discrete $L_2-error$ of the experimental pressure response compared to the FOM response with the inverse characterization solutions, and the discrete L_2-norm of the difference between the ROM responses and the FOM responses with the inverse characterization solutions for the five trials of the inverse problem. As expected, since the inverse solution strategy was capable of sufficiently minimizing the error between the experimental response

and the ROM response, the error between the FOM response and the experimental response was of the same order as the difference between the ROM response and the FOM response. Therefore, the generalization capabilities of the ROMs led to inverse solutions which were likely to be as accurate, or nearly as accurate, as those which could have been obtained using the FOM in the solution procedure (Equation (1)).

Figure 3.5 shows the mean and standard deviation of the equivalent elasticity for the solution parameter sets, and Figure 3.6 shows the mean and standard deviation of the mechanical loss for the solution parameter sets. In accordance with the results shown in [11], the low amount of damping in the experimental specimen resulted in a relatively low sensitivity of the results to the mechanical loss. Therefore, the solutions for the equivalent elasticity were more accurate than for the mechanical loss. However, this further goes to demonstrate the generalization capabilities of the POD ROM, in that it was able to identify the range of parameter values which satisfied the given experiment.

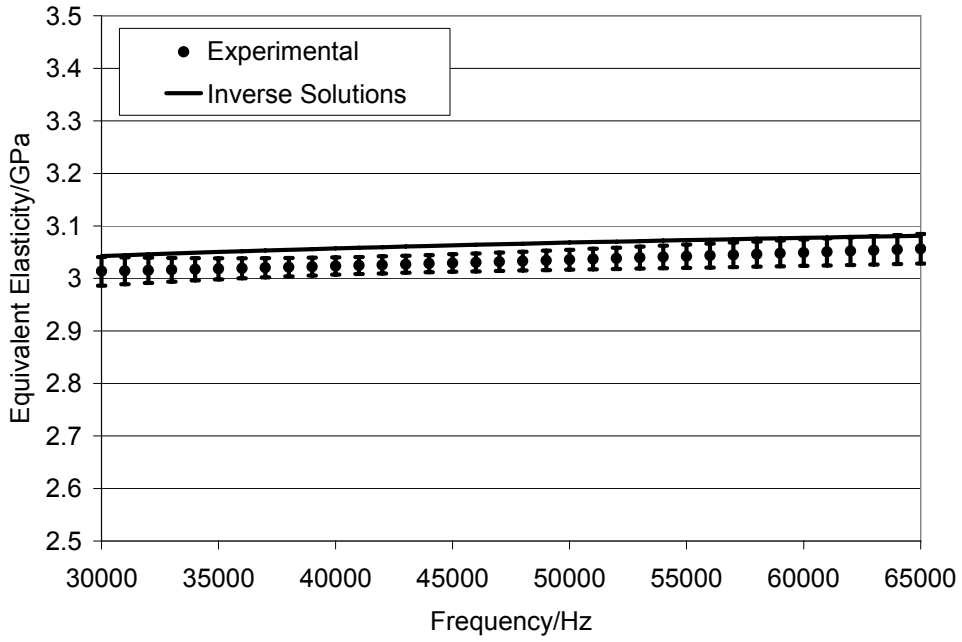

Figure 3.5. Mean and standard deviation (error bars) of the equivalent elasticity for the inverse solutions compared to the experimental value for Example 2.

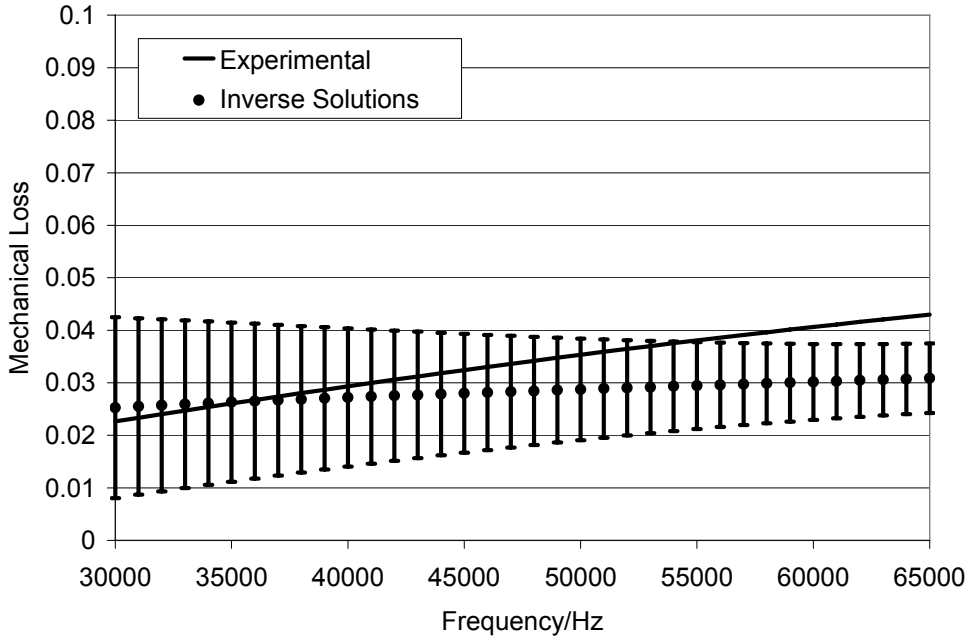

Figure 3.6. Mean and standard deviation (error bars) of the mechanical loss for the inverse solutions compared to the experimental value for Example 2.

3.6.3 Inverse Characterization of a Cylinder with a Hard Sphere Inclusion

To explore the capabilities of the proposed methodology for a heterogeneous solid, the second inverse problem consisted of a $45mm$ diameter $75mm$ long cylinder immersed in water with a $15mm$ diameter spherical hard inclusion, as shown in Figure 3.7. The inclusion was centered along the axis of the cylinder and a harmonic pressure was applied to the surface of the inclusion in the direction of the axis of the cylinder to maintain axisymmetry. The frequency response of the system was obtained through the full-order axisymmetric FEM for a range of frequencies between $20kHz$ and $60kHz$. Similarly to the previous example, the steady-state acoustic pressure response was measured at a single point in the water and normalized. Again, a different mesh was used for the FOM to generate the experiment than was used for the FOM to generate the POD snapshots. Figure 3.8 shows the frequency response of the

normalized acoustic pressure at the chosen measurement location, and the 14 frequency points which were sampled and used to solve the inverse problem.

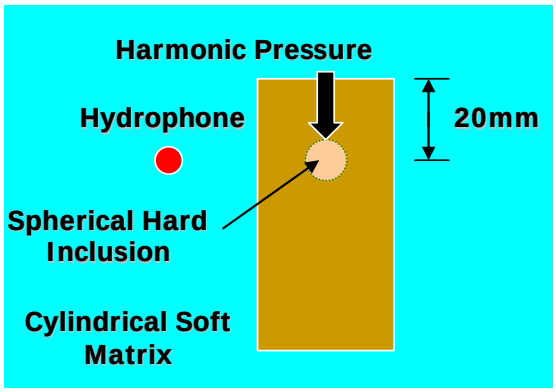

Figure 3.7. Schematic of Example 3.

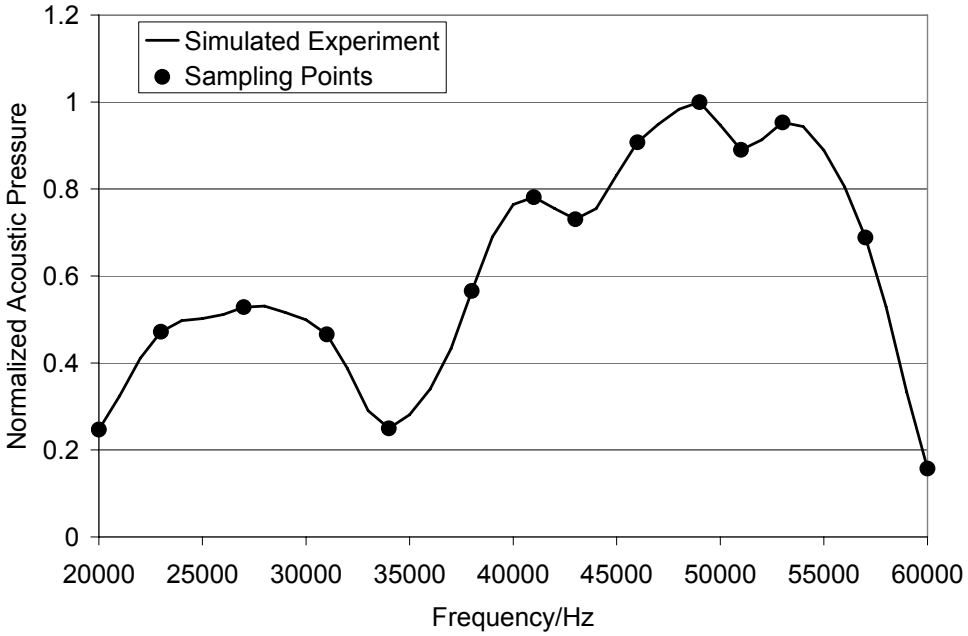

Figure 3.8. Frequency response of normalized acoustic pressure and discrete sampling points used for the inverse problem for Example 3.

The cylinder and the inclusion both had Poisson's ratios of 0.48, all densities were taken as $1000\,kg/m^3$, and the bulk modulus of the water was again taken to be

2.2 *GPa*. Table 3.3 shows the values of the viscoelastic moduli for the cylinder, i.e. solid matrix, (E_∞^m, $\widehat{E}^m$, and τ^m) and the inclusion (E_∞^i, $\widehat{E}^i$, and τ^i) used to simulate the experiment and the search ranges considered for the optimization inverse solution strategy. An important note is that it was not assumed *a priori* that the inclusion would be harder than the surrounding matrix and the search ranges for the two materials were identical to keep the prospective applicability of the example broad.

Table 3.3. Experimental material properties and optimization search ranges for Example 3.

Optimization Parameter	Experimental Value	Optimization Minimum	Optimization Maximum
E_∞^m	**0.6GPa**	**0.5GPa**	**5.0GPa**
$\widehat{E}^m$	**0.4GPa**	**0.1GPa**	**1.0GPa**
τ^m	**$1.0\text{x}10^{-5}$s**	**$5.0\text{x}10^{-7}$**	**$5.0\text{x}10^{-5}$**
E_∞^i	**3.0GPa**	**0.5GPa**	**5.0GPa**
$\widehat{E}^i$	**0.375GPa**	**0.1GPa**	**1.0GPa**
τ^i	**$1.0\text{x}10^{-6}$s**	**$5.0\text{x}10^{-7}$s**	**$5.0\text{x}10^{-5}$s**

Again, three material realizations were chosen to create the POD snapshots for the ROMs used in the inverse solution strategy. However, to account for the discrete heterogeneity without bias, all nine combinations of the three material realizations for the matrix and the inclusion were applied. Because of the increased difficulty due to the heterogeneity, a slightly smaller search space was considered for this problem. The minimum and maximum values for creating the snapshots to maximize diversity were $0.5GPa$ and $5GPa$ for the equivalent elasticity, and 0.01 and 0.5 for the mechanical loss. All 14 of the sampling frequencies were used to generate the

snapshots, producing a total of 126 POD bases. Similarly to the previous example, nearly all of the POD bases were required for accurate generalization, and therefore, 125 bases were used for all solid and acoustic components in the ROMs for the solution process. Once again the inverse solution process was repeated five times to test consistency.

Figure 3.9 shows the mean and standard deviation of the discrete $L_2 - error$ of the experimental pressure response compared to the ROM response with the inverse characterization solutions, the discrete $L_2 - error$ of the experimental pressure response compared to the FOM response with the inverse characterization solutions, and the discrete $L_2 - norm$ of the difference between the ROM responses and the FOM responses with the inverse characterization solutions for the five trials of the inverse problem. Clearly this example was a more challenging inverse problem than the previous example, as the solution errors were larger. This is partially due to the fact that the added noise in the simulated experiment from the FOM mesh differences was greater for this example. Also, based on these results and additional numerical analyses, the sensitivity of the acoustic pressure at the measurement point was lower for this example. However, the difference between the ROM responses and the FOM responses was as low as in the previous example, demonstrating that the ROM again served as an adequate replacement to the FOM in the inverse solution strategy.

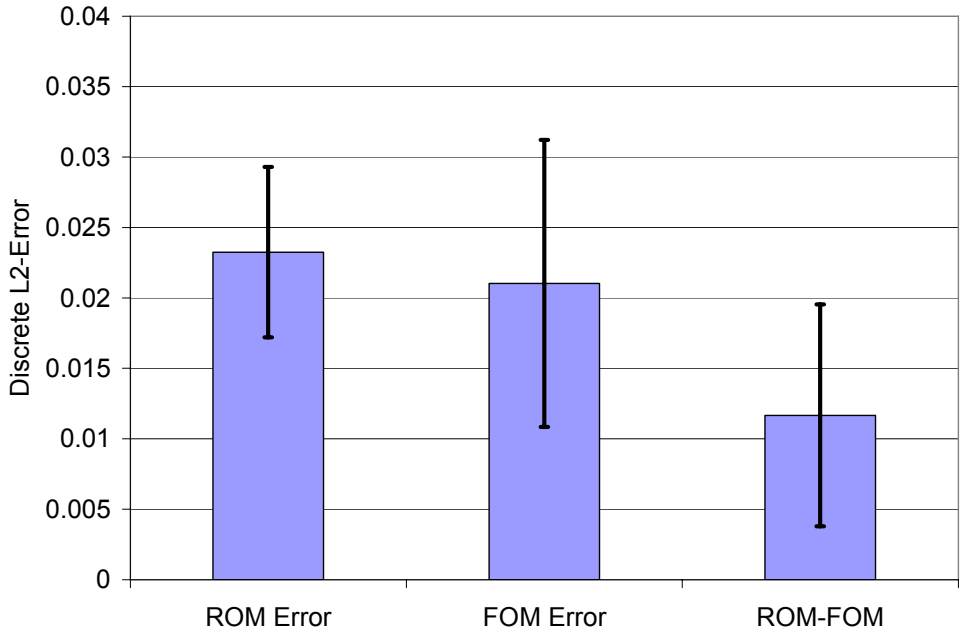

Figure 3.9. Mean and standard deviation (error bars) of the discrete $L_2 - error$ of the pressure responses from the inverse solutions with the ROM and the FOM, and the discrete $L_2 - norm$ of the difference between the pressure responses of the ROM and FOM for Example 3.

Figure 3.10 shows the mean and standard deviation of the equivalent elasticity for the solution parameter sets, and Figure 3.11 shows the mean and standard deviation of the mechanical loss for the solution parameter sets. In this case the equivalent elasticity of the matrix was identified accurately while the equivalent elasticity of the inclusion was less accurate with significant scatter. The mechanical loss of both materials was less accurate and had more scatter than the previous example. Though, in all trials the inclusion was accurately identified to be significantly stiffer than the matrix, and in all but one trial the matrix was accurately identified to have significantly more damping than the inclusion.

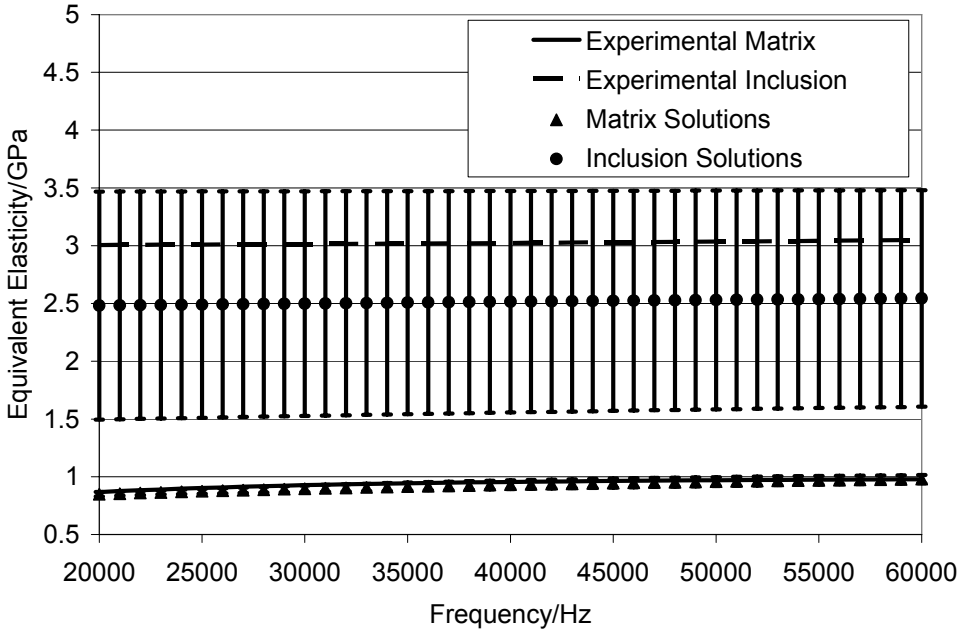

Figure 3.10. Mean and standard deviation (error bars) of the equivalent elasticity for the inverse solutions compared to the experimental value for Example 3.

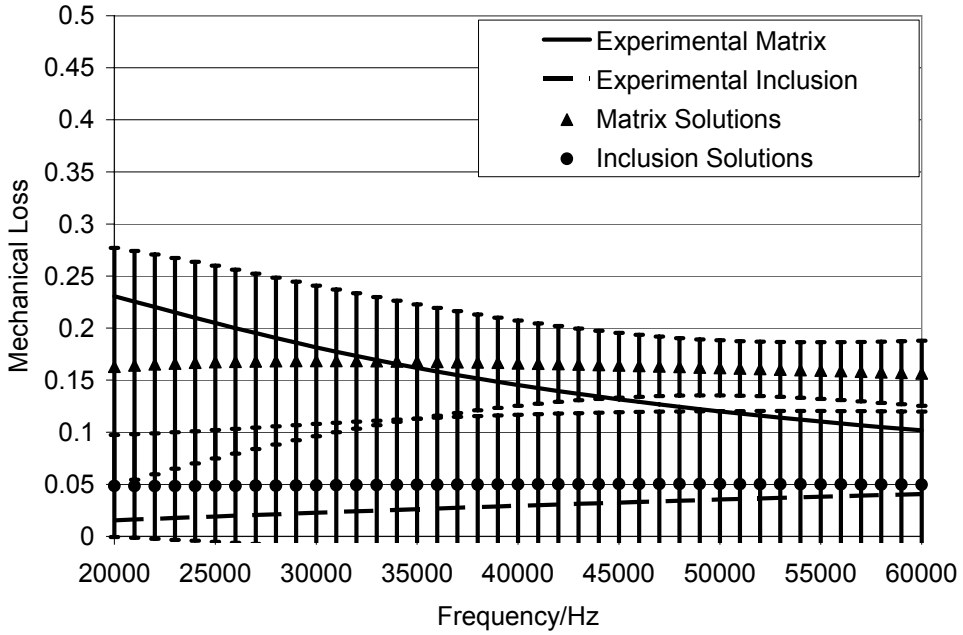

Figure 3.11. Mean and standard deviation (error bars) of the mechanical loss for the inverse solutions compared to the experimental value for Example 3.

The material results for this example emphasize the difficulty of this inverse problem. Clearly, the associated optimization problem had many local minima with errors close to that of the known solution, which lead to the uncertainty in the characterization. Yet, even though the inverse solutions were inaccurate, the POD ROM was again able to replace the FOM accurately, and identify the broad range of parameters which satisfied the experiment. This further goes to show the capabilities of the methodology presented to not just solve inverse problems in vibroacoustics, but to also perform numerical studies of possible experimental setups, to assess sensitivities and identify improvements. Since the method to maximize the diversity of the snapshots leads to accurate POD ROMs without bias, the search space of the inverse problems can be accurately explored.

3.7 Conclusions

A strategy for incorporating ROMs using the method of POD into numerical methods for the inverse characterization of viscoelastic solids was presented and analyzed. The approach included an efficient computational implementation of POD bases for reduced-order Galerkin FE modeling of vibroacoustic systems. In addition, a methodology was proposed for generating solution snapshots with maximum diversity in the material space for creating POD ROMs which have sufficient generalization capabilities for inverse characterization. The snapshot generation method was shown through a plane wave problem to produce POD bases which have excellent approximation capabilities for a broad range of material properties with a minimal number of FOM analyses. Then through two simulated inverse problems the methodology was shown to be capable of accurately and consistently characterizing viscoelastic properties of solids and assessing experimental procedures with minimal added error due to the use of the reduced-order modeling.

REFERENCES

[1] ABAQUS, Documentation, Version 6.5.

[2] S. Acharjee and N. Zabaras, A proper orthogonal decomposition approach to microstructure model reduction in Rodrigues space with applications to optimal control of micro structure-sensitive properties, Acta Materialia 51 (2003) 5627-5646.

[3] W. Aquino, An object-oriented framework for reduced-order models using proper orthogonal decomposition (POD), Computer Methods in Applied Mechanics and Engineering 196 (2007) 4375-4390.

[4] W. Aquino and J.C. Brigham, Self-learning finite elements for inverse estimation of thermal constitutive models, International Journal of Heat and Mass Transfer 49 (2006) pp 2466-2478.

[5] F. Asma and A. Bouazzouni, Finite element model updating using FRF measurements, Shock and Vibration 12 (2005) 377-388.

[6] J.A. Atwell and B.B. King, Proper orthogonal decomposition for reduced basis feedback controllers for parabolic equations, Mathematical and Computer Modelling 33 (2001) 1-19.

[7] A. Bagchi, Updating the mathematical model of a structure using vibration data, Journal of Vibration and Control 11 (2005) 1469-1486.

[8] H.T. Banks, M.L. Joyner, B. Wincheski, and W.P. Winfree, Real time computational algorithms for eddy-current-based damage detection, Inverse Problems 18 (2002) 795-823.

[9] J. Bercoff, S. Chaffai, M. Tanter, L. Sandrin, S. Catheline, M. Fink, J.L. Gennisson, and M. Meunier, In vivo breast tumor detection using transient elastography, Ultrasound in Medicine and Biology 29 (2003) 1387-1396.

[10] J.C. Brigham and W. Aquino, Surrogate-Model Accelerated Random

Search Algorithm for Global Optimization with Applications to Inverse Material Identification, Computer Methods in Applied Mechanics and Engineering 196 (2007) 4561-4576.

[11] J.C. Brigham, W. Aquino, F.G. Mitri, J.F. Greenleaf, and M. Fatemi, Inverse estimation of viscoelastic material properties for solids immersed in fluids using vibroacoustic techniques, Journal of Applied Physics 101 (2007) 23509-1-14.

[12] F.A. Duck, Physical properties of tissue: a comprehensive reference book, Academic Press, London; San Diego, Calif., 1990.

[13] M. Fatemi and J.F. Greenleaf, Ultrasound-stimulated vibro-acoustic spectrography, Science 280 (1998) 82-85.

[14] W.N. Findley, J.S. Lai, and K. Onaran, Creep and relaxation of nonlinear viscoelastic materials, with an introduction to linear viscoelasticity, North-Holland Pub. Co., Amsterdam, New York, 1976.

[15] S. Ganapathysubramanian and N. Zabaras, Design across length scales: a reduced-order model of polycrystal plasticity for the control of micro structure-sensitive material properties, Computer Methods in Applied Mechanics and Engineering 193 (2004) 5017-5034.

[16] D.E. Goldberg, Genetic algorithms in search, optimization, and machine learning, Addison-Wesley, Reading, Mass., 1989.

[17] S. Han and B. Feeny, Application of proper orthogonal decomposition to structural vibration analysis, Mechanical Systems and Signal Processing 17 (2003) 989-1001.

[18] P. Holmes, J.L. Lumley, and G. Berkooz, Turbulence, coherent structures, dynamical systems, and symmetry, Cambridge University Press, Cambridge; New York, 1996.

[19] F. Ihlenburg and I. Babuska, Finite-Element Solution of the Helmholtz-Equation with High Wave-Number.1. The H-Version of the Fem, Computers & Mathematics with Applications 30 (1995) 9-37.

[20] F. Ihlenburg and I. Babuska, Finite element solution of the Helmholtz equation with high wave number.2. The h-p version of the FEM, Siam Journal on Numerical Analysis 34 (1997) 315-358.

[21] E.T. Jaynes, Information Theory and Statistical Mechanics, Physical Review 106 (1957) 620-630.

[22] M.L. Joyner, A numerical study of the POD method in NDE, Applied Mathematics and Computation 174 (2006) 732-754.

[23] G.A. Kopp, J.A. Ferre, and F. Giralt, The use of pattern recognition and proper orthogonal decomposition in identifying the structure of fully-developed free turbulence, Journal of Fluids Engineering-Transactions of the Asme 119 (1997) 289-296.

[24] J. Ladeji-Osias and N.A. Langrana, Analytical Evaluation of Tumors Surrounded by Soft Tissue, Proceeding of the 22nd Annual EMBS International Conference, IEEE, Chicago, IL, 2000, Vol. 3, 2114-2117.

[25] B.M. Learoyd and M.G. Taylor, Alterations with Age in Viscoelastic Properties of Human Arterial Walls, Circulation Research 18 (1966) 278-&.

[26] F. Leibfritz and S. Volkwein, Reduced order output feedback control design for PDE systems using proper orthogonal decomposition and nonlinear semidefinite programming, Linear Algebra and Its Applications 415 (2006) 542-575.

[27] T. Lieu, C. Farhat, and A. Lesoinne, Reduced-order fluid/structure modeling of a complete aircraft configuration, Computer Methods in Applied Mechanics and Engineering 195 (2006) 5730-5742.

[28] H.V. Ly and H.T. Tran, Modeling and control of physical processes using proper orthogonal decomposition, Mathematical and Computer Modelling 33 (2001) 223-236.

[29] M. Mitchell, An introduction to genetic algorithm, MIT Press, Cambridge, Mass., 1998.

[30] F.G. Mitri, Inverse determination of porosity from object's resonances, Journal of Applied Physics 96 (2004) 5866-5869.

[31] F.G. Mitri, P. Trompette, and J.Y. Chapelon, Detection of object resonances by vibro-acoustography and numerical vibrational mode identification, Journal of the Acoustical Society of America 114 (2003) 2648-2653.

[32] Z. Ostrowski, R.A. Bialecki, and A.J. Kassab, Estimation of constant thermal conductivity by use of Proper Orthogonal Decomposition, Computational Mechanics 37 (2005) 52-59.

[33] S.S. Ravindran, A reduced-order approach for optimal control of fluids using proper orthogonal decomposition, International Journal for Numerical Methods in Fluids 34 (2000) 425-448.

[34] J.N. Reddy, An Introduction to the Finite Element Method. 3rd ed, McGraw-Hill, New York, 2006.

[35] D.E. Rosario, J.C. Brigham, and W. Aquino, Identification of Material Properties of Orthotropic Elastic Cylinders Immersed in Fluid Using Vibroacoustic Techniques, International Journal of Ultrasonics (2008 (In Review)).

CHAPTER 4

Current Capabilities and Future Directions

A computational framework was developed for viscoelastic characterization of fluid-immersed solids using vibroacoustic methods, with emphasis on soft tissue characterization. The framework includes an object-oriented implementation of the finite element (FE) method for the numerical modeling of viboracoustic systems, along with a non-gradient based global optimization algorithm for the computational solution strategy for the characterization problems. The FE formulation encompasses steady-state dynamic analysis of isotropic linear viscoelastic solids coupled with homogeneous linear acoustic fluids. The solids can be discretely heterogeneous, the viscoelastic behavior is defined through parameters for complex-valued rate-dependent shear and bulk moduli based on generalized Maxwell rheological representations, the solids can have displacements, pressures, tractions, and body forces applied, and the fluids can have pressures, normal accelerations, and non-reflecting boundary conditions applied. In addition, the proper orthogonal decomposition (POD) method was integrated into the FE implementation to build and use high-accuracy reduced-order models for computationally expensive vibroacoustic systems. Lastly, the surrogate-model accelerated random search (SMARS) algorithm was incorporated to minimize the difference between sets of experimental data and FE models representing the experiments, to obtain approximations to the viscoelastic properties. SMARS incorporates a stochastic global search technique, along with machine learning tools to identify global minimization solutions with a limited number of FE evaluations.

The current computational system is capable of accurately and efficiently analyzing and characterizing solids for typical laboratory developmental systems for

vibroacoustic methods (e.g. water tanks with synthetic solids). In addition, the current framework can be applied to clinical applications in which the solids can be assumed to be discretely heterogeneous (e.g. homogeneous tissues surrounding homogeneous inclusions), and the vibroacoustic behavior and resulting characterization can be assumed to be defined as a linear perturbation to the system. This could include applications, such as, the characterization of breast tissues which have select regions that are possible tumors.

However, certain extensions need to be made in order for the framework to be clinically applicable in general. First and foremost, the FE implementation needs to be parallelized for cluster computing. The computational cost of the full-order FE simulations, which are necessary even to create POD reduced-order models, to represent many biological systems in the frequency ranges typical of medical vibroacoustic methods is in excess of current serial computing capabilities. Also, the physics which can be represented needs to be extended. This could include incorporating anisotropy into the solid behavior (e.g. fibrous tissues), as well as a generalized treatment of heterogeneity to account for unknown inclusion locations or gradual property variations. In addition, the fluid behavior may need to be extended to incorporate viscosity, or even fluid flow due, for instance, to the circulatory system. An even more challenging yet important possibility is to account for variations in geometric characteristics of biological systems. For example, changes in the diameter or thickness of arterial vessels can be highly uncertain for noninvasive *in vivo* testing. The computational inverse solution strategy can account for any variable model parameter of the system, including geometry. However, to allow geometry to be freely varying in a FE model requires significant consideration into geometric mapping and adaptive meshing techniques. Lastly, the framework could be extended to include methods to formally analyze and account for sensitivity and uncertainty of

the system unknowns, thereby, producing a system which can quantitatively evaluate experimental approaches to assist in experiment design, as well as provide probability distributions of the characterized quantities given input uncertainties.